ADVANCED STEEL CONSTRUCTION
an international journal

ISSN 1816-112X

Science Citation Index Expanded, Materials Science Citation Index and ISI Alerting

Advanced Steel Construction
an international journal

Cover: 1000ton+ temporary steel platform in support of heavy-duty mobile cranes, designed by second-order direct analysis without effective length

e-copy of IJASC is free to download at "www.ascjournal.com" in internet and mobile apps.

General Information
Advanced Steel Construction, an international journal

Aims and scope

The International Journal of Advanced Steel Construction provides a platform for the publication and rapid dissemination of original and up-to-date research and technological developments in steel construction, design and analysis. Scope of research papers published in this journal includes but is not limited to theoretical and experimental research on elements, assemblages, systems, material, design philosophy and codification, standards, fabrication, projects of innovative nature and computer techniques. The journal is specifically tailored to channel the exchange of technological know-how between researchers and practitioners. Contributions from all aspects related to the recent developments of advanced steel construction are welcome.

Instructions to authors

Submission of the manuscript. Authors may submit on-line at **www.hkisc.org**

Asian Pacific , African and organizing editor :	Professor S.L. Chan, Email: ceslchan@polyu.edu.hk
American editor :	Professor W.F. Chen, Email: waifah@hawaii.edu
European editor :	Professor R. Zandonini, Email: riccardo_zandonini@ing.unitn.it

All manuscripts submitted to the journal are recommended to accompany with a list of four potential reviewers suggested by the author(s). This list should include the complete name, address, telephone and fax numbers, email address, and at least five keywords that identify the expertise of each reviewer. This scheme will improve the process of review.

Style of manuscript

General. Author(s) should provide full postal and email addresses and fax number for correspondence. The manuscript including abstract, keywords, references, figures and tables should be in English with pages numbered and typed with double line spacing on single side of A4 or letter-sized paper. The front page of the article should contain:

a) a short title (reflecting the content of the paper);
b) all the name(s) and postal and email addresses of author(s) specifying the author to whom correspondence and proofs should be sent;
c) an abstract of 100-200 words; and
d) 5 to 8 keywords.

The paper must contain an introduction and a conclusion. The length of paper should not exceed 25 journal pages (approximately 15,000 words equivalents).

Tables and figures. Tables and figures including photographs should be typed, numbered consecutively in Arabic numerals and with short titles. They should be referred in the text as Figure 1, Table 2, etc. Originally drawn figures and photographs should be provided in a form suitable for photographic reproduction and reduction in the journal.

Mathematical expressions and units. The Systeme Internationale (SI) should be followed whenever possible. The numbers identifying the displayed mathematical expression should be referred to in the text as Eq. 1, Eq. 2.

References. References to published literature should be referred in the text, in the order of citation with Arabic numerals, by the last name(s) of the author(s) (e.g. Zandonini and Zanon [3]) or if more than three authors (e.g. Zandonini et al. [4]). References should be in English with occasional allowance of 1-2 exceptional references in local languages and reflect the current state-of-technology. Journal titles should be abbreviated in the style of the Word List of Scientific Periodicals. References should be cited in the following style [1, 2, 3].

Journal: [1] Chen, W.F. and Kishi, N., "Semi-rigid Steel Beam-to-column Connections, Data Base and Modelling", Journal of Structural Engineering, ASCE, 1989, Vol. 115, No. 1, pp. 105-119.

Book: [2] Chan, S.L. and Chui, P.P.T., "Non-linear Static and Cyclic Analysis of Semi-rigid Steel Frames", Elsevier Science, 2000.

Proceedings: [3] Zandonini, R. and Zanon, P., "Experimental Analysis of Steel Beams with Semi-rigid Joints", Proceedings of International Conference on Advances in Steel Structures, Hong Kong, 1996, Vol. 1, pp. 356-364.

Proofs. Proof will be sent to the corresponding author to correct any typesetting errors. Alternations to the original manuscript at this stage will not be accepted. Proofs should be returned within 48 hours of receipt on-line.

Copyright. Submission of an article to "Advanced Steel Construction" implies that it presents the original and unpublished work, and not under consideration for publication nor published elsewhere. On acceptance of a manuscript submitted, the copyright thereof is transferred to the publisher by the Transfer of Copyright Agreement and upon the acceptance of publication for the papers, the corresponding author must sign the form for Transfer of Copyright.

Permission. Quoting from this journal is granted provided that the customary acknowledgement is given to the source.

Page charge and Reprints. There will be no page charges if the length of paper is within the limit of 25 journal pages. A total of 30 free offprints will be supplied free of charge to the corresponding author. Purchasing orders for additional offprints can be made on order forms which will be sent to the authors. These instructions can be obtained at the Hong Kong Institute of Steel Construction, Journal website: http://www.hkisc.org

The International Journal of Advanced Steel Construction is published quarterly by learnt society, The Hong Kong Institute of Steel Construction, c/o Department of Civil & Environmental Engineering, The Hong Kong Polytechnic University, Hung Hom, Kowloon, Hong Kong.

Subscription inquiries and change of address. Address all subscription inquiries and correspondence to Member Records, IJASC. Notify an address change as soon as possible. All communications should include both old and new addresses with zip codes and be accompanied by a mailing label from a recent issue. Allow six weeks for all changes to become effective.

The Hong Kong Institute of Steel Construction
HKISC
c/o Department of Civil and Environmental Engineering,
The Hong Kong Polytechnic University,
Hunghom, Kowloon, Hong Kong, China.
Tel: 852- 2766 6047 Fax: 852- 2334 6389
Email: *ceslchan@polyu.edu.hk* Website: *http://www.hkisc.org/*
ISSN 1816-112X
Science Citation Index Expanded, Materials Science Citation Index and ISI Alerting

ISSN 1816-112X

Science Citation Index Expanded, Materials Science Citation Index and ISI Alerting

Advanced Steel Construction
an international journal

VOLUME 12 NUMBER 2 JUNE 2016

Technical Papers

Announcement by IJASC :

OUTRIGGER TOPOLOGY AND BEHAVIOUR

Goman W.M. Ho

Arup, Level 5, 80 Tat Chee Avenue, Kowloon Tong, Hong Kong
(E-mail: goman.ho@arup.com)

Received: 23 February 2012; Revised: 10 September 2015; Accepted: 30 September 2015

ABSTRACT: The structural efficiency of tall buildings heavily depends on their stiffness and lateral resistance capacity. Among those structural systems for tall buildings, outriggers system is the most common one for buildings with a relatively regular floor plan. Research in outriggers system is relatively limited and usually focuses on the optimal locations/levels of outrigger only. However, the locations of the outriggers are usually dictated by the functional use of the tall buildings and outriggers are usually located in the less commercial valuable floors such as mechanical or refuge floors. Because of this limitation, the topology of outriggers becomes an important element in providing an optimum design. Furthermore, most engineers considered that the performance of buildings is a linear relationship with the stiffness and the critical load of the outriggers. Nevertheless, this is not always true if the ultimate design load condition is being considered. This paper starts with various topologies of outrigger which are commonly used in practice; studies their stability behaviour, compares their stiffness and finally their ultimate load capacity. Examples demonstrate that for some outriggers geometry arrangement or topologies which delivered maximum stiffness and critical loads do not always yield the highest ultimate load capacity even for same outrigger member sizes.

DOI: 10.18057/IJASC.2016.12.2.1

Keywords : Tall buildings, outrigger systems

1. INTRODUCTION

The race to the sky started from the time of Tower of Babel following the invention of bricks. Nowadays, engineers use reinforced concrete, steel or composite material of steel and concrete to build high-rise buildings. Furthermore, various lateral structural systems such as shear walls, core-perimeter frame, tube-in-tube, core-outriggers with or without belt truss and mega frame etc. were developed. Ali and Moon [1] had a comprehensive review on the development of structural systems for tall buildings. Among the Interior Structures, "outrigger structures" is the category with efficient height limit up to 150 storeys. Hong Kong Cheung Kong Center (290m), Hong Kong IFC2 (380m), Hong Kong ICC (450m), Taipei 101 (509m) are typical well known tall building examples with outrigger systems.

The first building with elevators was the Equitable Life Assurance Building in New York completed in 1870. This 40m tall building was named as the world first tall building. The structural system is just simply framed building. With the height of buildings increasing, stiffness becomes an important issue. By simple engineering principle, the lateral resistance increases if the moment arm of building can be stretch out from the core to the extreme perimeter. Therefore, engineers started considering using stiff beams to connect both the core and the perimeter tube. It is obvious that the stiffer the beam, the further increase in lateral stiffness. Once buildings became taller, it was very difficult to adopt the "stiff" beam concept as the depth of the "stiff" beam would be as deep as a wall. Concrete outrigger systems were therefore developed. Shankar Nair [2] proposed the concept of "Virtual Outrigger" but engineers must make sure that the stiffened coupled floors and the vertical perimeter structures can provide sufficient stiffness to behave as outriggers.

After World War II, the use of steel in tall buildings became popular because of the speed of construction and reduction in labour cost etc. With buildings with typical slenderness ratio and taller than 40 storeys, the previous “stiff” beam method is replaced by single or double story high steel truss. Although the use of outriggers is getting more widespread, research in outrigger systems is still very limited. Taranath [3], Stafford Smith [4], Gerasimidis et al [5] and Fawiza et al [6] studies focus on the overall efficiency of outriggers in tall buildings in controlling drifts and optimum locations of outriggers. Nevertheless, the possible locations for which can allow the designers to install the outriggers system are limited by the function of the buildings. In practice, outriggers are limited to be installed in mechanical or refugee floors instead of “optimum” locations. Ideally outriggers should be as deep as possible and therefore engineers often request double story height space for outriggers. In China, refuge floors are required for every 15 floors. Hence, in some buildings, the floor spaces which can allow for outriggers to be installed are limited to be single story height. Therefore, study on optimum topology of outrigger layout rather than the optimum locations of outriggers is needed. To the knowledge of the author, there is no literature on the topology of outriggers and its effect to stiffness and strength which is publicly available.

Also, the belief that the performance of tall buildings against drift is a linear function of outrigger stiffness leads to a tendency of providing oversize and overstiff outriggers in tall buildings. However, wind loading is not the only lateral load for tall buildings; seismic resistance is also an important factor for considerations in some area. Therefore, a balance for the stiffness, strength and ductility of the outriggers should be an area which engineers should pay special attention.

Outriggers increase the stiffness of buildings by means of converting the lateral forces into push (compression) and pull (tension) forces in the perimeter structures. Hence, outriggers are required to resist reverse and cyclic loading. From engineering principle, the topology for outrigger system should be symmetric to both upward and downward load such that it provides similar performance in all load cases. If symmetric topology cannot be used, the designer must be aware of the behaviour of outriggers under cyclic load.

2. TOPOLOGY OF OUTRIGGERS

With reference to most of the aforementioned text books, the typical diagrams for outriggers are as Figure 1. However, from a practical engineering point of view, these layout are neither possible nor efficient. Figure 1a shows an ideal situation for concrete outriggers. In practice, it is not possible to have a complete solid concrete wall between core and perimeter frame as doorways must be required. With a door access, the stiffness of concrete outriggers will greatly be reduced. Figure 1b shows a braced steel core and steel truss as outrigger while 1c shows a concrete core with simple cross braces as outriggers. For presentation purposes, these diagrams are clean and clear. However, in reality, the topologies for outriggers are very different and subject to a lot of co-ordination between architects, structural and building service engineers.

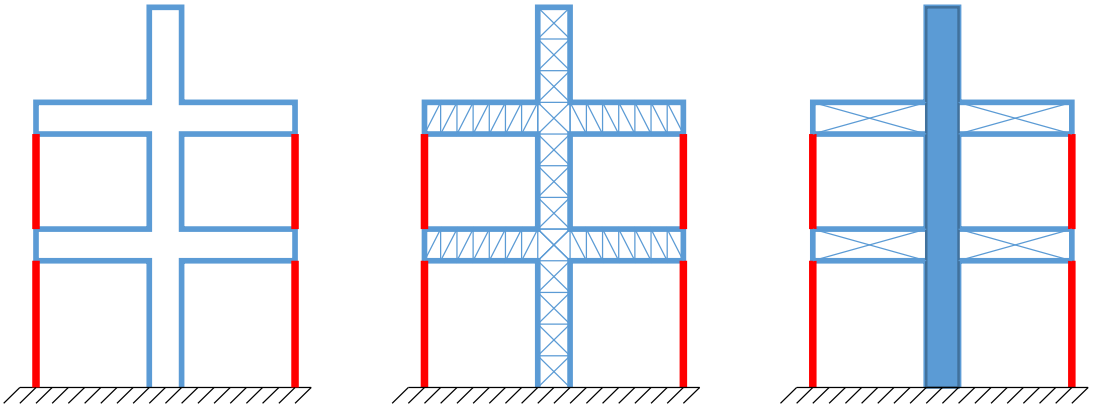

Figure 1. Typical Diagrammatic Drawings for Outrigger Systems

It is not possible to study all the topological options for outriggers. Therefore, the most practical and common samples are selected in this studies. Figure 2 indicates a typical example with design constraints- Double story space (2x4.2m) between core and perimeter frame (13m span).

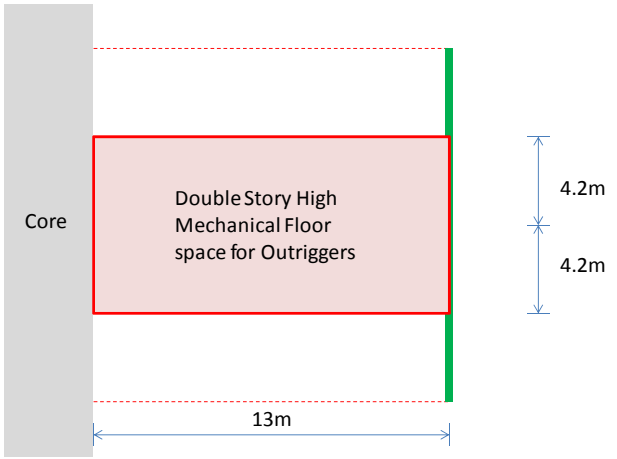

Figure 2. Design Constraints for Outriggers

Based on same space constraints, four practical topologies of outriggers are presented in Figures 3, 4 and 5. Figure 3 is a “>” shaped outriggers as topology A. Figure 4 shows options B which is also as simple as topology A with bottom chord to be in the same level of floor. Figure 5a and b show topology C and D respectively. Both topology C and D are basically identical except there is no vertical member in topology D in comparsion with C. To demonstrate the effect of stiffness, two kinds of member sizes are used. They are either fabricated square hollow section (SHS) of 1000mmx1000mmx50mmx50mm or Universal Beam (UB)UB304x127x42. The latter (UB) example is for reference and comparison purpose only as such member sizes are generally too small in practice. However, it provides the idea that the behaviour of outriggers varies with its member stiffness even with no topology change. All connections are assumed to be fully rigid except the vertical load applied to the tips of outriggers are pure vertical and conservative. All connections are assumed to be rigid because in most practical cases, outrigger members are heavy so designing a pinned connection would not be justifiable.

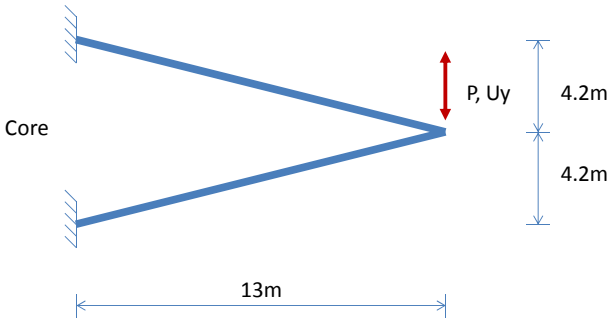

Figure 3. Topology A

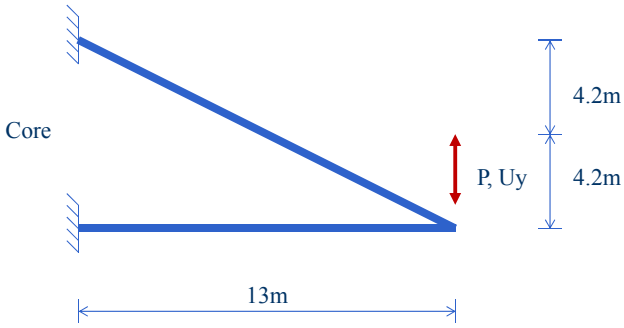

Figure 4. Topology B

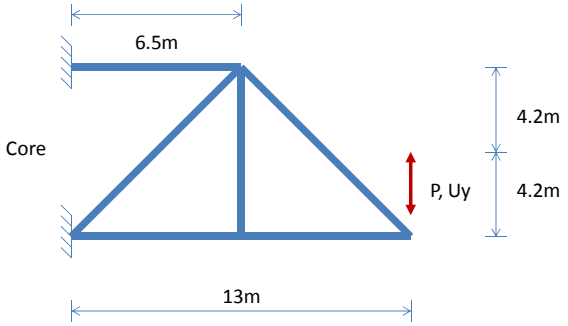

Figure 5a. Topology C

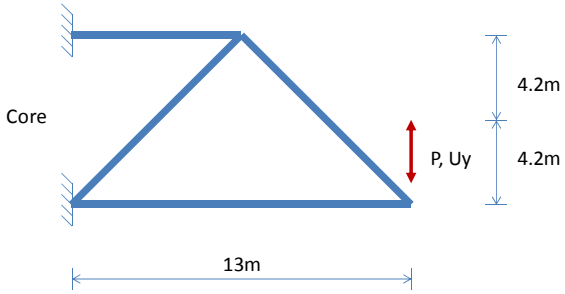

Figure 5b. Topology D

3. GEOMETRIC NONLINEAR ANALYSIS AND ADVANCED ANALYSIS

For all cases, unit downward (-ve) and upward (+ve) load were applied to the tip of outriggers. Geometric nonlinear analysis was carried out for all options to gain a better understanding on the impact of topology to the behaviour of outriggers. Considering the robustness in obtaining solution for the critical load of outriggers and the convenient in obtaining the stiffness of outrigger, Displacement Control method is used. For all geometric nonlinear analysis, the vertical displacement at the tip of outrigger (U_y) is selected as the numerical constraints parameter and all with constants displacement load steps up to 5m. The displacement up to 5m is larger than necessary but does provide results to confirm whether or not hardening effect is present. The initial stiffness of outrigger, ${}_0K_T$ is denoted as

$$_0K_T = {}_0F/{}_0U_y$$

where $_0F$ represents the load reaction at the first displacement control load step $_0U_y$. Because displacement control method is used, $_0U_y$ can be the same for all options and studies. Hence, the $_0F$ obtained from the analysis is the stiffness of the outriggers. For each topology, with the consideration of geometric nonlinear effects, there are two values for the stiffness, one for download and one for upward load. For comparison purposes, all loads and displacements are taken as positive so the curves can be compared directly. For the cases where the critical point is not clear enough to be determined, reference will be made to the first and second derivatives of the load-deflection curve.

Generally speaking, the magnitude of critical load of a structure is considered to reflect the ultimate load capacity. From typical member capacity check, engineers will first determine the critical loads; calculate the effective length and then the member capacity. Therefore, before engineers calculate the member sizes, they will consider the 2nd Order load-deflection curve as an indicator to the load capacity and the initial slope for the stiffness. Hence most engineers will consider that the higher the critical load, the higher the member capacity. To validate this concept, advanced analysis technique is also applied to determine the capacity for members. Member section capacity ratio will also be listed so that we could have a whole picture on the behaviour of each outrigger topology. In advanced analysis, NIDA version 9.0.1.0 (Build 10) [7] is used with S275 steel, initial imperfection of all members to be L/1000 and the design to Hong Kong Code [8].

Topology A

Because Topology A is symmetrical to both upward and download load at tip, option A will therefore generate only one single response curve for both load cases. The 2nd order analysis indicates that there is minor hardening (member under tension) effect for the SHS section. For UB section, there is a minor drop in load resistance after critical load before hardening starts. A summary of analysis results for topology A for both SHS and UB sections is listed in Table 1.

Table 1. Results for Topology A

A-SHS	A-UB
Stiffness, K_0=551160kN/m	Stiffness, K_0=15022kN/m
Design Load Capacity, P_N =531MN	Design Load Capacity, P_N=1528kN
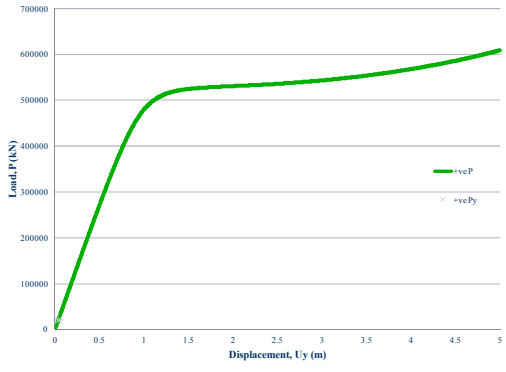	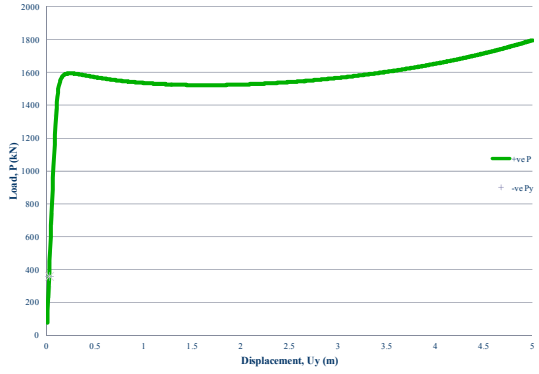

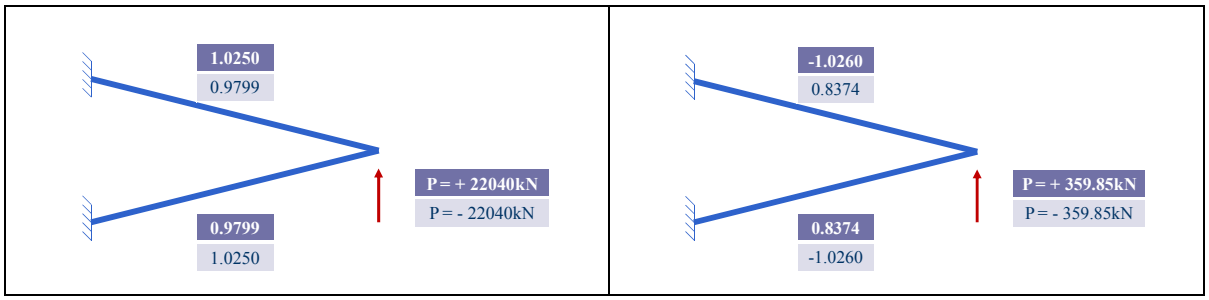

The design load capacity, P_N for SHS and UB cases are 531MN and 1528 kN respectively. The numbers next to members indicate the corresponding section capacity ratio for that member under "+ve" or "-ve" load P. The results show that for topology A, the section capacities for both sections are 2% difference in SHS case and 16% in UB case. The differences in section capacities reflect the efficiency of the topology. Topology A with SHS section is relatively optimal as the section capacities for both members are close to each other in both cases. For Topology A with UB sections, the 16% difference in section capacities indicated that the geometric effect which affecting the stiffness in UB case is more significant than SHS cases. If the geometric effect is not taken into account, in elastic case, the stiffness for topology A will have only one value for both upward and downward cases. Therefore, the section capacity ratios for both SHS and UB cases will be identical.

Topology B

Although Topology B has two members and same as Topology A, it consists of one inclined member only while the other is horizontal. This topology is also common in practice as the horizontal member could also be used as floor beam. The critical load is 351MN for upward load and 628MN for downward load. The results are listed in the table 2.

Table 2. Results for Topology B

B-SHS	B-UB
Stiffness, K_0=476910kN/m : (479130kN/m)	Stiffness, K_0=12918kN/m : (13006kN/m)
Design Load Capacity, P_N =351MN : (628MN)	Design Load Capacity, P_N=1070kN : (1870kN)
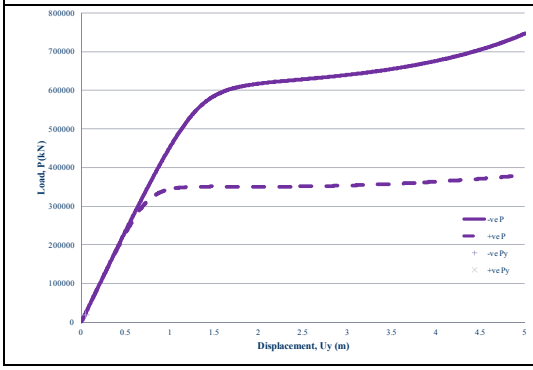	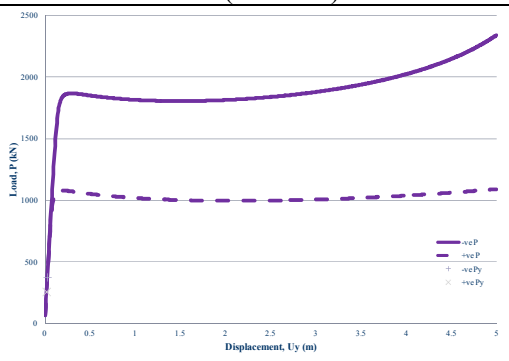

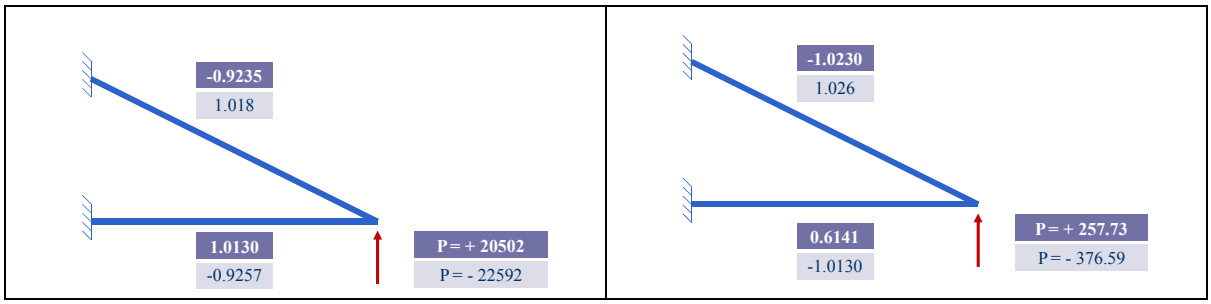

For the case of upward load, the inclined member is subject to compression while the horizontal member is under tension and vice versa. However, it is quite clear that the in the contribution of the horizontal member in case of download load could contribute more than the case of upward load. Therefore, in the case of UB sections, the section capacity ratio for the horizontal members under upward load is much lower than the downward load case. The difference in SHS section is relatively small because the stiffness in SHS model is comparatively high and again, the geometric effect is less significant.

Topology C

Through the finding of Topology A and B, engineers may conclude that outriggers should be as stiff as possible to minimize the geometric effect. Besides that, by providing very stiff members, the structures should also deliver high capacity. This concept is questionable if we consider 2nd order effect. Therefore, Topology C and D are introduced in this study. For Topology C, there isn't a sharp critical point for the upward load case in the 2nd order analysis. Therefore, the critical loads for both cases are based on the first and second derivatives of the load-deflection curves. The load-deflection curve also indicates hardening effect for the downward load cases is significant.

Table 3 : Results for Topology C

C-SHS	C-UB
Stiffness, K_0=723870kN/m : (723640kN/m)	Stiffness, K_0=191531kN/m : (191530kN/m)
Design Load Capacity, P_N =1020MN : (1630MN)	Design Load Capacity, P_N=3030kN : (4600kN)
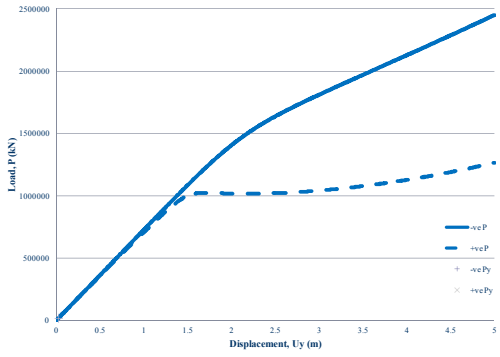	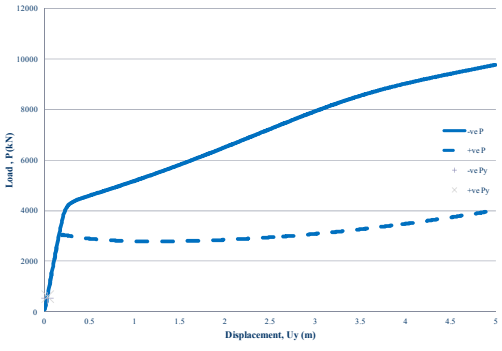

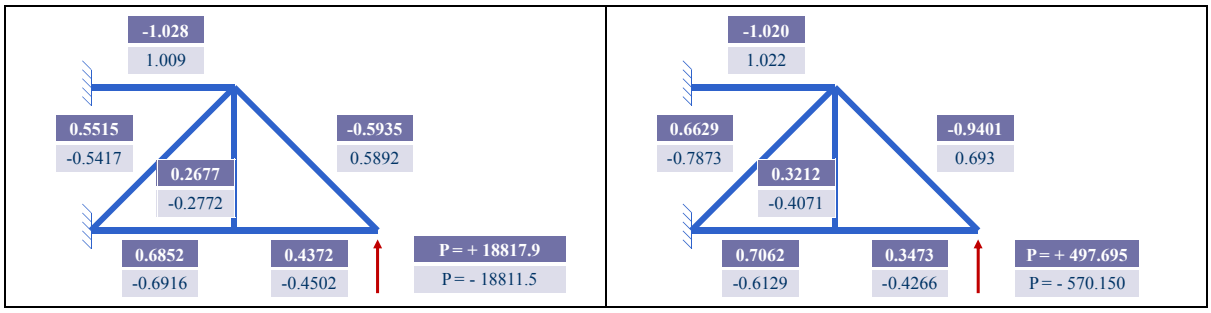

The stiffness for topology C models is in the order of 30%+ and 27%+ higher than Topology A for the case of SHS and UB models respectively. The critical loads for Topology C are also 3 times higher than Topology A. If we are going to check the final capacity, engineers will consider that Topology will provide much higher section capacity than Topology A. However, the ultimate load obtained by Topology C is lower than Topology A and B. By checking the capacity ratios, the most critical member is the top chord which controls the design in both upward and downward load cases. The vertical member is as low as 0.27 (+P) and 0.28 (-P). This indicates that the structures are not efficient and there are many dummy members. Although it delivers higher stiffness, the distribution of internal forces and stress are not even which causes a much lower ultimate load capacity than Topology A and B.

Topology D

From the finding of Topology C, Topology D is proposed but with the vertical member removed. The results are listed in Table 4.

Table 4. Results for Topology D

D-SHS	D-UB
Stiffness, K_0=476910kN/m : (479130kN/m)	Stiffness, K_0=12918kN/m : (13006kN/m)
Design Load Capacity, P_N =1010MN : (1360MN)	Design Load Capacity, P_N=2840kN : (4100kN)
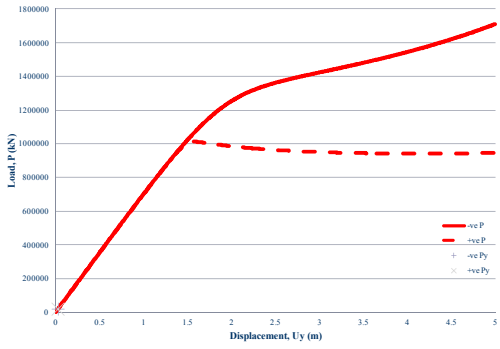	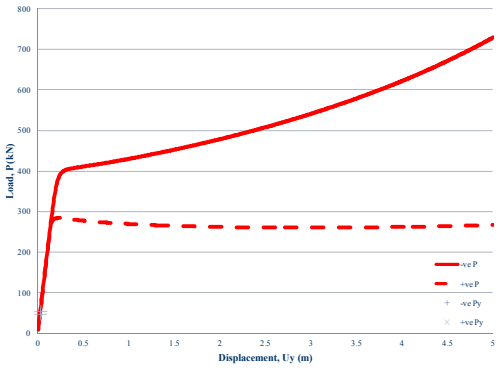
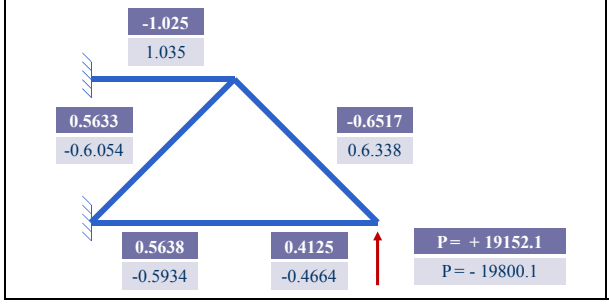	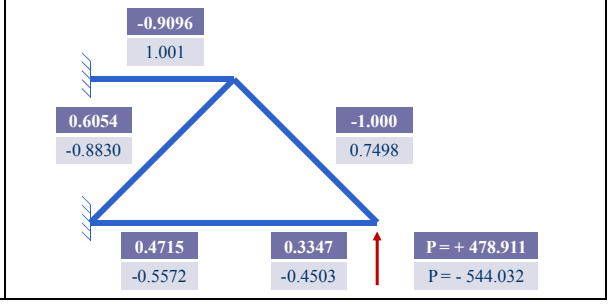

The stiffness and ultimate load capacity of Topology D is slightly less than C but of a similar order. This further proves the finding from Topology C as the section capacity ratios in Topology D at ultimate load are more evenly distribute than Topology C. It is interesting to find out that for the case of upward load, no hardening effect is found and the structure is degrading after yield for both SHS and UB cases.

4. SUMMARY AND CONCLUSION

For ease of comparison, the SHS and UB cases are grouped in Figure X and Y respectively. Through the figures, readers can compare the stiffness, load-deflection relationship etc. for either SHS or UB sections.

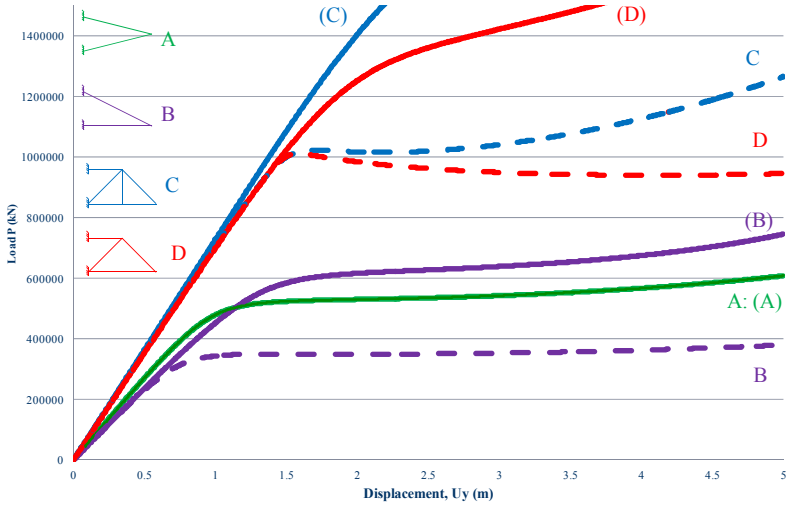

Figure 6. Load-Deflection Plot for SHS section
*For the cases of downward force, the curve will be named with a bracket ().

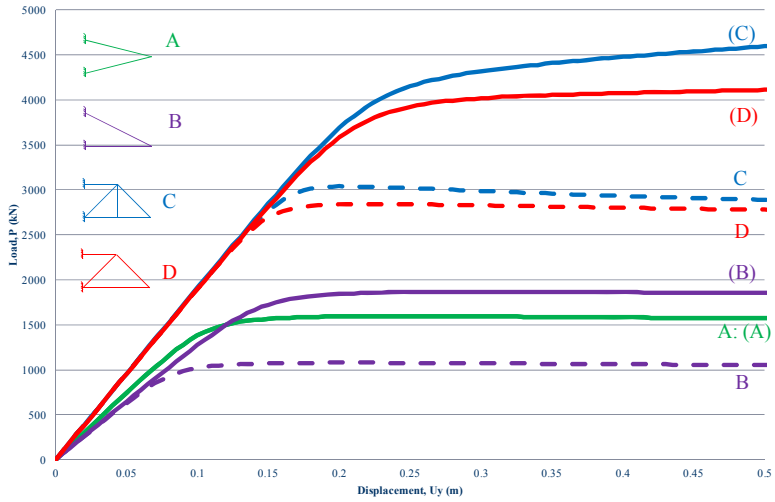

Figure 7. Load-Deflection Plot for UB section
*For the cases of downward force, the curve will be named with a bracket ().

The results are also summarized in Table 5 and 6. The ratio of P_{cr} and P_N in percentage were tabled where P_{cr} is the critical load obtained from 2nd Order analysis and P_N is the ultimate load capacity obtained from advanced analysis.

Table 5. Summary of Results for Outrigger Topologies with SHS Section

Load Direction	A-SHS	B-SHS	C-SHS	D-SHS
$+P_{cr}$	531MN	351MN	1020MN	1010MN
$-P_{cr}$		-628MN	-1630MN	-1360MN
$+P_N$	22040kN (4.15%)	20502kN (5.84%)	18818kN (1.84%)	19152KN (1.90%)
$-P_N$		-22592kN (3.60%)	-18812kN (1.15%)	-19800kN (1.46%)

Table 6. Summary of Results for Outrigger Topologies with UB Section

Load Direction	A-UB	B-UB	C-UB	D-UB
$+P_{cr}$	1582 kN	1070kN	3030 kN	2840 kN
$-P_{cr}$		-1870 kN	-4600 kN	-4100 kN
$+P_N$	359.85 kN (22.72%)	257.73 kN (24.09%)	497.77 kN (16.43%)	478.91 kN (16.86%)
$-P_N$		-376.59 kN (20.14%)	-550.15 kN (11.96%)	-544.03 kN (13.26%)

A total of four practical outrigger geometries or topologies were studied. Through the finding from this study, the following conclusions are listed:

1. Unlike elastic analysis, there is more than one stiffness value for a unsymmetrical outrigger if geometric effect is taken into account as stiffness under compression is less than under tension;
2. For the same topology of outrigger, the outrigger behaviour varies according to its member stiffness. In other words, the outrigger behaviour changes if the section size changes. This means that if engineer reduces the member sizes, the design capacity is not linear proportion because the behaviour for stiff and soft members will be quite different. Similarly, enlarged sections in an outrigger structure do not always means the structure will perform better. Engineers should have a clear understanding on how the structure behaves and also the member contribution to the overall structural behaviour.

In general, the higher the structure stiffness, the less geometric effect and hence higher buckling or critical load. However, the 2nd order critical load of a structure and stiffness is not directly proportional to the ultimate load capacity of an outrigger. Therefore, higher stiffness does not always yield high ultimate load capacity. This is very important concept especially when the structure is under cyclic load (e.g. seismic cases). The above finding and conclusion do not just apply to outrigger structures but also all slender structures. From the study of four topologies of outrigger system which considered the 2nd order geometric effect, material nonlinearity and also design load capacity, the topology of outriggers should be as simple and symmetrical as possible. If stiffness must be increased, it is suggested to enlarge the member size instead of changing the topology. However, engineers must be aware that the internal forces within a structure change according to its stiffness. The actions may cause a member, which is previously controlled by axial force, to become moment controlled etc. A good understanding in outriggers behaviours is always needed. Among all four topologies, Topology A is possibly the best option and B be the second choice.

ACKNOWLEDGEMENT

The author would like to express his thanks and support to Hong Kong Polytechnic University in providing an excellent research environment during the author's sabbatical leave, Prof. S.L. Chan in allowing me to use NIDA software for this study and for his valuable comments on this manuscript.

REFERENCES

[1] Mir, M. Ali and Kyoung, Sun Moon, "Structural Developments in Tall Buildings: Current Trends and Future Prospects", Architectural Science Review, 2007, Vol. 50, No. 3 pp. 205-223.

[2] Shankar Nair, B. "Belt Trusses and Basements as "Virtual" Outriggers for Tall Buildings", 4th Quarter, Engineering Journal, 1998, AISC.

[3] Taranath, B.S., "Structural Analysis & Design of Tall Buildings", McGraw-Hill, 1988.

[4] Stafford Smith, B and Coull, A, "Tall Building Structures- Analysis and Design", John Wiley & Sons, INC, 1991

[5] Gerasimidis S., Efthymiou E. and Baniotopoulos C.C., "Optimum Outrigger Locations of High-rise Steel Buildings for Wind Loading", 5th European and African Conference on Wind Engineering (Proceedings), 2009

[6] Fawzia, S., Nasir, A. and Fatima, T., "Study of the Effectiveness of Outrigger System for High-Rise Composite Buildings for Cyclonic Region", Vol. 60, World Academy of Science, Engineering and Technology, 2011.

[7] http://www.nida-naf.com

[8] Code of Practice for the Structural Use of Steel 2011, Buildings Department, Hong Kong SAR Government.

STUDY ON AXIAL COMPRESSION BEARING CAPACITY OF REINFORCED CONCRETE FILLED STEEL TUBE MEMBERS

Xiao-Xiong Zha*, Xiao-Li Li, Ning Wang and Cheng-Yong Wan

Shenzhen Graduate School, Harbin Institute of Technology, Shenzhen 518055, China
**(Corresponding author: E-mail: Zhaxx@hit.edu.cn)*

Received: 30 May 2014; Revised: 30 January 2015; Accepted: 25 June 2015

ABSTRACT: The bearing capacity equation of reinforced concrete filled steel tube (RCFST) members under axial loads is derived by using the combined unified and limit equilibrium theories. The concrete strength increase due to the constraint effect of the steel tube is taken into account through the use of unified theory; whereas the concrete strength increase due to the constraint effect of the stirrups is considered through the use of the limit equilibrium theory. Three-dimensional nonlinear finite element analysis and experimental tests were carried out and the corresponding results are reported in this paper. The comparisons of the numerical, experimental and theoretical results show that there are in good agreement between these three different methods. However, the present theoretical analysis model is not only simple and convenient to use but also consistent with existing Chinese design codes for CFST columns.

Keywords: Reinforced concrete filled steel tube, Axial compression bearing capacity, Unified theory, Limit equilibrium theory, Finite element

DOI: 10.18057/IJASC.2016.12.2.2

1. INTRODUCTION

Because of many advantages, concrete filled steel tubes (CFST) are very popular in high rise buildings, bridges and offshore structures. Extensive studies have been conducted on the static and dynamic analyses, and the fire performance of CFST members [1-10]. For example, Han et al. [1], Yu et al. [2], Dundu et al. [3], Dai et al. [4] studied the compressive strength of CFST members. Han et al. [1], Yu et al. [5], Prabhu et al. [6] investigated the axial compression performance of CFST members encased by various different materials, such as concrete, FRP and CFRP. Wang et al. [7] studied the behavior of fire-exposed CFST columns. More recently, Ma et al. [8] studied their seismic behavior of CFST columns. Based on these studies, Chinese Codes [11] for design of concrete filled steel tubular members has been developed in 2014.

A RCFST member is formed by filling a steel tube with reinforcement concrete. Because of the large size of the section the RCFST members may have smaller thickness of steel tube than CFST members, which can cause trouble in machining, construction and welding. Reinforced concrete filled steel tubes (RCFST) have been used in multi-story buildings, particularly, high-level buildings. Figure 1 shows a typical section of a steel tube column and the corresponding column layout of Shenzhen Jingji financial center, which is ranked as the tenth highest building in the world.

Some studies have been conducted on the static performance of RCFST columns [12-20]. Lie [14] gave the resistance of circular steel columns filled with bar-reinforced concrete. Chang et al. [15] and Zhu et al. [16] conducted experimental studies on the performance of steel-reinforced concrete-filled-steel tubular members. Wang et al. [18] studied on experimental performance twin-column RCFT pier. Endo et al. [19] and Xiamuxi et al. [20] obtained the evaluation for axial

compressive strength of RCFST columns and the results were validated using experimental data. But most studies on the mechanical properties at room temperature didn't consider the constraints of the stirrup on core concrete. And they just simply considered the superposition of steel tube, concrete and longitudinal reinforcement on the basis of a coefficient, not considering the synergy of steel tube and concrete.

Notations			
K	Lateral constant determined by tests, $K=4$ usually	A_{cor}	Area of concrete confined by stirrups, $A_{cor}=\pi d_s^2/4$
f'_{ck}	Axial compressive strength of concrete confined by concrete stirrup	f , f_c	Design strength of steel and concrete, respectively
f_r	Lateral pressure on concrete surrounded by stirrups	θ^*	Equivalent confining factor of multilayer stirrups
A_{ss1}	Area of single-layer stirrup	α	Steel ratio
f_{yv}	Tensile strength of stirrup	ψ	Hollow ratio, $\psi = A_h/(A_c+A_h)$
d_s	Ddiameter of concrete column surrounded by stirrups	f_y , f_{ck}	Characteristic strength of steel and concrete, respectively
s	Spacing of stirrups	B , C	Parameters according to section types
A_{sso}	Equivalent reinforcement area of stirrup, $A_{sso}=\frac{\pi d_s A_{ss1}}{s}$	θ_h	Standard value of confining factor, $\theta_h=\alpha_0 f_y/(1.1 f_{ck})$
A_c , A_h	Area of concrete and hollow part in HCFST, respectively	θ , θ_1	Confining factor of steel tube in CFST and RCFST respectively, and $\theta=\frac{A_S f_y}{A_c f_{ck}}$, $\theta_1=\frac{A_S f_y}{A_c f_{ck}^*}$
A_c , A_s	Area of concrete and steel tube		
ρ_v	Stirrup ratio		
f_{sc}, f_{sc}'	Combined strength of CFST and RCFST, respectively	A_{sc}	Total area of RCFST, Asc=As+Ac
A_b	Total area of reinforcement in RCFST	f_b	Yield strength of reinforcement in RCFST

In this paper the behavior of RCFST members under axial compression bearing capacity is studied through the theoretical analysis, finite element simulation and experimental tests. A theoretical analysis model is developed by using the combined unified and limit equilibrium theories. The present theoretical analysis model is not only simple and convenient to use but also consistent with existing Chinese design codes [11] for CFST columns.

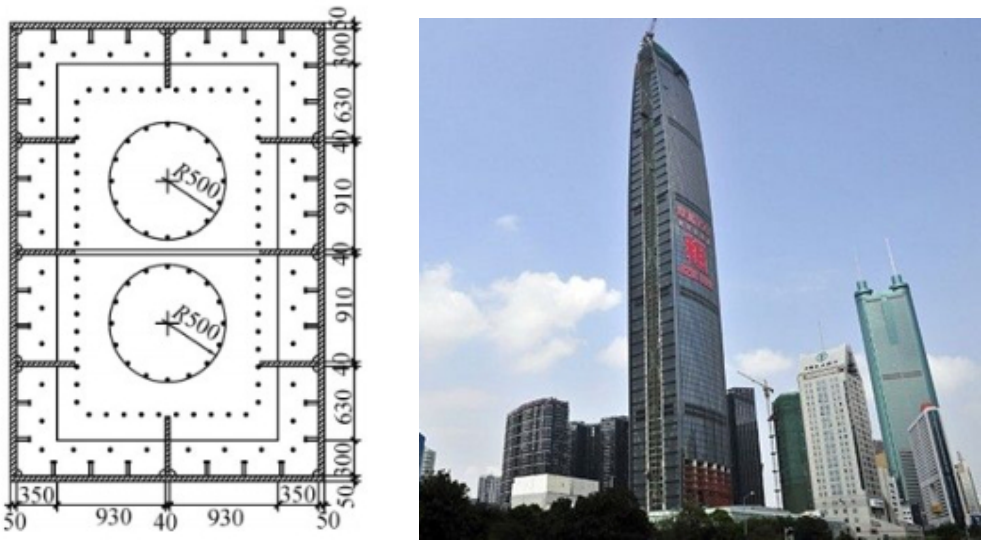

Figure 1. Typical Section of Steel Tube Column and Building Elevation of King Key Financial Center

2. THEORETICAL DERIVATION OF RCFST MEMBERS

In general, the concrete in RCFST is restrained by both the outside steel tube and inside stirrups as shown in Figure 2. The constraints will enhance the concrete compressive strength, which will be discussed separately in the following analyses.

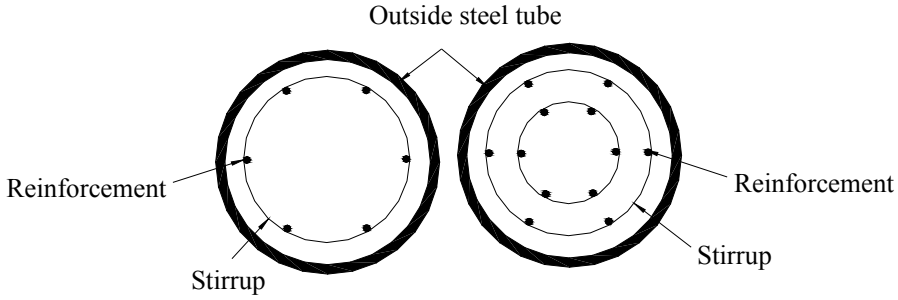

a) Single-layer reinforcement section b) Multilayer reinforcement section

Figure 2. Cross Section Diagram of RCFST

2.1 The Equivalent Strength of Core Concrete from Stirrups

According to the configuration of the reinforcement, the core concrete of a RCFST member can be treated as a single layer material or a multilayer material, as shown in Figure 3. Both cases will be discussed in this paper. The equivalent strengths of the core concrete in both cases are to be developed.

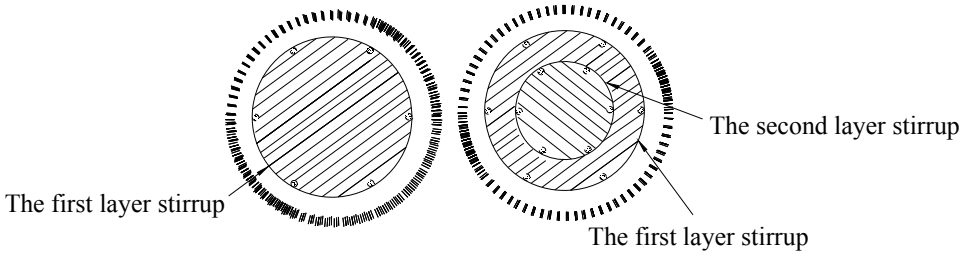

a) Single-layer reinforcement section b) Multilayer reinforcement section

Figure 3. Core Concrete Confined by Stirrups diagram of RCFST

2.1.1 The compressive strength of concrete confined by stirrups

(1) Axial compressive strength of concrete confined by single-layer stirrups

According to limit equilibrium theory from the theory of reinforcement concrete, if the spacing of spiral stirrups or welded stirrups is not larger than 80 mm and $d_s/5$ (where d_s is the diameter of the concrete column surrounded by stirrups), the strength improvement of core concrete due to the effect of stirrups should be considered (Slater et al. [21]), as shown in Figure 4.

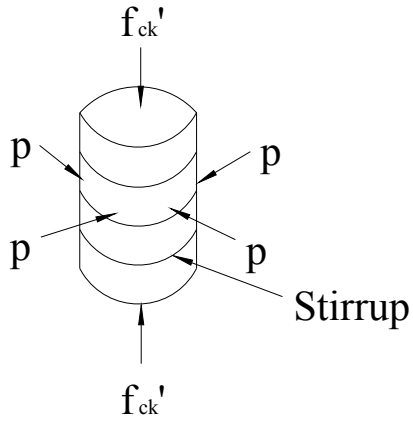

Figure 4. Concrete under Three-way Pressure

In this case, the longitudinal compressive strength of concrete confined by stirrups can be determined as follows:

$$f'_{ck} = f_{ck} + Kf_r \tag{1}$$

$$f_r = \frac{2A_{ss1} f_{yv}}{d_s s} \tag{2}$$

According to Eqs. 1, 2 and in general the lateral constraint coefficient is taken as K=4, it yields

$$f'_{ck} = f_{ck}(1 + \frac{2A_{ss0}}{A_{cor}} \cdot \frac{f_{yv}}{f_{ck}}) \tag{3}$$

Assuming ρ_v is the stirrup reinforcement ratio, the confining factor of steel tube θ can be defined as follows

$$\theta = \rho_v \cdot \frac{f_{yv}}{f_{ck}} \tag{4}$$

So the axial compressive strength of the confined single-layer concrete stirrup can be expressed as:

$$f'_{ck} = f_{ck}\left(1+2\theta\right) \tag{5}$$

(2) Axial compressive strength of concrete confined by multilayer stirrups

Concrete in a RCFST column of multilayer stirrups can be divided into i+1 parts, as the shadow part shown in Figure 3 (b). As far as the whole member is concerned, the effects of individual layer stirrups on the concrete can be calculated using a superposition method. Hence, the ferrule effect increases gradually from outside to inside.

Assuming that A_{ci} is the area divided by the i th and (i+1)-th layer stirrups, θ_i is the ferrule coefficient of the i th layer stirrups, A_{ssoi} is the equivalent reinforcement area of the i th layer stirrups, ρ_v is the stirrup ratio, and f_{cki} is the concrete strength restrained by the i th layer stirrup, Eq. 4 can be expressed as follows

$$\theta_i = \rho_v \cdot \frac{f_{yv}}{f_{ck}} = \frac{A_{ssoi}}{A_{ci}} \cdot \frac{f_{yv}}{f_{ck}} \tag{6}$$

when $i=1$, $f_{cki} = f_{ck}(1+2\theta_1)$ (7)

when $i>1$, $f_{cki} = f_{ck}(1+2\sum_{k=1}^{i}\theta_k)$ (8)

According to the above formulas, the compressive strength of concrete confined by the multilayer stirrups is equal to the ordinary concrete strength multiplied a stirrup enhancement coefficient.

2.1.2 Equivalent strength of core concrete within the outside steel tube

The total bearing capacity of concrete within the steel tube including plain concrete with no stirrups and the concrete confined by stirrups can be given by Eq. 9 , including the shadow and blank parts shown in Figure 3.

$$N_c = A_c f_{ck} + \sum_{i+1}^{n} A_{ci}\left(f_{cki} - f_{cki-1}\right) = A_c f_{ck} + 2\sum_{i=1}^{n} A_{ci} f_{ck}\theta_i \tag{9}$$

Substituting Eq. (6) into (9), it yields

$$N_c = A_c f_{ck} + 2\sum_{i=1}^{n} A_{ci} f_{ck} \frac{A_{ssoi}}{A_{ci}} \cdot \frac{f_{yv}}{f_{ck}} = A_c f_{ck} + 2 f_{yv} \sum_{i=1}^{n} A_{ssoi} = A_c f_{ck}\left(1+2\theta^*\right) \tag{10}$$

Since

$$\theta^* = \frac{f_{yv}\sum_{i=1}^{n} A_{ssoi}}{A_c f_{ck}} \tag{11}$$

Eq. 10 is simplified as follows

$$f_{ck}^* = \frac{N_c}{A_c} = f_{ck}\left(1+2\theta^*\right) \tag{12}$$

2.2 Axial Compression Bearing Capacity of RCFST by steel tube

2.2.1 Combined strength by steel tube

According to the CFST "*unified theory*" [13], the compressive strength of the CFST column can be expressed as follows:

$$f_{sc} = \left(1.212 + B\xi + C\xi^2\right) f_{ck} \tag{13}$$

The strength of concrete in Eq. 12 replacing 13, we have the formula of the combined strength of RCFST columns:

$$f_{sc}' = \left(1.212 + B_1\xi_1 + C_1\xi_1^2\right) f_{ck}^* = \left(1.212 + B_1\xi_1 + C_1\xi_1^2\right) f_{ck}\left(1+2\theta^*\right) \tag{14}$$

where, $\xi_1 = \frac{A_s f_y}{A_c f_{ck}^*}$, $B = B_1 = 0.1759\frac{f_y}{235} + 0.974$, $C = -0.1038\frac{f_{ck}}{20.1} + 0.0309$ and $C_1 = -0.1038\frac{f_{ck}^*}{20.1} + 0.0309$.

2.2.2 Axial compression bearing capacity

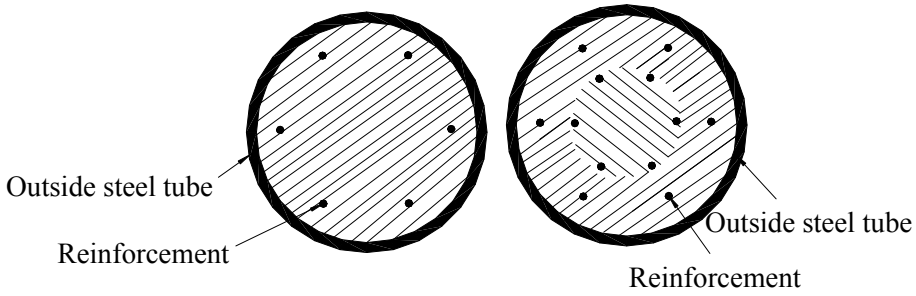

Figure 5. Cross Section Diagram of RCFST without Stirrup

According to superposition principle, the axial compression bearing capacity of RCFST members is obtained by the sum of the axial compression bearing capacity of longitudinal bar and CFST members confined by stirrups, as shown in Figure 5.

$$N_{scb} = A_{sc} f_{sc}' + A_b f_b = A_{sc}\left(1.212 + B_1\xi_1 + C_1\xi_1^2\right) f_{ck}\left(1+2\theta^*\right) + A_b f_b \tag{15}$$

The above description demonstrates that the axial compression bearing capacity of RCFST members is related to the ferrule coefficient of stirrups and steel tube, reinforcement ratio and strength of longitudinal reinforcement. If the ferrule coefficient or the reinforcement ratio becomes higher, the overall load-bearing capacity becomes stronger.

2.2.3 Compared with the formula of national code when it is CFST

When the reinforcement ratio is zero, the RCFST reduces to the CFST. Because $A_b = 0$ and $\theta^* = 0$, Eq. 15 is simplified into Eq. 16.

$$\begin{aligned} N_{scb} &= A_{sc} f'_{sc} + A_b f_b \\ &= A_{sc}\left(1.212 + B_1\xi_1 + C_1\xi_1^2\right) f_{ck} \\ &= A_{sc}\left(1.212 + B\xi + C\xi^2\right) f_{ck} \\ &= A_{sc} f_{sc} \end{aligned} \tag{16}$$

By comparing Eqs. 13 and 16, it can be seen that the formula of RCFST is in a good agreement with the formula recommended in Chinese design code for CFST members. Furthermore Eq. 15 can be regarded as an extension of the Chinese national design code for RCFST members.

3. FINITE ELEMENT SIMULATION OF RCFST MEMBERS

3.1 The material constitutive relation

Core concrete of RCFST is simulated by using the plastic-damage constitutive model (Ludovic et al. [22]). The uniaxial compressive stress-strain model of concrete is utilized as suggested by Hognestad (Jeffrey et al. [23]), which is simplified as the elastic-perfectly plastic model, as shown in Figure 6. Tensile in elastic part is similar with compressive parts, and the ultimate tensile strength is taken as one-tenth of the compressive strength. The steel model uses the bilinear model. Poisson's ratio is taken as 0.25 for concrete and 0.3 for steel.

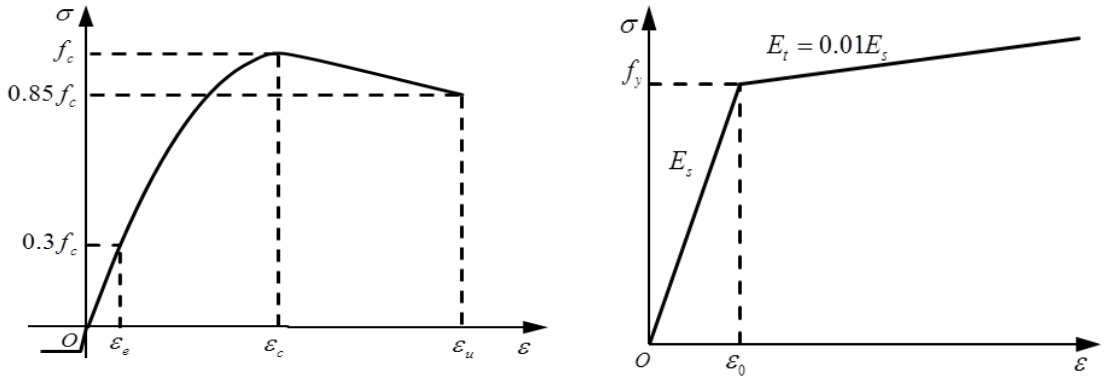

Figure 6. The Constitutive Relation of Concrete and Steel

3.2 The Finite Element Model

The three-dimensional solid element (C3D8R) is used to simulate the core concrete and steel tube of CFST members (Lu and Zhao [24]). The truss element (T3D2) is adopted to simulate the

unidirectional reinforced bars. For the convenience of applying boundary conditions, two rigid circular plates are used in the finite element analysis (FEA) model to simulate the upper and lower cover plates of the CFST member. All boundary conditions and loads are directly loaded on the rigid plates. Reinforced skeleton frame and concrete are contacted by using the Embedded region defined in ABAQUS. Element meshes of core concrete and reinforcement are shown in Figure7.

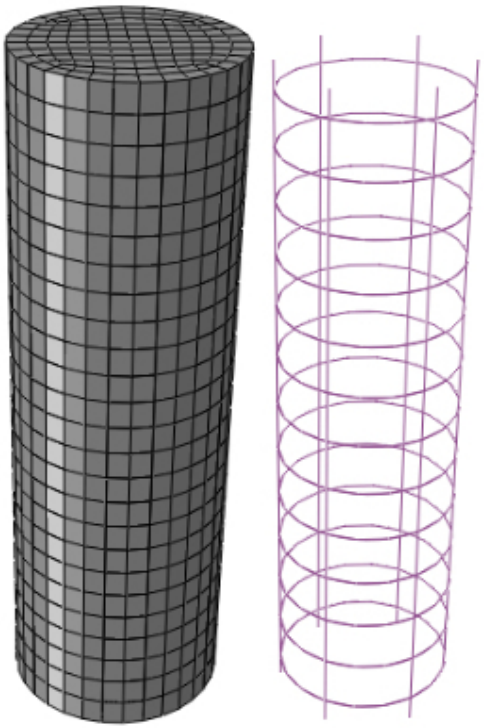

Figure 7. Model Meshes of Core Concrete and Reinforcement

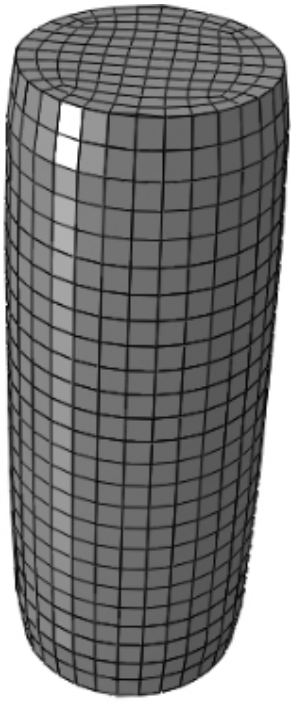

Figure 8. Deformation Model

Fixed displacement constraints are imposed to the bottom rigid plate. On the top rigid plate all other degrees of freedom except for the axial displacement are fixed. The axial loading is added on the center of the top plate. The problem is solved by using the displacement loading method.

3.3 Finite Element Results

Before the parametric analysis of the finite element analysis, finite element model is verified in this section. From the comparison between finite element simulation and its theoretical value under different parameters, it is found finite element value is slightly higher than the theoretical value, but the error is very small. Figure 8 plots a typical deformed shape of the RCFST column.

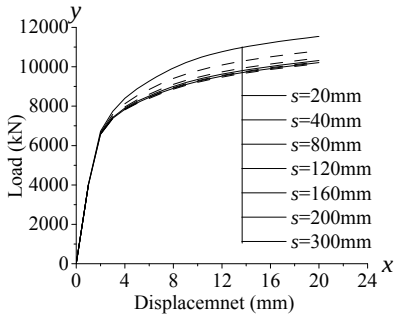

Figure 9. The Influence of Stirrup Spacing for Load-displacement Curve

Figure 9 shows the influence of the number of stirrups on the ultimate bearing capacity of the RCFST column (Wang [25]). It can be seen from the figure that the ultimate load increases with the decrease of the spacing of the stirrups. Table 1 gives a comparison of the finite element results with the theoretical values. Through the parameter analysis, it is found that the influence of the steel tube ferrule coefficient and slenderness ratio on the load-displacement curve of RCFST members are similar to CFST members.

According to the results of finite element simulation, reinforcement ratio, the strength of longitudinal reinforcement and the stirrup spacing are the key parameters, which should be considered in the experimental tests.

Table 1. Partial Value of Finite Element Simulation Compared with the Theoretical Value

Steel ratio α	Steel pipe intensity f_y (MPa)	Concrete strength f_{ck} (MPa)	Reinforcement ratio ρ_b	Longitudinal reinforcement intensity f_b (MPa)	Stirrup spacing s (mm)	Theoretical value N_c (kN)	Simulation value N_0 (kN)	N_0/N_c
0.080	235	33.5	0.027	335	80	9455	9757	1.032
0.080	235	40.2	0.027	335	80	10489	10732	1.023
0.080	235	46.9	0.027	335	80	11526	11657	1.011
0.080	345	20.1	0.027	335	80	8825	9039	1.024
0.080	390	20.1	0.027	335	80	9443	9581	1.015
0.080	420	20.1	0.027	335	80	9865	9942	1.008
0.019	235	20.1	0.027	335	80	5631	5598	0.994
0.039	235	20.1	0.027	335	80	6248	6367	1.019
0.059	235	20.1	0.027	335	80	6837	7066	1.034
				Mean value				1.028

4. AXIAL COMPRESSION TEST RESEARCH

4.1 General Situation of Test

4.1.1 Material

Tensile tests of reinforcement and steel tube were carried out by using hydraulic universal material testing machine. The sample size was determined according to the tensile test of metallic materials. The length of reinforcement specimens is 500 mm. Figure 10 shows some of the specimens tested for the steel tube and reinforcement. The specimens tested for concrete is shown in Figure 11 (Wang [25]), which is the standard cubic specimen of 150*150*150 mm.

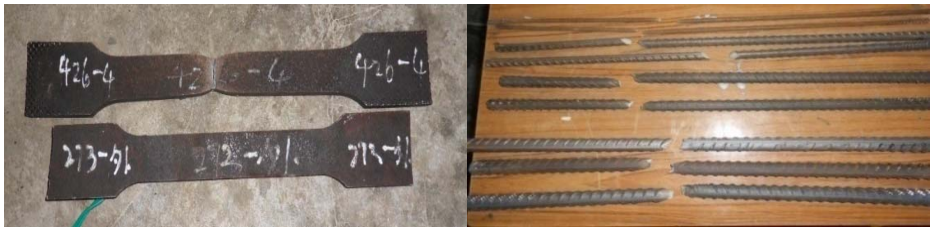

a) Steel tube specimens b) Reinforcement material specimens

Figure 10. Steel Specimens

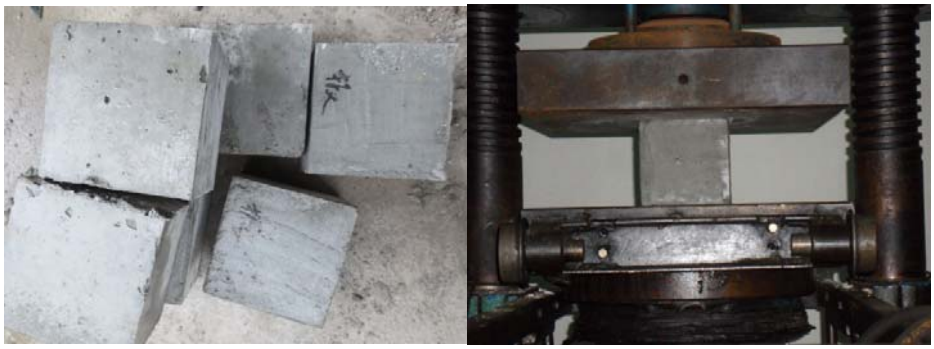

Figure 11. Concrete Standard Cube Specimens

The yield and ultimate strengths for the steel were obtained in the steel tensile tests, which show that both the steel tube and reinforcement have very good ductility. The concrete cubic compressive strength f_{ck} is used to calculate the compressive strength of the prism by using : $f_{ck} = k_2 f_{cu,k}^{150}$ (where k_2 is the conversion factor， for ordinary strength concrete, $k_2 = 0.67$).

4.1.2 Specimens

The axial compressive tests included CFST specimens and RCFST specimens, and all steel tubes were of the same size. RCFST specimens were divided into three groups according to the strength of internal longitudinal reinforcement, and there were three kinds of longitudinal reinforcement ratios and two stirrup spacings in each group specimens. The section size of the cover plates was 500mm × 500mm, with an identical thickness of 16 mm. All parameters of specimens are listed in Table 2.

The experiment was carried out in architecture lab of South China University of Technology. The specimens were made by the procedure: (1) fabrication of steel reinforcement cage, (2) welding reinforcement to the bottom plate, (3) welding steel tube to the bottom plate, (4) pouring concrete into the steel tube. During the casting of concrete, a 50 mm plug-in vibrator was used to vibrate the concrete. After the concrete is casted, the specimen was cured for 12 hours in an environment with fixed temperature and humidity conditions. After the concrete was cured, the top steel plate was welded to the specimen (Jamaluddin et al. [26]).

Table 2. Parameters of the Specimens under Axial Compression

Sample number	D (mm)	t (mm)	L (mm)	f_y (MPa)	f_{cu} (MPa)	f_b (MPa)	f_{yv} (MPa)	ρ_b	s (mm)
A-1	426	8	1300	297	28.24	-	-	0	-
A1-6-1	426	8	1300	297	28.24	414	314	1.73%	100
A1-10-1	426	8	1300	297	28.24	414	314	2.88%	100
A1-10-2	426	8	1300	297	28.24	414	314	2.88%	50
A1-12-1	426	8	1300	297	28.24	414	314	3.45%	100
A2-6-1	426	8	1300	297	28.24	485	314	1.73%	100
A2-10-1	426	8	1300	297	28.24	485	314	2.88%	100
A2-10-2	426	8	1300	297	28.24	485	314	2.88%	50
A2-12-1	426	8	1300	297	28.24	485	314	3.45%	100
A3-6-1	426	8	1300	297	28.24	532	314	1.73%	100
A3-10-1	426	8	1300	297	28.24	532	314	2.88%	100
A3-10-2	426	8	1300	297	28.24	532	314	2.88%	50
A3-12-1	426	8	1300	297	28.24	532	314	3.45%	100

Note: In the table, D is the cross-section diameter of the specimen, t is thickness the steel tube L is the length of members, f_y is the yield strength of steel, f_{cu} is the cube crushing strength of concrete, f_b is yield strength of the longitudinal reinforcement, f_{yv} is the yield strength of stirrup, ρ_b is the ratio of longitudinal reinforcement, s is the stirrup spacing.

4.1.3 Test procedure

(1) The test instrument and equipment Axial compression tests were performed in the 1500T hydraulic pressure testing machine, as shown in Figure 12. Collecting device of strains and displacements was DH3816 static strain gauge.

(2)

Figure 12. 1500T Hydraulic Pressure Testing Machine

(2) Loading and data acquisition In the axial compression test, the parameters needed to determine were the longitudinal stress-strain relationship of reinforcement, the stress-strain relationship of the steel tube in both the longitudinal and hoop directions. In order to obtain the required parameters, four groups of strain gauges were placed on the middle of the external surface of the steel tube, which were purposed to measure the longitudinal and hoop strains (see Figure 13).

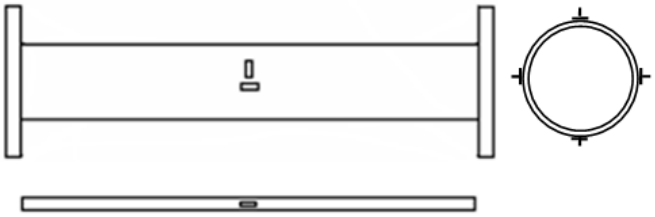

Figure 13. Strain Gauge Arrangement of Steel Tube and Reinforcement

In addition, four internal longitudinal strain gauges were used to measure the axial tension and compression strain of longitudinal reinforcement (Nie et al. [27]). To determine the axial and lateral displacements of the specimens, two axial displacement meters and two lateral displacement meters were placed in the middle of the column (Hou et al. [28]).

4.2 Experimental Results

In the axial compression test process, short columns generally do not fall, so when the axial displacement component reaches a certain extent or when the axial deformation is large, the test is stopped or unloaded.

Figure 14. Slip Line and Failure State

The experimental phenomenon (Figure 14) shows that the damage form of RCFST specimens is neither bending failure nor shear failure, but the local buckling. The examination of the internal concrete shows that there is no evidence of debonding from the steel tube although concrete crushing in some places.

A detailed comparison of the theoretical, finite element analysis and experimental results of the short column is given in Table 3. It can be seen from Figure 15 that the ductility of the RCFST members is better than that of CFST members. For such good ductile structural members it is general to take the compressive load at the strain value of 0.0035 as the bearing load of the member (Degtyarev [29]).

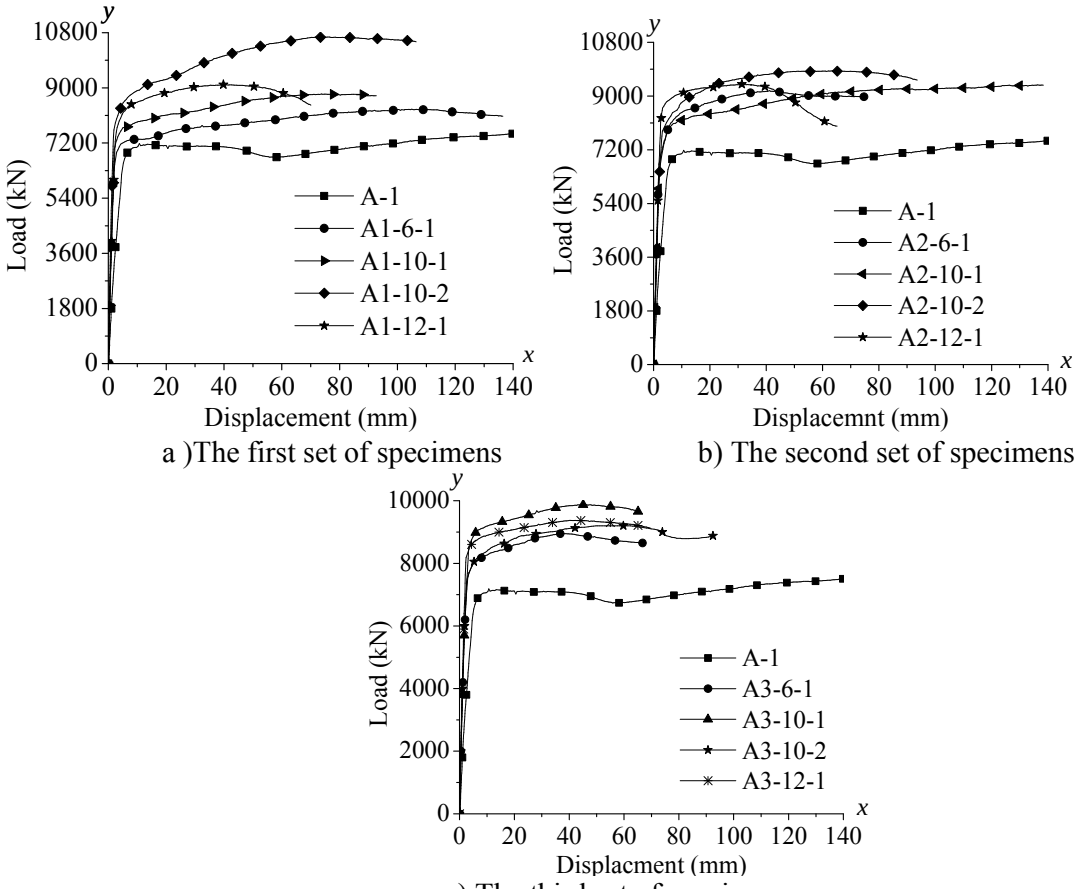

a)The first set of specimens

b) The second set of specimens

c) The third set of specimens

Figure 15. Loading-displacement Curve of RCFST Short Columns

Table 3. Axial Compression Bearing Capacity of Short Columns

Specimen number	Theoretical value N_c (kN)	Finite element value N_0 (kN)	Trial value N_e (kN)	N_c/N_0	N_c/N_e
A1-1	6760	6791	6826	0.996	0.990
A1-6-1	8042	8045	8302	1.000	0.969
A1-10-1	8637	8676	8797	0.995	0.982
A1-10-2	9056	9077	9946	0.998	0.911
A1-12-1	8934	8999	9215	0.993	0.970
A2-6-1	8204	8205	8896	1.000	0.922
A2-10-1	8907	8943	9375	0.996	0.950
A2-10-2	9326	9344	9847	0.998	0.947
A2-12-1	9258	9320	9400	0.993	0.985
A3-6-1	8311	8311	8748	1.000	0.950
A3-10-1	9085	9118	9594	0.996	0.947
A3-10-2	9505	9521	9388	0.998	1.012
A3-12-1	9473	9532	9488	0.994	0.998
Mean value				0.997	0.964

5. CONCLUSIONS

This paper has presented the theoretical, numerical and experimental investigations on the ultimate bearing load capacity of RCFST columns. The theoretical study is performed by using the combined unified and limit equilibrium theories. The numerical study is done by using the finite element method. The theoretical and FEA results are validated by the experimental data. From the results obtained the following conclusions can be drawn:

1) Addition of longitudinal reinforcement in RCFST short columns can significantly increase the bearing capacity of the columns, in which both longitudinal reinforcement and stirrups play important role in this strength increase.

2) Short columns are neither in bending failure nor in shear failure, but in the local buckling failure of the steel tube.

3) The proposed theoretical formula for calculating the compressive strength of RCFST columns is consistent with existing design code for CFST columns. That is, it reduces to the design formula of CFST when the reinforcement ratio is 0.

REFERENCES

[1] Han, L.H. and An, Y.F., "Performance of Concrete-encased CFST Stub Columns under Axial Compression", Journal of Constructional Steel Research, 2014, Vol. 93, pp. 62-76.

[2] Yu, M. at al., "A Unified Formulation for Circle and Polygon Concrete-filled Steel Tube Columns under Axial Compression", Engineering Structures, 2013, Vol. 49, pp. 1-10.

[3] Dundu, M., "Compressive Strength of Circular Concrete Filled Steel Tube Columns", Thin-Walled Structures, 2012, Vol. 56, pp. 62-70.

[4] Dai, X. and Lam, D., "Numerical Modelling of the Axial Compressive Behaviour of Short concrete-filled Elliptical Steel Columns", Journal of Constructional Steel Research, 2010, Vol. 66, pp. 931-942.

[5] Yu, T., Hu, Y.M. and Teng, J.G., "FRP-confined Circular Concrete-filled Steel Tubular Columns under Cyclic Axial Compression", Journal of Constructional Steel Research, 2014, Vol. 94, pp. 33-48.
[6] Prabhu, G.G and Sundarraja, M.C., "Behaviour of Concrete Filled Steel Tubular (CFST) Short Columns Externally Reinforced using CFRP Strips Composite", Construction and Building Materials, 2013, Vol. 47, pp. 1362-1371.
[7] Wang, Y.H., Nie, J.G. and Fan, J.S., "Theoretical Model and Investigation of Concrete Filled Steel Tube Columns under Axial Force–torsion Combined Action", Thin-Walled Structures, 2013, Vol. 69, pp. 1-9.
[8] Ma, H. et al., "Seismic Performance of Steel-reinforced Recycled Concrete Columns under Low Cyclic Loads", Construction and Building Materials, 2013, Vol. 48, pp. 229-237.
[9] Zhong, S.T and Tu, Y.Q., "The Study of Dynamics Behavior of Concrete Filled Steel Tubular (CFST) Members", In Advances in Steel Structures, 1996, pp. 449-454.
[10] Abdalla, S. and Abed, F., "Mohammad AlHamaydeh, Behavior of CFSTs and CCFSTs under Quasi-static Axial Compression", Journal of Constructional Steel Research, 2013, Vol. 90, pp. 235-244.
[11] GB 50936-2014. Technical Code for Concrete Filled Steel Tubular Structures. (in Chinese)
[12] Liu, S.W., Liu, Y.P. and Chan, S.L., "Advanced Analysis of Hybrid Steel and Concrete Frames, Part 1: Cross-section Analysis Technique and Second-order Analysis", J. Constr. Steel Res., 2012, Vol. 70, pp. 326-336.
[13] Liu, S.W., Liu, Y.P. and Chan, S.L., "Advanced Analysis of Hybrid Steel and Concrete Frames, Part 2: Refined Plastic Hinge and Advanced Analysis", J. Constr. Steel Res., 2012, Vol. 70, pp. 337-349.
[14] Lie, T.T., "Fire Resistance of Circular Steel Columns Filled with Bar-Reinforced Concrete", Journal of Structure Engineering, 1994, Vol. 120, No. 5, pp. 1489-1509.
[15] Chang, X., Wei, Y.Y. and Yun, Y.C., "Analysis of Steel-reinforced Concrete-filled-steel Tubular (SRCFST) Columns under Cyclic Loading", Construction and Building Materials, 2012, Vol. 28, No. 1, pp. 88-95.
[16] Zhu, M.C., et al., "Experimental Research on Square Steel Tubular Columns Filled with Steel-reinforced Self-consolidating High-strength Concrete under Axial Load", Engineering Structures, 2010, Vol. 32, No. 8, pp. 2278-2286.
[17] Wei, H., et al., "Study on Strength of Reinforced Concrete Flled Circular Steel Tubular Columns", Structural Engineering and Mechanics, 2005, Vol. 19, No. 6, pp. 653–657.
[18] Wang, H.J., et al., "Experimental Study on Twin-column RCFT Pier", Conf. on Advances in Structural Engineering and Mechanics, Busan (Pusan), Korea, 2002.
[19] Endo, T. et al. "Experimental study on reinforced concrete filled steel tubular structure", Conf. on Steel Structures, Singapore, 2000, Proc.7th Int.
[20] Xiamuxi, A. and Hasegawa, A., "A Study on Axial Compressive Behaviors of Reinforced Concrete Filled Tubular Steel Columns", Journal of Constructional Steel Research, 2012, Vol. 76, pp. 144-154.
[21] Slater, W.A., Richart, F.E. and Scofield, G.G., "Tests of Bond Resistance between Concrete and Steel", Journal of the Franklin Institute, Phlebol-Ann Vasc, 1920, Vol. 190, pp. 885-886.
[22] Ludovic, J., et al., "An Elastic Plastic Damage Formulation for Concrete: Application to Elementary Tests and Comparison with an Isotropic Damage Model", Computer Methods in Applied Mechanics and Engineering, 2006, Vol. 195, Issue 52, pp. 7077-7092.
[23] Jeffrey, M., et al., "Reconsidering the Use of High-strength Reinforcement in Concrete Columns", Engineering Structures, 2012, Vol. 37, pp. 135-142.
[24] Lu, Z.H. and Zhao, Y.G., "Suggested empirical models for the axial capacity of circular CFT stub columns", Journal of Constructional Steel Research, 2010, Vol. 66, Issue 6, pp. 850-862.

[25] Wang, N., Static and Dynamic Performance Research of Bar-reinforce Concrete Filled Steel Tubular Component [D]. 2013, Shenzhen: Harbin Institute of Technology. (in Chinese)
[26] Jamaluddin, N. et al., "An experimental study on elliptical concrete filled columns under axial compression", Journal of Constructional Steel Research, 2013, Vol. 87, pp. 6-16.
[27] Nie, J.G, Wang, Y.H. and Fan, J.S., "Experimental Research on Concrete Filled Steel Tube Columns under Combined Compression-bending-torsion Cyclic Load", Thin-Walled Structures, 2013, Vol. 67, pp. 1-14.
[28] Hou, C., Han, L.H. and Zhao, X.L., "Concrete-filled Circular Steel Tubes Subjected to Local Bearing Force: Experiments", Journal of Constructional Steel Research, 2013, Vol. 83, pp. 90-104.
[29] Degtyarev, V.V., "Strength of Composite Slabs with End Anchorages, Part I: Analytical Model", Journal of Constructional Steel Research, 2013.

STRESS INTENSITY FACTORS OF TUBULAR T/Y-JOINTS SUBJECTED TO THREE BASIC LOADING

S.T. Lie[1,*], T. Li[1] and Y.B. Shao[2]

[1]*School of Civil and Environmental Engineering, Nanyang Technological University, 50 Nanyang Avenue, Singapore 639798*
[2]*School of Civil Engineering, Yantai University, Yantai City 264005, P. R. China*
**(Corresponding author: E-mail: cstlie@ntu.edu.sg)*

Received: 30 July 2014; Revised: 17 June 2015; Accepted: 3 July 2015

ABSTRACT: This paper describes the determination of stress intensity factors (SIFs) of a 3D surface crack in a circular hollow section (CHS) T/Y-joint subjected to three basic loading. In order to achieve the main objective, an automatic finite element (FE) mesh generator is designed whereby the mesh density and element type of the Crack Tube zone can be controlled by the users. Extensive tests are carried out to check the accuracy and to test the convergence of the mesh models. It is found that the generated mesh models are both accurate and robust. Subsequently, a total of 246 cracked CHS T/Y-joints subjected to axial loading; in-plane bending and out-of-plane bending are analysed, and the influencing parameters β, γ, τ, θ, a/t_0 and c/a on the SIFs of a 3D surface crack are investigated in this study. The SIFs at the deepest point of a 3D surface crack are also determined using an indirect method incorporated in BS7910. It is found that the later underestimates the SIFs by as much as -36.9% under axial load for crack located at the crown and -32.9% under out-of-plane bending for crack located at the saddle, respectively. Hence, the indirect method is found to be unsafe in estimating the SIFs of a 3D surface crack in CHS T/Y-joints under certain loading conditions and crack location.

Keywords: Finite element analysis, Mesh generation, 3D Surface crack, Stress intensity factor, Tubular T/Y-joint

DOI: 10.18057/IJASC.2016.12.2.3

1. INTRODUCTION

Stress intensity factor (SIF) is an important fracture parameter frequently used to estimate the fatigue life and to predict the fracture behaviour of a cracked component. As there are no analytical solutions available in the literature to determine the SIFs along the crack front of a 3D surface crack in a circular hollow section (CHS) joint, many researchers have to depend on the finite element (FE) method. The accuracy and convergence of the computed SIFs are influenced very much on the mesh quality of the generated FE mesh models particularly along the crack front and near the crack ends. It has a significant impact on the accuracy of the SIFs. For crack tips further away from the crack ends where the crack front intersects with the weld toe, SIFs can be determined accurately using *J*-integral and displacement extrapolation methods under the square root singularity assumption (Shivakumar and Raju [1], Madia et al. [2]). However, this is not the case for SIFs at the crack ends due to boundary layer effect. More evidence indicates that square root singularity assumption is not valid at the crack ends of a surface crack (Hutař and Náhlík [3], Heyder et al. [4]). Hence, both *J*-integral and displacement extrapolation methods cannot produce accurate SIFs exactly at the crack ends of a surface crack. The singularity at the crack ends of a surface crack is still being investigated by researchers (Madia et al. [2], Hutař and Náhlík [3], Heyder et al. [4]). Therefore, this study focus only on the calculation of SIFs at the crack tips farther away from the crack ends.

For the past decades, many researchers had developed their special purpose automatic FE mesh generators (Huang and Hancock [5], Rhee [6], Bowness and Lee [7, 8], Cao et al. [9], Lie et al. [10], Chiew et al. [11]) as it is a daunting task to manually create the mesh models of the 3D surface crack in any CHS joint. Among of these researchers, Bowness and Lee [7, 8], Lie et al. [10] and Chiew et al. [11] had carried out extensive analyses on the SIFs of CHS T/Y-joints taking advantage of their own mesh generators. However, due to the limitations of their mesh generators, all the works done so far focus only on cracked CHS T-joints subjected to axial loading, and there are no published reports on SIFs of cracked CHS T/Y-joints subjected to in-plane bending and out-of-plane bending.

In addition to FE analyses, some researchers had carried out experimental tests on full-scale specimens to determine the SIFs of cracked CHS T-joints. Peter [12] carried out fatigue tests on high strength steel CHS T-joints under different axial loading. The crack propagation was monitored by the alternating current potential drop (ACPD) technique, and the SIFs at the deepest point were derived in conjunction with the Paris' crack propagation law. Shao and Lie [13] carried out similar fatigue tests on two full-scale CHS K-joints subjected to balanced axial loading and derived the SIFs using the same approach. In practice, it is very costly and time-consuming to carry out such large scale fatigue tests. Hence, it is not feasible to carry out extensive experimental tests to study the SIFs of cracked CHS T/Y-joints subjected to different loading cases.

Apart from numerical method and experimental test, there is an alternative method called the indirect method which can be used to calculate SIFs in a CHS joint. This indirect method has been incorporated in BS7910 [14], and it is based on a central cracked flat plate model subjected to tension and bending loading. The SIFs of a surface crack are calculated first by using the well-established Newman-Raju [15, 16] equation. Then, by incorporating the effects of the weld profile, local hot spot stress and local degree of bending (Lee and Bowness [17]), the flat plate model can be used to estimate the SIFs of any cracked CHS T/Y-joint containing a surface crack. Lie et al. [18] had applied it to CHS K-joints subjected to balanced axial loads, and found that it overestimates the SIFs by as much as 190.4% at the crack deepest point. This indirect method has not been tested extensively on CHS T/Y-joints subjected to in-plane bending and out-of-plane bending.

Hence, in this study, FE analysis is used to study the SIFs of cracked CHS T/Y-joints subjected under different loading conditions. A new FE mesh generator is developed to create the mesh models. Firstly, element types, mesh design of the surface crack front and mesh refinement schemes are presented. Secondly, the boundary conditions and loading types applied are introduced. Finally, mesh convergence test and verification of the FE mesh models are carried out. Subsequently, the SIFs of 246 cracked CHS T/Y-joints subjected to three basic loading are calculated. The influencing parameters β, γ, τ, θ, a/t_0 and c/a on the shape factors (dimensionless stress intensity factor) are investigated. Finally, the accuracy of the shape factors estimated using the indirect method incorporated in BS7910 [14] is examined and compared with the SIFs calculated using the present FE mesh models.

2. GEOMETRY OF T/Y-JOINT

Figure 1 shows the dimensionless parameters α, β, γ, τ, and θ of a CHS T/Y-joint subjected to three basic loading. If the angle θ is not equal to 90^o, then the joint is considered as a Y-joint. It is common to group and denote such a T-joint and Y-joint as a T/Y-joint in practice. The range of geometries and crack shapes of the analyzed cracked CHS T/Y-joints are listed in Table 1. The chord thickness of all the cracked CHS T/Y-joints is 10 mm, and all the other parameters used to

define the joint can be derived from Figure 1. The surface crack is located at the weld toe on the chord side of the hot spot stress location, and its value is obtained using the SCF equations recommended in API-RP-2A [19]. The Young's modulus and Poisson's ratio are 210 GPa and 0.3, respectively

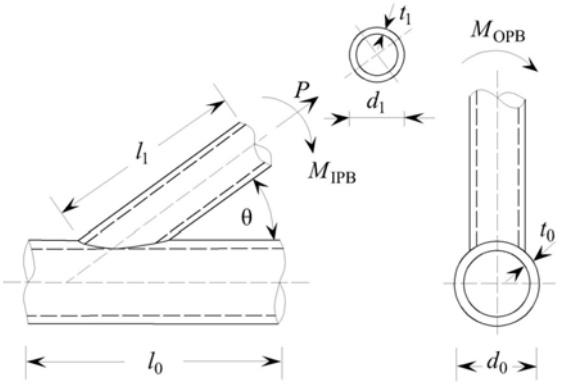

$\alpha=2l_0/d_0$; $\beta=d_1/d_0$; $\gamma=d_0/2t_0$; $\tau=t_1/t_0$

Figure 1. Geometry and Notations of a CHS T/Y-joint Subjected to Three Basic Loading

Table 1. Crack Shapes and Geometries of CHS T/Y-joints

Group	1	2	3
α	14	24	14
β	0.3~0.8	0.8	0.3~0.8
γ	8~26	8	8~ 26
τ	0.4~1.0	0.6	0.4~1.0
θ	30^0 ~90^0	30^0~90^0	30^0~ 90^0
a/t_0	0.2~0.8	0.2~0.8	0.2~0.8
c/a	3~10	3 ~10	3~10
Loading type	Axial, OPB	Axial	IPB
Crack location	Saddle	Crown	Crown

3. FINITE ELEMENT MESH GENERATION

In this section, FE mesh generation of cracked CHS T/Y-joints is introduced. Several important key points of the mesh generation are highlighted, including element types, mesh design of the surface crack front, and mesh refinement schemes. In addition, the double mapping approach used to generate FE mesh models of cracked CHS T/Y-joints is also briefly introduced in this section.

3.1 Element Selection

There are two types of solid elements, i.e. 20-nodes hexahedron and 15-nodes collapsed prism elements are used and shown in Figure 2. For the 15-nodes collapsed prism element, the middle nodes at element edges intersecting with the crack front are moved to the quarter position to produce the square root singularity. The collapsed prism elements are only used along the surface crack front.

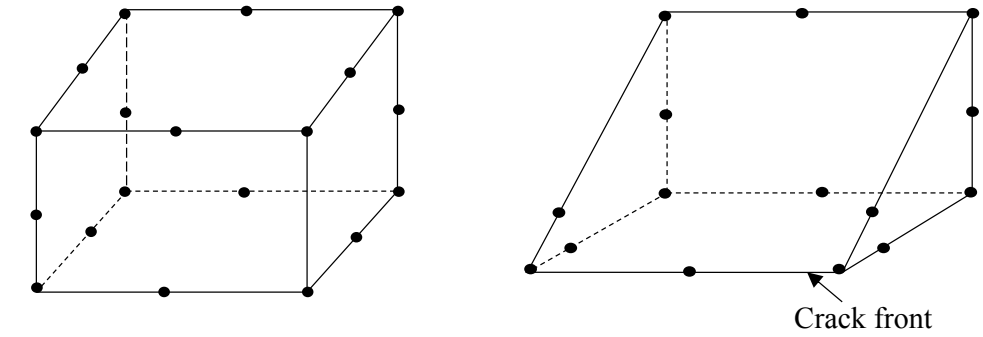

Figure 2. Solid Elements Used in FE Mesh Models

3.2 Mesh Generation

The surface crack block containing the crack front is generated by double mapping a 2D plain surface crack as shown in Figure 3. It can be seen that the zone is divided into three parts, including Part A, Part B and Crack Tube where the crack front is located.

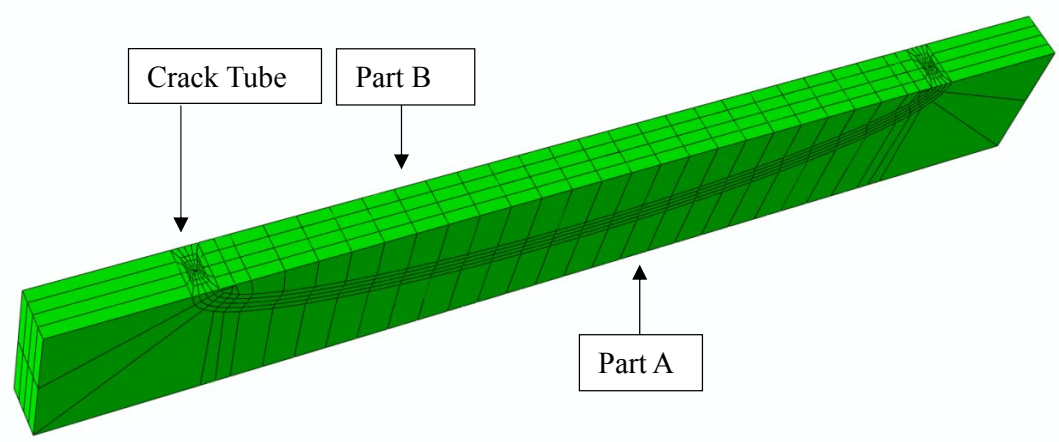

Figure 3. Mesh Design of the 2D Surface Crack Block in a Central Cracked Plain Plate

Figure 4 shows the internal mesh design by cutting a cross-section through the Crack Tube at the crack tip. It can be seen that 16 elements surrounding the crack tips are used, and they share a node at the crack tip. For this case, the number of element rings enclosing the crack tips is 4. In the new mesh generator, the number of element rings is set as a variable so that it is easy to refine the mesh along the crack front and check the path independence of the *J*-integral. Figure 4 indicates the dimensions of the cutting cross-section of the Crack Tube.

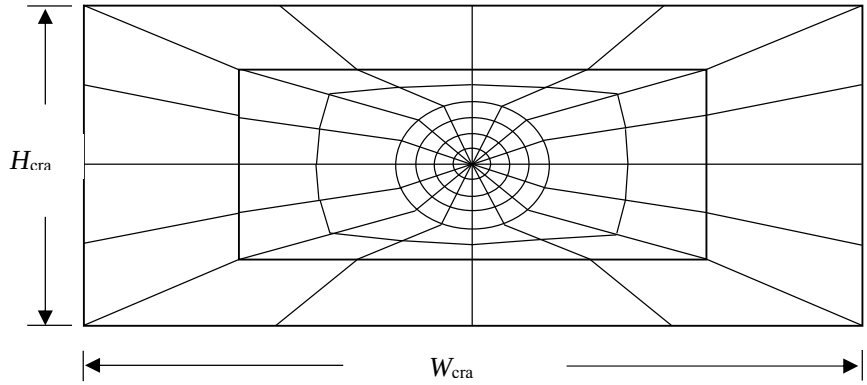

Figure 4. Mesh Design of Cutting Cross-section of Crack Tube at Crack Tip

The mesh model of the Crack Tube is created using a sweep technique. Firstly, the Crack Tube is cut into sufficient segments along the crack front and the cutting cross-sections are set perpendicular to the tangent along the crack front at the cutting points. Then, nodes are inserted on the cutting cross-sections, creating elements of the Crack Tube simultaneously. By sweeping the cutting cross-section shown in Figure 4 along the surface crack front, 3D-coordinates of nodes are determined. Finally, dimensions of certain cutting cross-sections are reduced to form transition elements (Figures 5 and 6). The mesh generation of Part A and Part B are quite straightforward and will not be discussed herein.

After the surface crack block shown in Figure 3 is generated, FE mesh model of a cracked T-butt joint can be produced by adding a vertical attachment and the fillet weld on a central cracked plain plate. Subsequently, the chord-brace intersection zone can be created using the double mapping approach shown in Figure 7. After all the mesh models of the other sub-zones are completed, they are merged with the chord-brace intersection zone to form the completed FE mesh model of a cracked CHS T/Y-joint. The detailed derivation of coordinate transformation can be found in Ref. [20]. Figure 8 shows a typical completed mesh model of such a cracked CHS T/Y-joint for $\theta=60^{o}$.

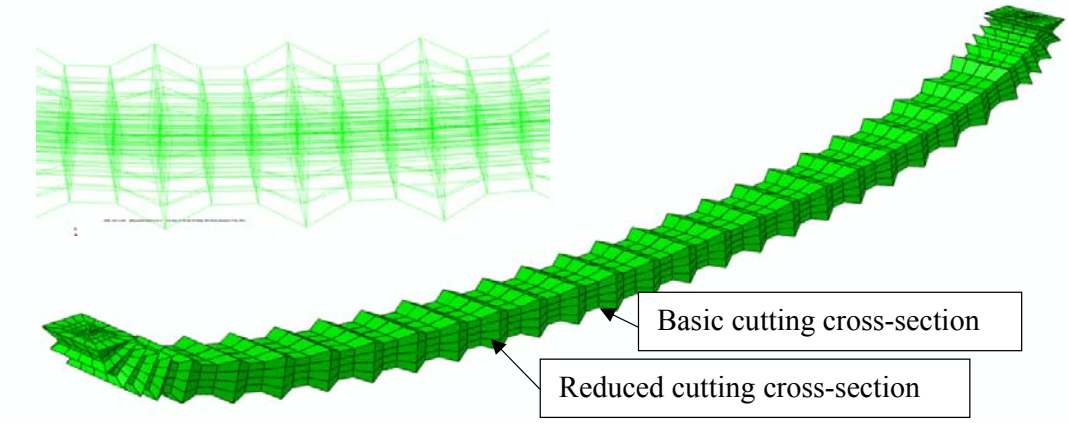

Figure 5. Mesh Design of Crack Tube Created Using a Sweep Process

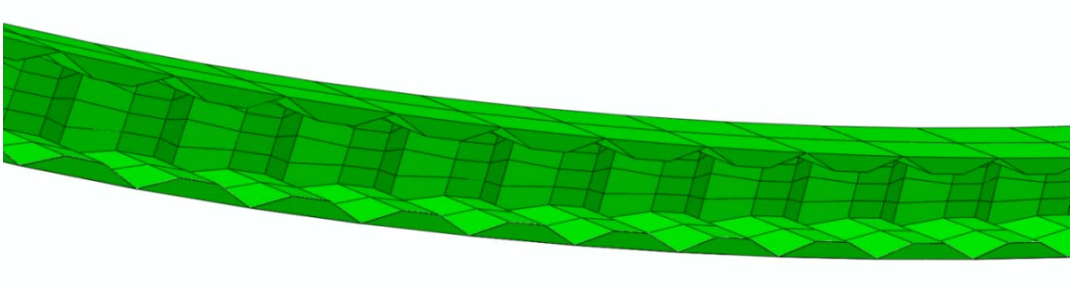

Figure 6. Transition Elements of Crack Tube Through Thickness Direction

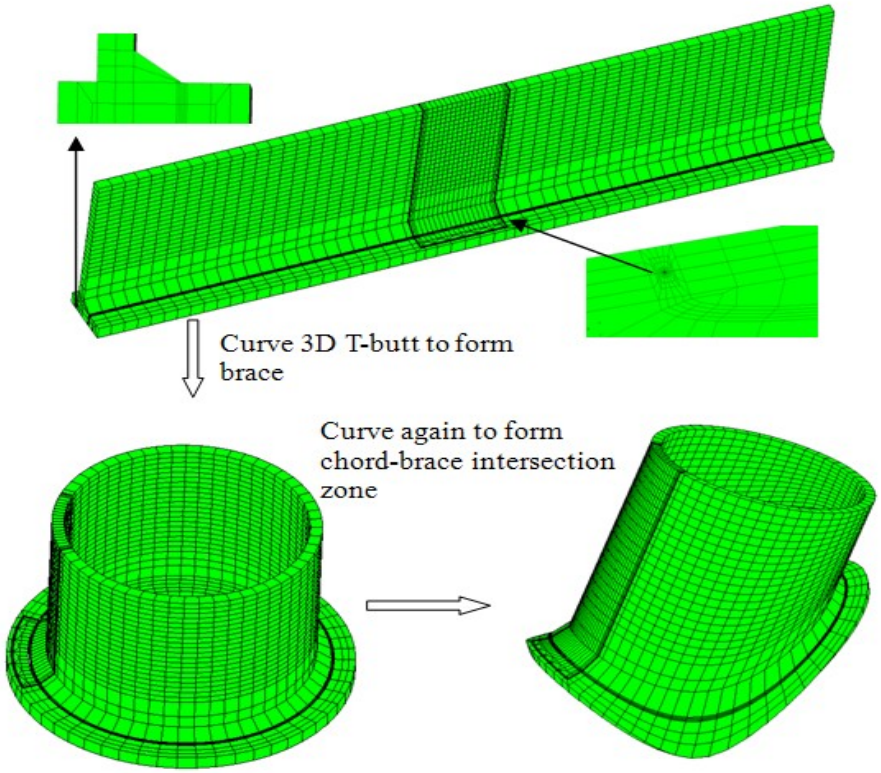

Figure 7. Double Mapping a T-butt to Form Chord-brace Intersection Zone

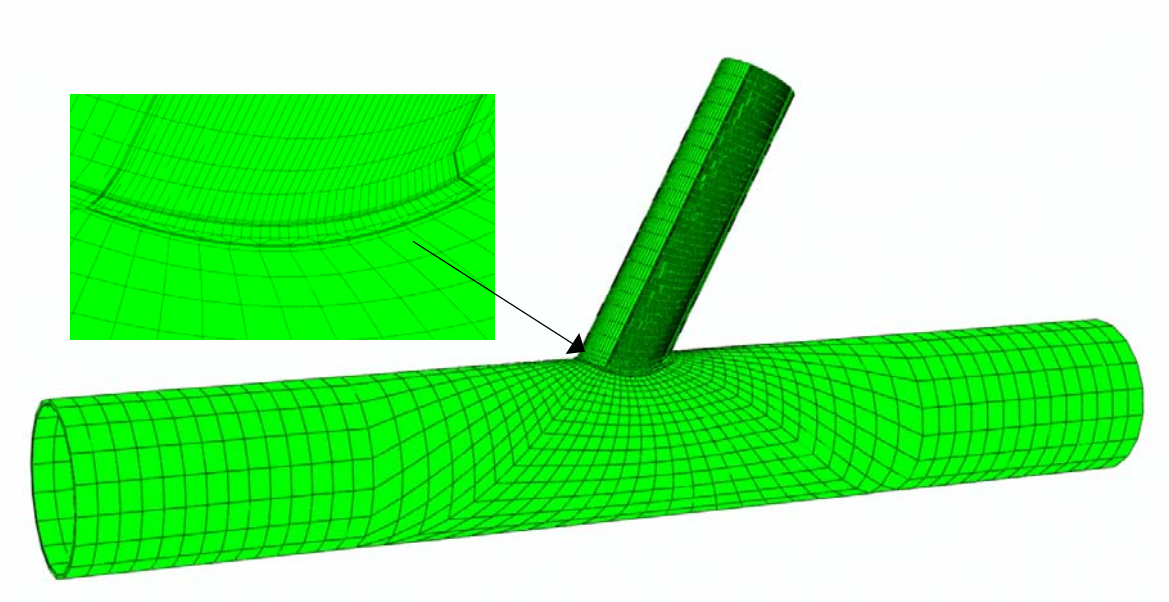

Figure 8. Completed Mesh Model of a Cracked CHS T/Y-joint (θ=60^o)

3.3 Mesh Refinement Schemes

In order to improve the accuracy of the SIF results, two types of mesh refinement schemes are adopted in the new mesh generator. The first type is used to refine the local mesh of the Crack Tube. Element rings enclosing the crack front and the number of divisions (number of cutting cross-sections) along the crack front are set as two variables so that it is easy to refine the mesh of the Crack Tube. The second type is used to refine the global mesh of the entire chord. Number of divisions along the chord-brace intersecting curve is set as a variable. It has been validated that a minimum of 40 divisions along the chord-brace intersecting curve is sufficient to capture the stress distribution at the chord-brace intersection zone of a typical CHS joint (Chiew et al. [11], Shao and Lie [13]). In practice, the crack depth and length of a surface crack can vary widely. If the crack depth is relatively shallow such as a/t_0 = 0.2, the dimensions of the Crack Tube, W_{cra} and H_{cra} indicated in Figure 4 must be sufficiently small so as to avoid affecting the mesh of Part B of the surface crack block. For shallower surface crack, the mesh transition between the Crack Tube and Part A is critical as element size of Part A is significantly larger than elements of the Crack Tube. This may bring uncertain effect on the accuracy of the SIF results. In order to smooth the mesh transition between the Crack Tube and Part A, a novel mesh refinement scheme is designed to increase the element layers at Part A. Figure 9 shows one application of such mesh refinement scheme with 4 element layers at Part A. Simultaneously, number of element layers of the entire chord along its thickness direction is increased to 4 so that the global mesh of the chord is refined. The number of element layers at Part A is also set as a variable in the new mesh generator.

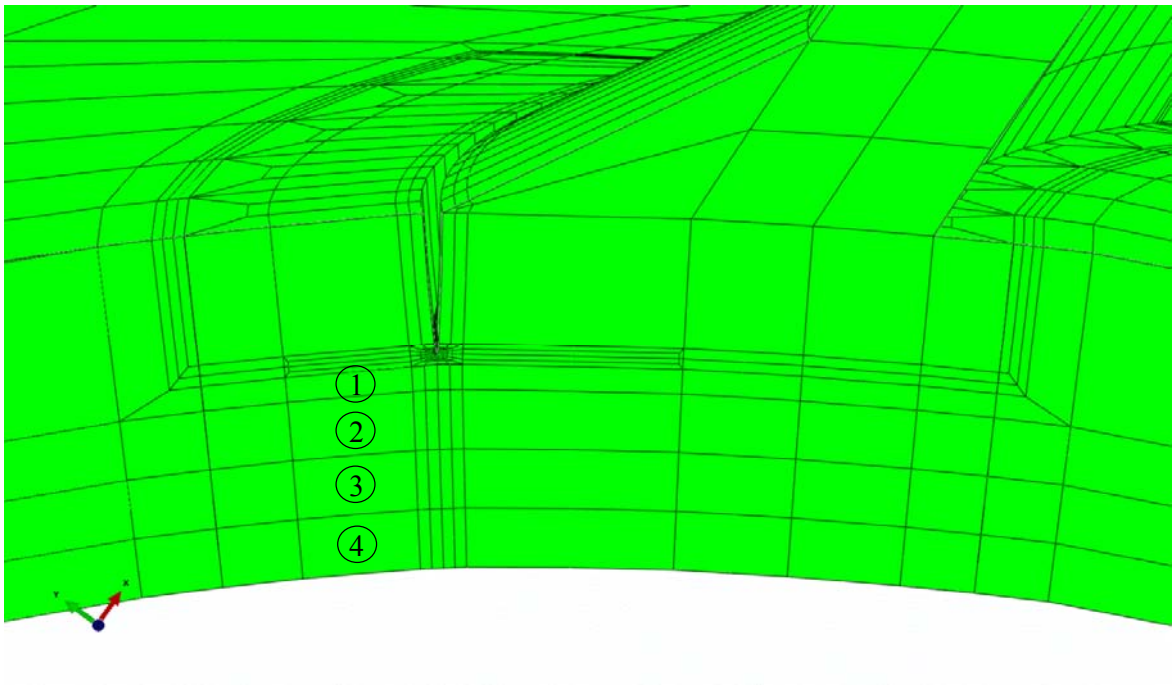

Figure 9. Mesh Refinement Scheme at Part A

4. BOUNDARY CONDITION AND LOADING

In this section, the boundary conditions of a cracked CHS T/Y-joint and the three types of loading applied are introduced and their magnitudes are defined accordingly.

4.1 Boundary Conditions

By examining previous research works (Huang and Hancock [5], Rhee [6], Bowness and Lee [7, 8], Cao et al. [9], Lie et al. [10], Chiew et al. [11]), it is found that all nodes at two ends of the chord are generally fixed in FE analysis. This type of boundary condition is reasonable as both ends of the chord are connected with adjacent members in practice. Therefore, in this study, fixed boundary conditions are used throughout in the FE analyses as shown in Figure 10.

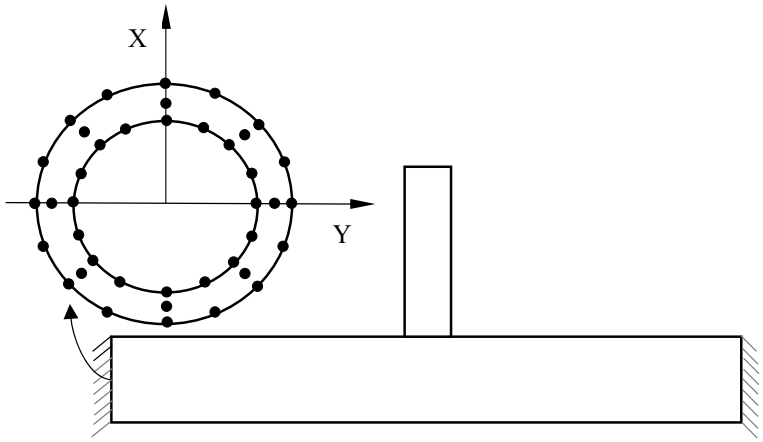

Figure 10. Boundary Conditions of Cracked CHS T/Y-joints

4.2 Applied Loading

The general form of the SIF of a cracked CHS joint can be expressed as

$$K = Y(g)\,\sigma_n\sqrt{\pi a} \tag{1}$$

where $Y(g)$ is the shape factor depending on the geometry of the CHS joint and the crack shape, σ_n is the nominal stress and a is the crack depth. For CHS joints subjected to axial loading, the nominal stress is defined as

$$\sigma_n = \frac{4P}{\left(\pi\left[d_1^2 - \left(d_1 - 2t_1\right)^2\right]\right)} \tag{2}$$

For CHS joints subjected to in-plane bending, the nominal stress is defined as

$$\sigma_n = \frac{32d_1M_i}{\left(\pi\left[d_1^4 - \left(d_1 - 2t_1\right)^4\right]\right)} \tag{3}$$

For CHS joints subjected to out-of-plane bending, the nominal stress is defined as

$$\sigma_n = \frac{32d_1M_o}{\left(\pi\left[d_1^4 - \left(d_1 - 2t_1\right)^4\right]\right)} \tag{4}$$

In this study, the nominal stress is fixed as 1 MPa for all the cracked CHS T/Y-joints. The magnitudes of the axial loading, P, in-plane bending, M_i and out-of-plane bending, M_o can be derived using Eqs. 2-4, respectively.

5. CALIBRATION OF FE MESH MODELS

The accuracy and convergence of the generated FE mesh models are verified in this section. Firstly, the SIFs of four cracked nozzles are compared with results from mesh models generated using a well-known commercial software called FEACrack™ [21]. After that, mesh convergence test is carried out. Finally, SIFs of five cracked CHS T-joints are compared with the experimental and numerical results reported by other researchers.

5.1 Comparison with FEACrack™ Mesh Model

There are very few published SIF data of cracked CHS T/Y-joints available in the literature. Most of them were published many years ago, and they were based on coarse mesh models at that time. In this sub-section, SIFs of 4 cracked nozzles generated by the new mesh generator are compared with results from FE mesh models produced by FEACrack™ [21] software. The dimensions of 4 cracked nozzles are listed in Table 2. The geometry of the nozzle is very close to the CHS T/Y-joint where the inner part of the chord at the chord-brace zone is removed. Figures 11(a), (b) and (c) compare the details of the FE mesh models generated by the new mesh generator and FEACrack™ [21] software. It can be seen that the mesh at the crack tip is three times more refined for mesh model generated by FEACrack™ [21] software, and 8 element rings are used at the crack front. For

mesh models generated by FEACrack™ [21] software, there are a total of 64160 elements and 332150 nodes; whereas for the mesh models generated by the new mesh generator, there are only 26102 elements and 119452 nodes.

Table 2. Dimensions and Surface Crack Sizes of Cracked Nozzles

Dimensions	d_0 (mm)	d_1 (mm)	t_0 (mm)	t_1 (mm)	l_0 (mm)	l_1 (mm)
	360	108	10	10	2520	800
Surface crack	1st	2nd	3rd	4th	—	—
a (mm)	2	4	6	8	—	—
$2c$ (mm)	32	64	128	256	—	—

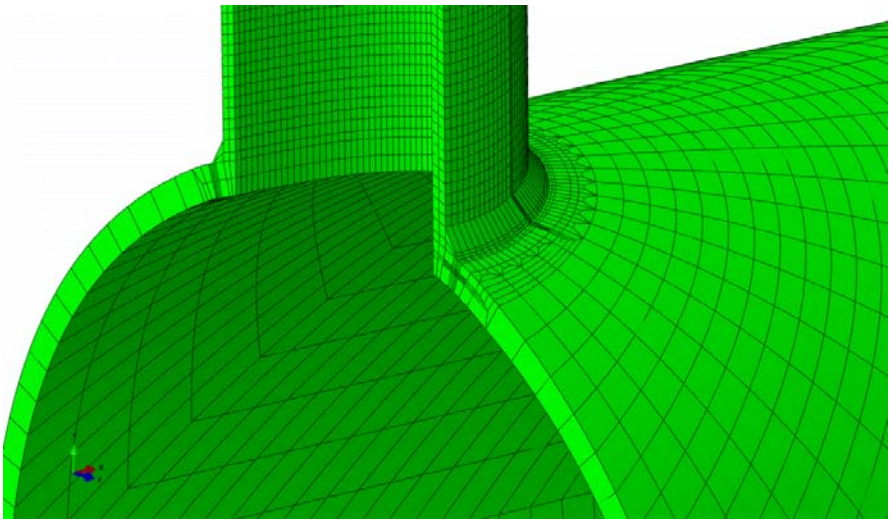

(a) A Half Mesh Model of a Cracked Nozzle Generated by FEACrack™ [21]

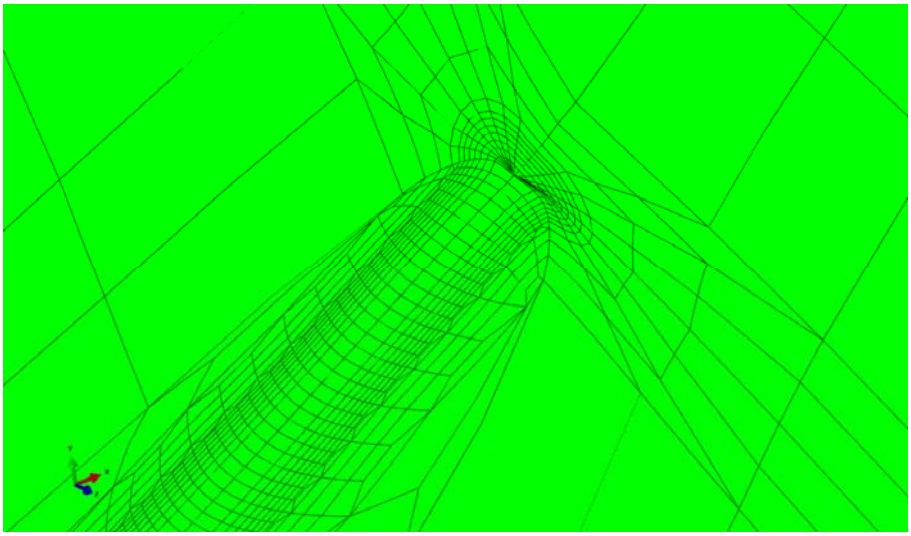

(b) Mesh Details at Crack Tips of mesh Models Generated by FEACrack™ [21]

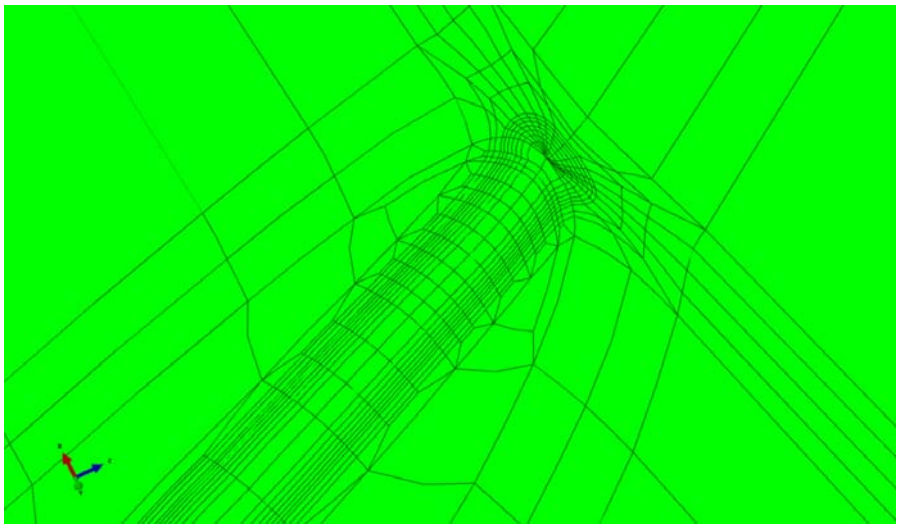

(c) Mesh Details at the Crack Tips of Mesh Models Generated by New Mesh Generator

Figure 11. Comparison of FE Mesh Models of a Cracked Nozzle Generated by FEACrack™ [21] Software and New Mesh Generator

Figures 12 compares the shape factors at the deepest point and crack ends of the four cracked nozzles subjected to axial loading and out-of-plane bending. In Figure 12, D and E denote the shape factors at the deepest point and crack ends, respectively. It can be seen that shape factors obtained from FE mesh models generated by the new mesh generator agree well with results obtained from those created by FEACrack™ [21] software. However, it is important to recognize that it does not guarantee the accuracy of the SIFs for shallower surface crack as the effect of element layers at Part A has not been investigated.

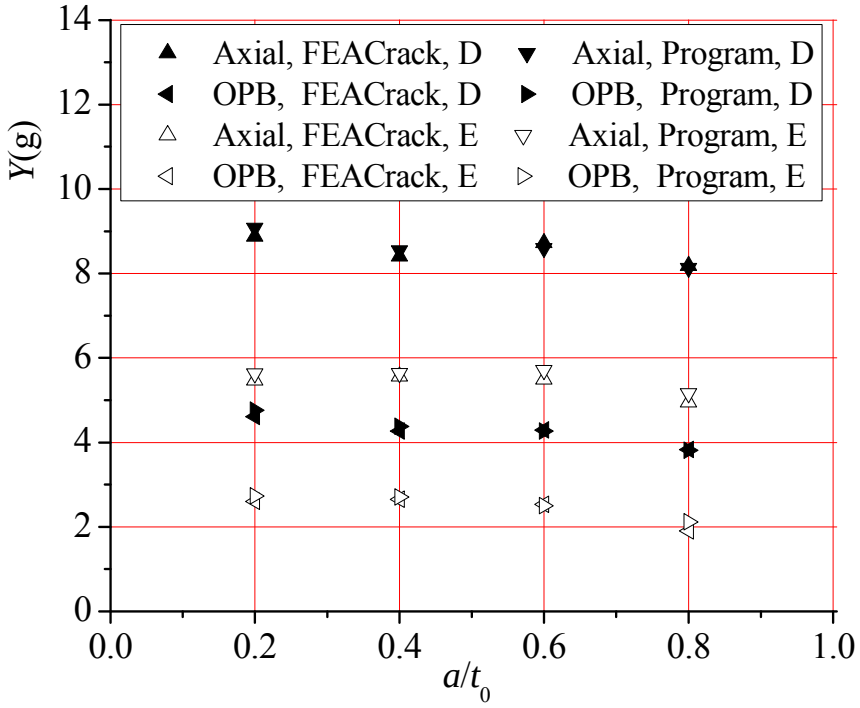

Figure 12. Comparison of Shape Factors $Y(g)$ of Cracked Nozzles

5.2 Mesh Convergence Test

In this sub-section, mesh convergence test of the FE mesh models is carried out on two aspects, which are the effect of element layers of Part A in the surface crack block and element rings enclosing the crack front. Figures 13(a) and (b) show the effect of element layers of Part A on the distribution of shape factors along the entire crack front. It is found that for cracked CHS T/Y-joints with $a/t_0 \leq 0.5$, at least 2 element layers must be designed for Part A. For cracked CHS T/Y-joints with $0.5 < a/t_0 \leq 0.8$, 1 element layer designed for Part A is sufficient to produce accurate SIFs. The definition of ϕ is illustrated in Figure 14. In this study, 3 element layers for Part A are adopted as an optimum choice for cracked CHS T/Y-joints with $a/t_0 \leq 0.5$.

Figure 15 show the effect of element rings enclosing the crack front on the distribution of the shape factors along the entire crack front. It can be seen that 3 element rings are sufficient to produce accurate shape factors at the crack tips further away from the crack ends. However, as mentioned in Refs. [21, 22], SIFs produced from the first element ring are generally not accurate and should be discarded. All SIF values are derived from the *J*-integral in ABAQUS [22] software. In order to check the path independence of the *J*-integral, 4 element rings enclosing the crack front are adopted in this study.

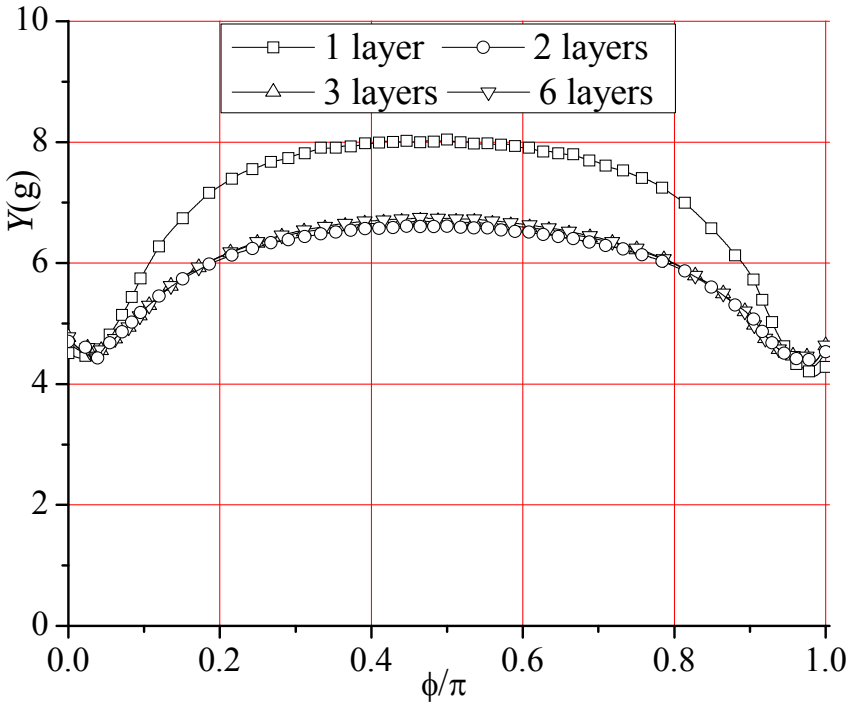

(a) α=14, β=0.5, γ=18, τ=0.6, θ=60°, a/t_0=0.2, c/a=8, Axial Loading

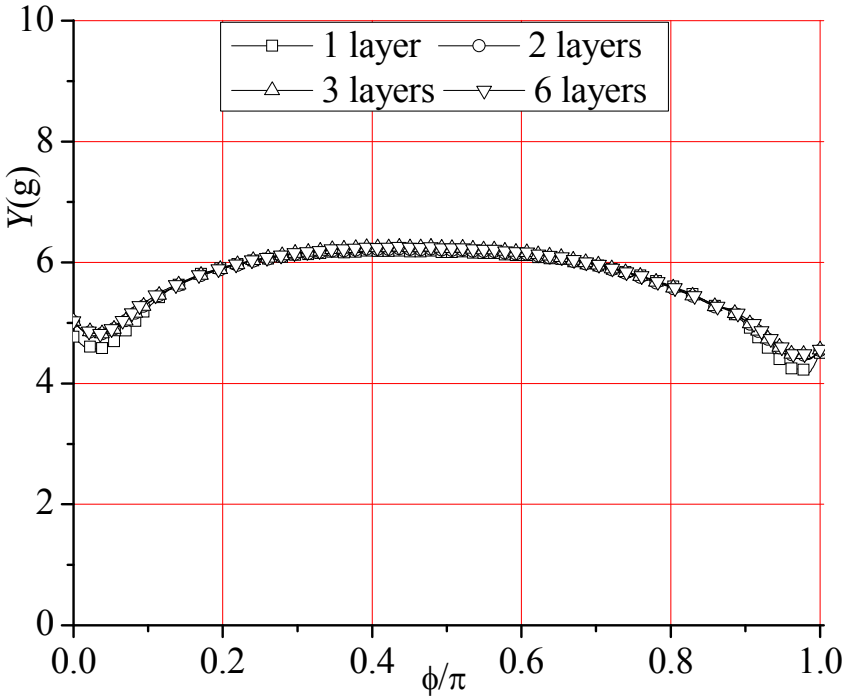

(b) α=14, β=0.5, γ=18, τ=0.6, θ=60°, a/t_0=0.5, c/a=8, Axial Loading

Figure 13. Effect of Element Layers at Part A of Surface Crack Block

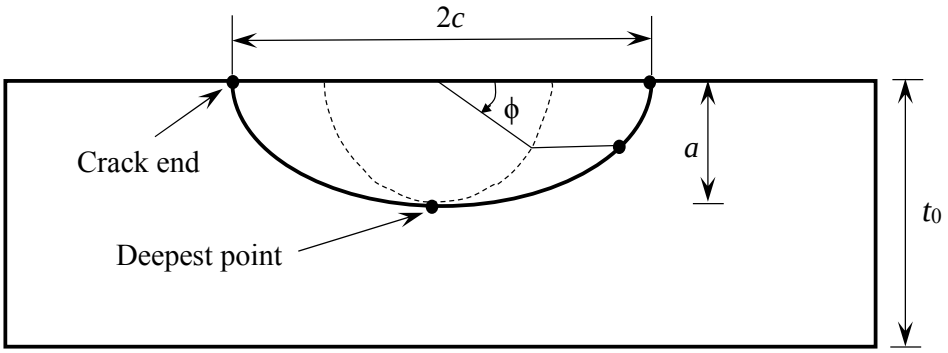

Figure 14. Definition of Crack Front Angle ϕ

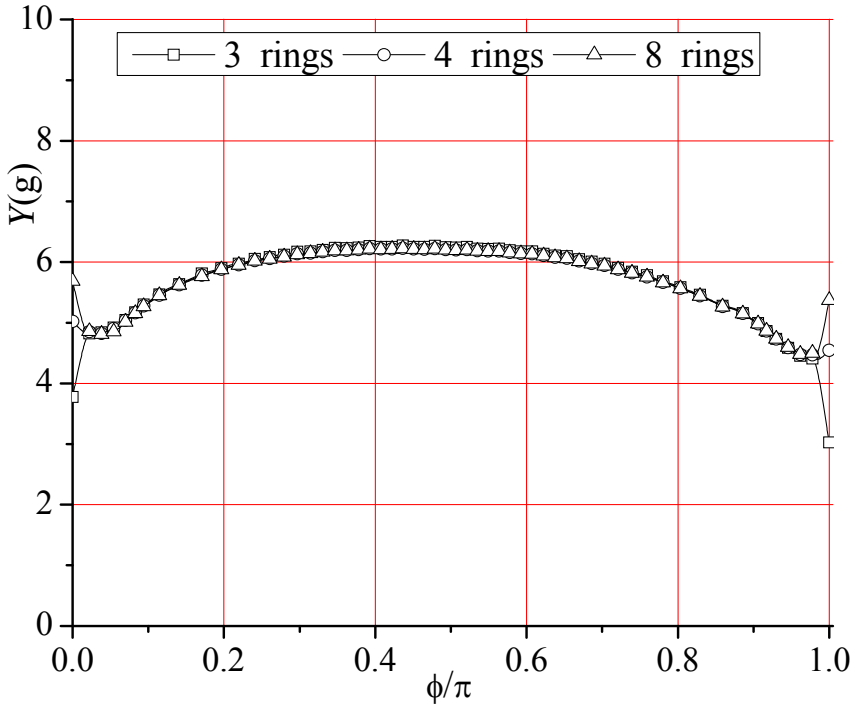

Figure 15. Effect of Element Rings Enclosing Crack Front on $Y(g)$ (α=14, β=0.5, γ=18, τ=0.6, θ=60^o, a/t_0=0.5, c/a=8, Axial Loading)

5.3 SIFs Derived from Experimental Results

The SIFs data reported by Ritchie and Hujskens [23] is widely used by researchers to validate their own FE models of cracked CHS T/Y-joints. Ritchie and Hujskens [23] carried out fatigue test on a CHS T-joint subjected to axial loading and estimated the SIFs at the deepest point located at the saddle. Table 3 lists the dimensions of the cracked CHS T-joints and the crack shapes used for calibration purposes. Figure 16 shows the comparison of the shape factors obtained in this study and results reported by other researchers (Bowness and Lee [7, 8], Ritchie and Huijskens [23], Shen and Choo [24]). It can be seen that the differences among these curves remain rather large. The difference may be caused by two facts. Firstly, the SIFs estimated from experimental test shown in Figure 16 are the average value of 5 curves reported in Ref. [23]. In fact, Ritchie and Hujskens [23] only estimated the range of the SIFs at the deepest points of 5 cracked CHS T-joints rather than provided actual SIF results. Therefore, the difference between the SIFs obtained in this study and the average SIFs shown in Figure 16 is quite acceptable as the average SIF curve does not represent the accurate one. Secondly, the FE mesh models generated by Bowness and Lee [7-8] are very coarse at that time. Therefore, their mesh models may not be dense enough to produce accurate SIF values. It can be seen that shape factors obtained by Shen and Choo [24] agree quiet well with the results obtained in this study. This is expected because FE mesh models generated by Shen and Choo [24] are created based on the cracked nozzle of FEACrack^{TM} [19] software where the mesh quality of their mesh models is very high.

Table 3. Dimensions and Surface Crack Sizes of Cracked CHS T/Y-joints

Dimensions	d_0 (mm)	d_1 (mm)	t_0 (mm)	t_1 (mm)	l_0 (mm)	l_1 (mm)
	914	457	32	16	3900	1250
Surface crack	1st	2nd	3rd	4th	5th	—
a (mm)	6.5	11.2	14.3	18.0	24.2	—
$2c$ (mm)	30.2	60.9	91.0	123.3	202.2	—

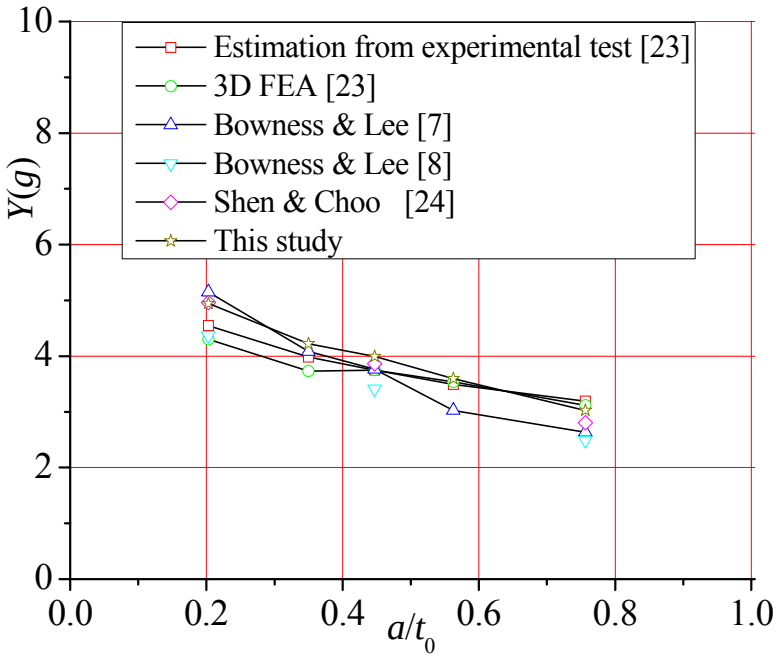

Figure 16. Comparison of the Shape Factors at Deepest Point

6. STRESS INTENSITY FACTORS OF CHS T/Y-JOINTS

A total of 246 cracked CHS T/Y-joints subjected to axial loading, in-plane bending and out-of-plane bending are analyzed, and the corresponding SIFs are calculated along the crack front. The objective of carrying such analyses is to investigate the effects of β, γ, τ, θ, a/t_0 and c/a parameters on the SIFs. Although the surface crack present in CHS T/Y-joints is a mixed mode one, K_I is still the dominant one as values of K_{II} and K_{III} are much smaller as compared to K_I [6-8]. Therefore, only K_I values are converted to shape factor $Y(g)$ and presented in this section.

6.1 Effect of Geometrical Parameters

Figures 17(a) and (b) show the effect of β on $Y(g)$. It can be seen that $Y(g)$ increases as β increases from 0.3 to 0.5. Thereafter, $Y(g)$ decreases when β is further increased to 0.8. This indicates a non-linear relationship between β and $Y(g)$. Figures 18(a) and (b) show the effect of γ on $Y(g)$ values. It can be seen that the relationship between $Y(g)$ and γ is directly proportional. Figures 19(a) and (b) show the effect of τ on $Y(g)$ values. The relationship between $Y(g)$ and τ is also almost linear. Figure 20 shows the effect of θ on $Y(g)$ values of cracked CHS T/Y-joints subjected to axial loading. As the angle θ increases from 30° to 90°, $Y(g)$ increases gradually, and the maximum value $Y(g)$ occurs in the CHS T-joint rather than at Y-joint under the same loading condition. For a particular parameter, only one type of loading case is presented. However, similar trend is also observed for the other two loading cases.

It is found that the geometrical parameters β, γ, τ, θ have the same effect on the hot spot stress of CHS T/Y-joints. For instance, the hot spot stress of CHS T/Y-joints subjected to axial loading increases as β increases from 0.3 to 0.5. Thereafter, the hot spot stress decreases when β is further increased to 0.8. It shows that SIFs of cracked CHS T/Y-joints are significantly influenced by the severity of the stress concentration at the chord-brace intersection region.

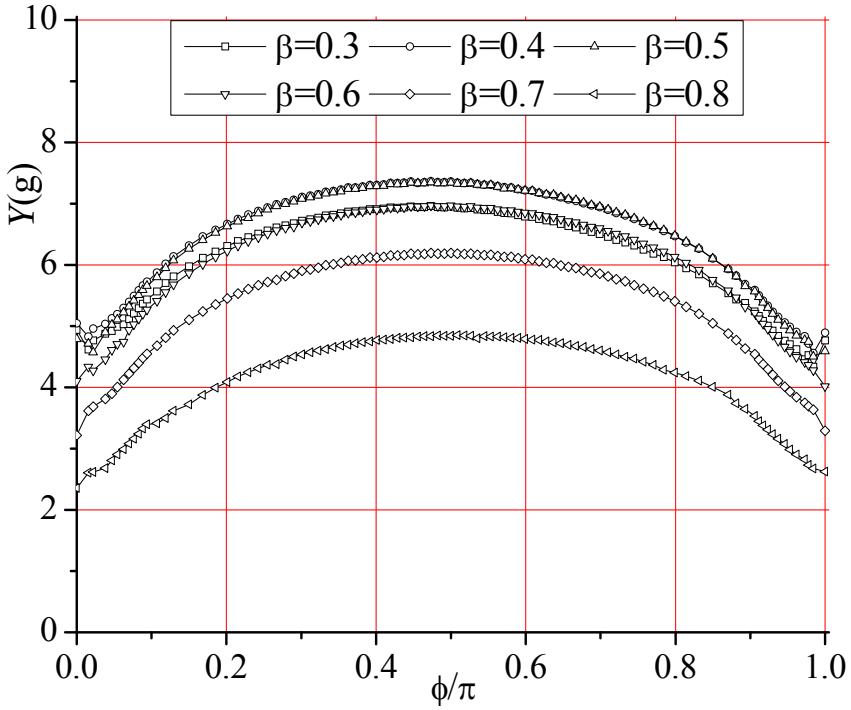

(a) α=14, γ=18, τ=0.6, θ=60°, a/t_0=0.2, c/a=8, Axial Loading

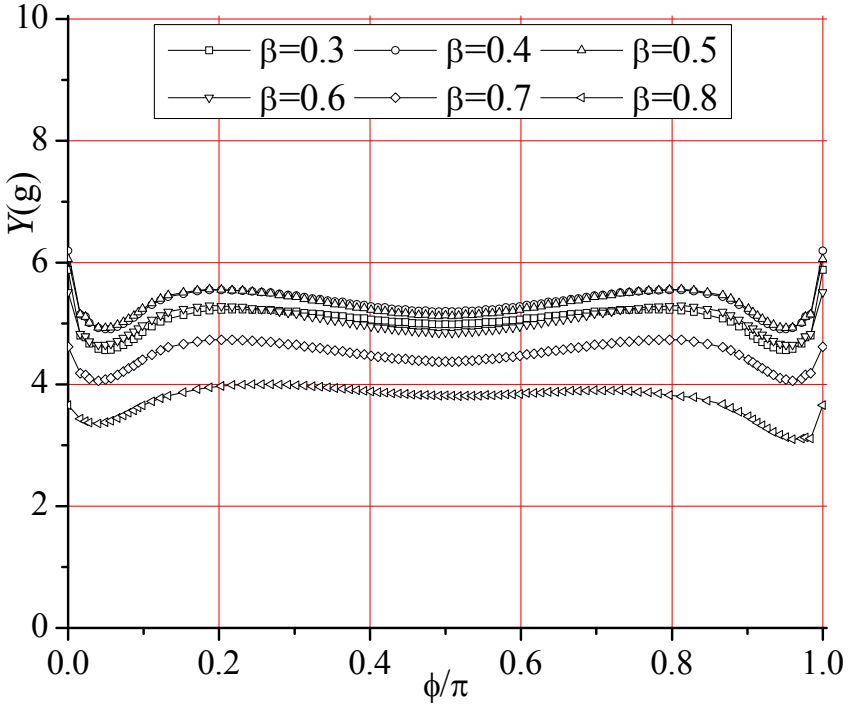

(b) α=14, γ=18, τ=0.6, θ=60°, a/t_0=0.6, c/a=6, Axial Loading

Figure 17. Effect of β on K_I of Cracked CHS T/Y-joints

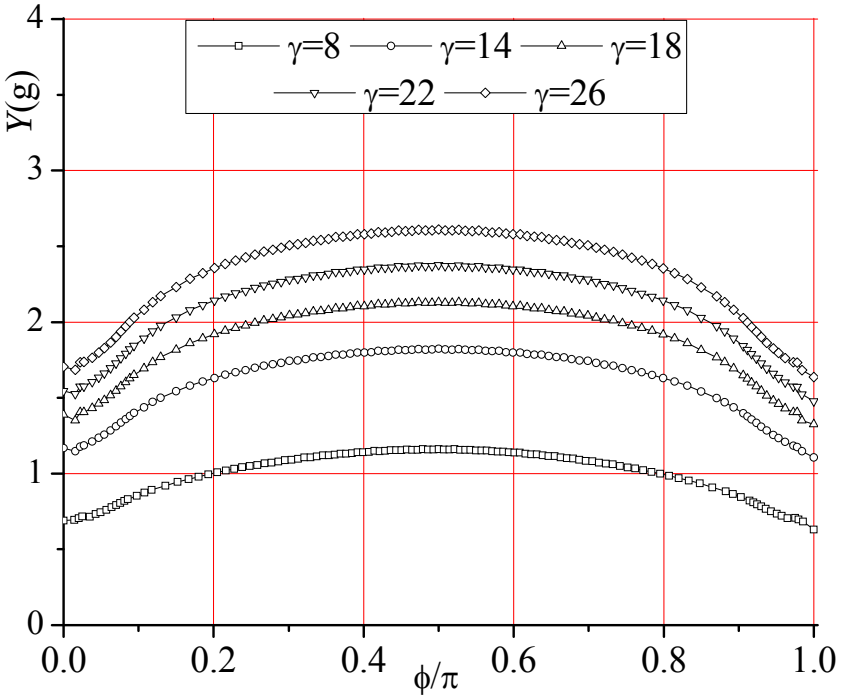

(a) α=14, β=0.5, τ=0.6, θ=60°, a/t_0=0.2, c/a=8, In-plane Bending

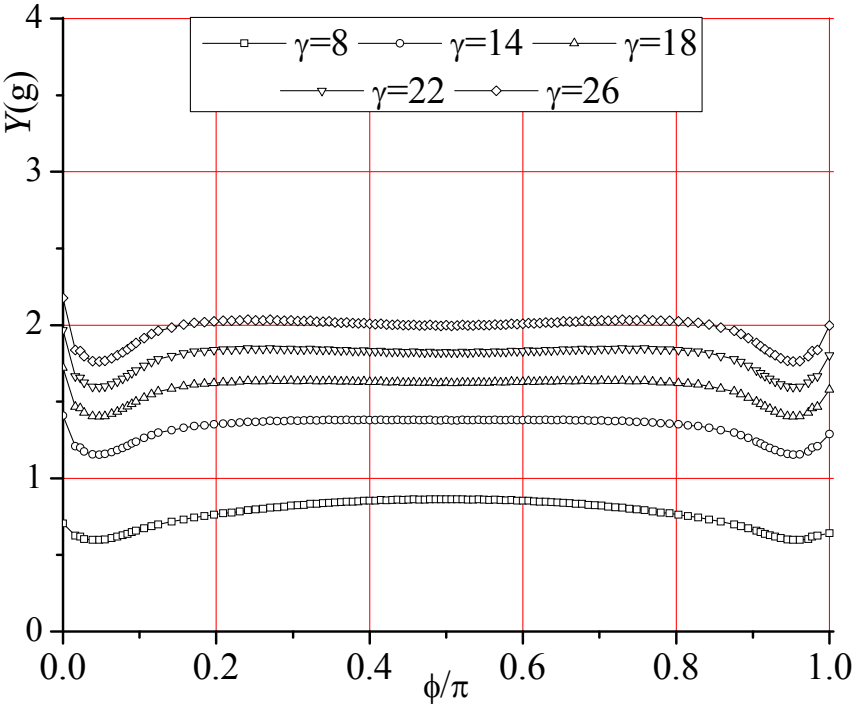

(b) α=14, β=0.5, τ=0.6, θ=60°, a/t_0=0.6, c/a=6, In-plane Bending

Figure 18. Effect of γ on K_I of Cracked CHS T/Y-joints

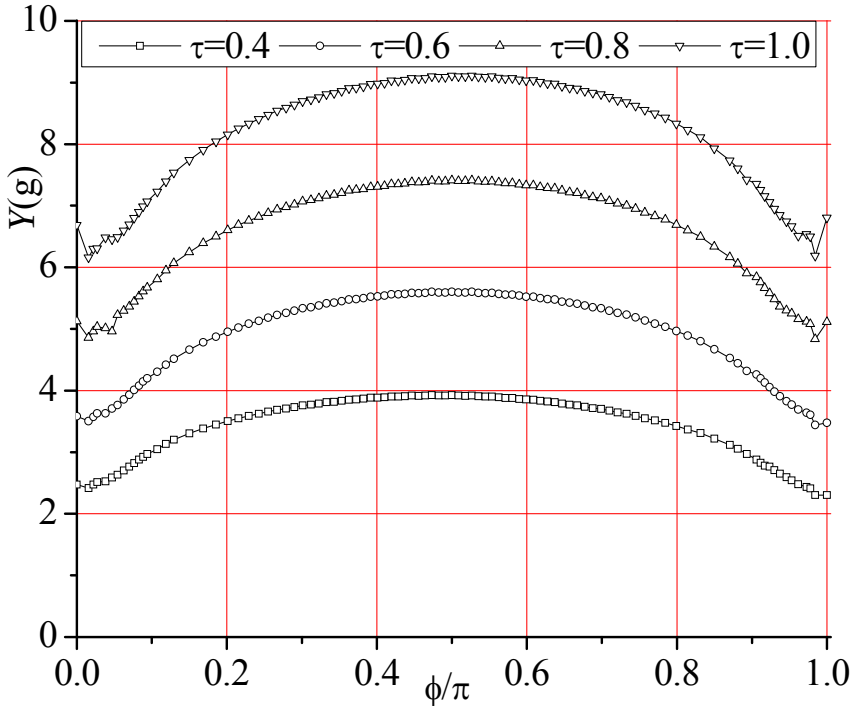

(a) α=14, β=0.5, γ=18, θ=60º, a/t_0=0.2, c/a=10, Out-of-plane Bending

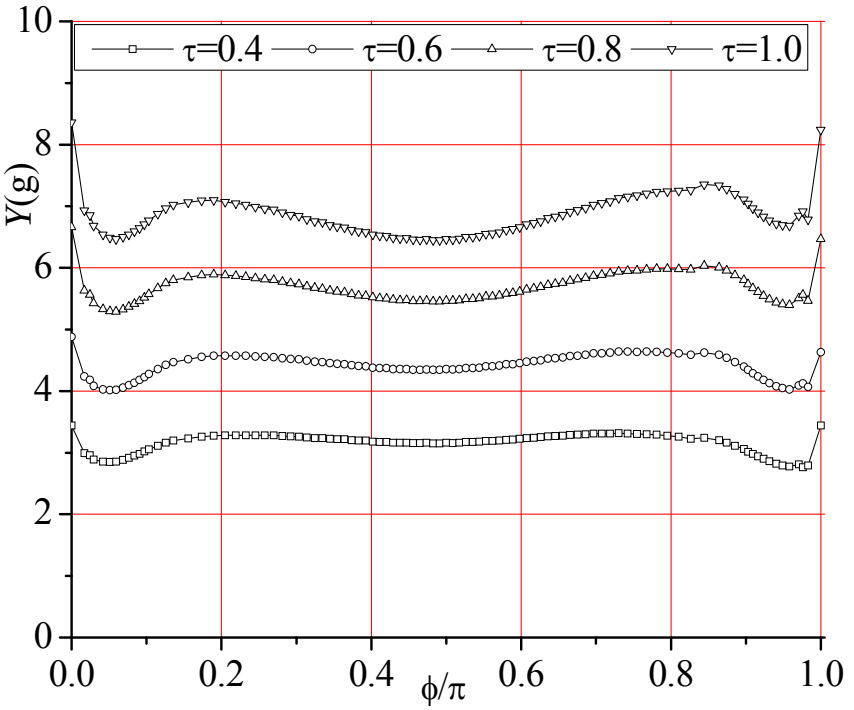

(b) α=14, β=0.5, γ=18, θ=60º, a/t_0=0.6, c/a=6, Out-of-plane Bending

Figure 19. Effect of τ on K_I of Cracked CHS T/Y-joints

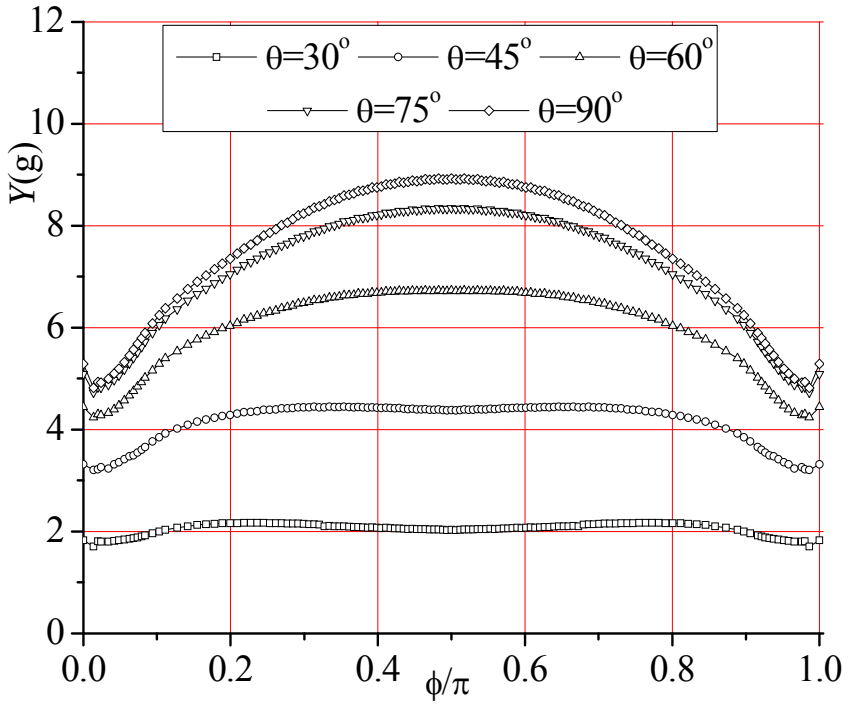

Figure 20. Effect of θ on K_I of Cracked CHS T/Y-joints subjected to Axial Loading (α=14, β=0.5, γ=18, τ=0.6, a/t_0=0.6, c/a=10)

6.2 Effect of Crack Shapes

Figures 21(a) and (b) show the effect of crack depth a/t_0 on $Y(g)$ values for CHS T/Y-joints subjected to axial loading. It can be seen that the distributions of $Y(g)$ values are completely different for a crack located at the saddle or at the crown. When the crack is located at the saddle, $Y(g)$ at the deepest point increases gradually as the crack depth increases, and after the maximum value is reached, it decreases even if the crack depth increases further. For a cracked CHS T/Y-joint with a crack located at the crown, the distributions of $Y(g)$ values increase as the crack depth increases at the deepest point. A similar finding is observed for cracked CHS T/Y-joints subjected to in-plane bending and out-of-plane bending cases.

Figure 22 shows the effect of the crack length c/a on $Y(g)$ values for CHS T/Y-joints subjected to axial loading. It can be seen that the distributions of $Y(g)$ values are the same for a crack located at the saddle or at the crown. The peak value of $Y(g)$ along the surface crack front tends to shift from the crack ends to the deepest point as the crack length increases. This is particularly true for a CHS T/Y-joint containing a surface crack located at the saddle. Moreover, there exists a non-linear relationship between $Y(g)$ and c/a. A similar finding is observed for cracked CHS T/Y-joints subjected to in-plane bending and out-of-plane bending cases.

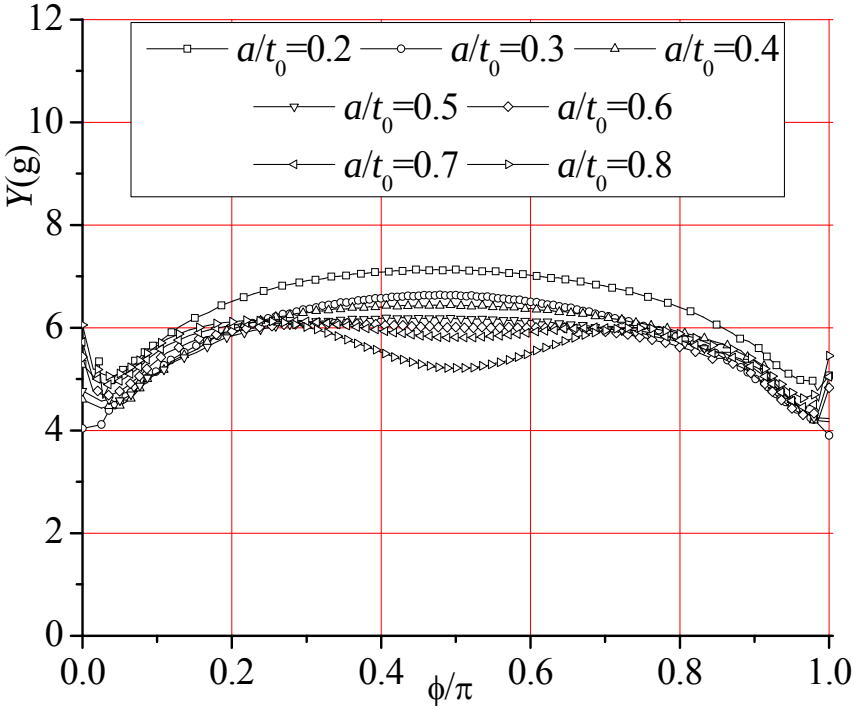

(a) α=14, β=0.5, γ=18, τ=0.6, θ=60°, *c*/*a*=8, Crack at the Saddle

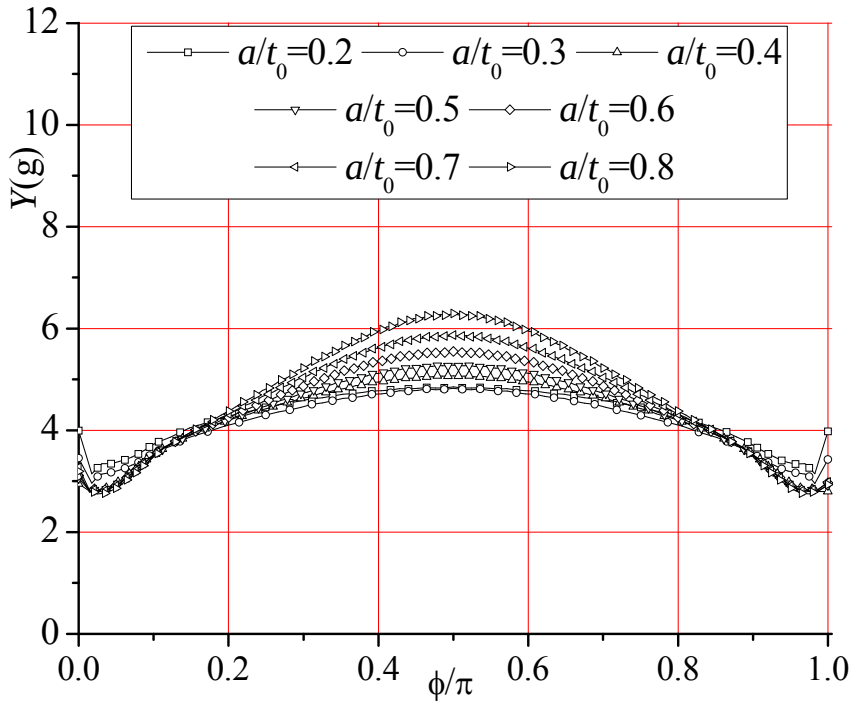

(b) α=14, β=0.5, γ=8, τ=0.6, θ=60°, *c*/*a*=8, Crack at the Crown

Figure 21. Effect of a/t_0 on K_I of Cracked CHS T/Y-joints Subjected to Axial Loading

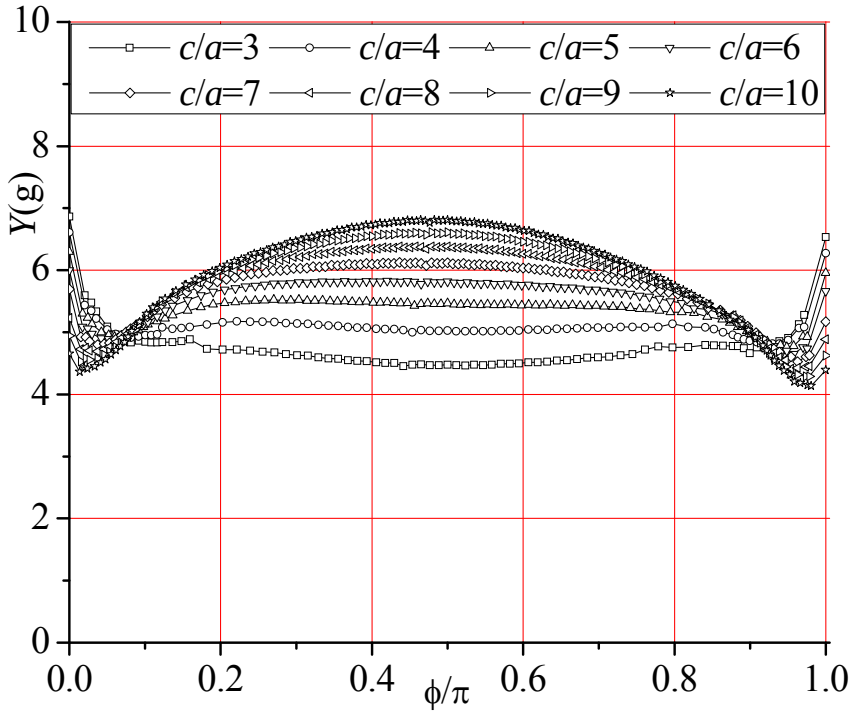

Figure 22. Effect of c/a on K_I of Cracked CHS T/Y-joints Subjected to Axial Loading (α=14, β=0.5, γ=18, τ=0.6, θ=60°, a/t_0=0.4)

7. ESTIMATION OF SIFS USING BS7910 (2005) INDIRECT METHOD

The indirect method used to estimate the SIF of a cracked CHS T/Y-join is expressed as

$$K \approx (M_{km} M_m \text{SCF} \times (1 - \text{DOB}) + M_{kb} M_b \text{SCF} \times \text{DOB})\, \sigma_n \sqrt{\pi a} \tag{5}$$

where a is the crack depth, M_{km} and M_{kb} are the weld toe magnification factors, and M_m *and* M_b are the plain plate shape factors. The subscripts *m* and *b* denote membrane and bending load respectively. SCF is the stress concentration factor and DOB is the degree of bending at the would-be location of the crack. σ_n is the nominal stress in the reference brace of the joint. As DOB, SCF and σ_n are all obtained from uncracked CHS joints, and M_{kj}, M_j (j=m, b) can be calculated from parametric equations, it is clear that Eq. 5 is a very convenient approach for estimating the SIFs of any cracked CHS joint because it avoids the complexity of generating the mesh models of the surface crack.

In this section, the degree of bending (DOB) [25] recommended in BS7910 [14] is adopted, whereas SCF equations for CHS T/Y-joints subjected to three basic loading incorporated in API-RP-2A [19] are used. Equations of M_{kj} and M_j (j=m, b) can be found in BS7910 [14]. Figures 23 to 25 show the differences of shape factors at the deepest point for all the loading cases. The percentage differences are found ranging from -36.9% to 77.6% for axial loading; 13.1% to 68.9% for in-plane bending; and -32.9% to 37.9% for out-of-plane bending cases. It can be seen that the indirect method underestimates the SIFs of a crack located at the crown and at the saddle for the axial loading and out-of-plane bending, respectively. Hence, Eq. 5 should be used with caution.

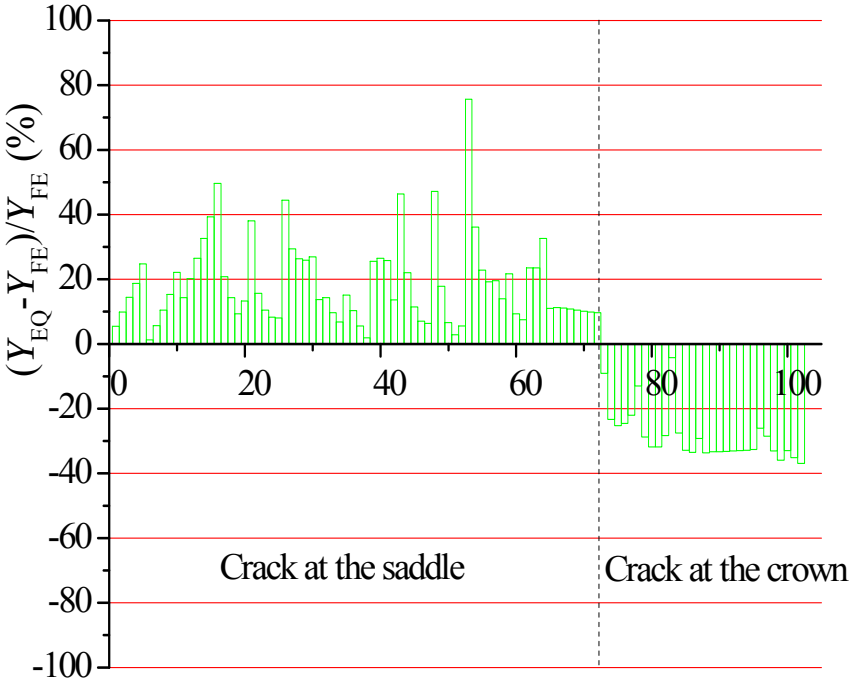

Figure 23. Comparison of Shape Factors of Cracked CHS T/Y-joints Subjected to Axial Loading

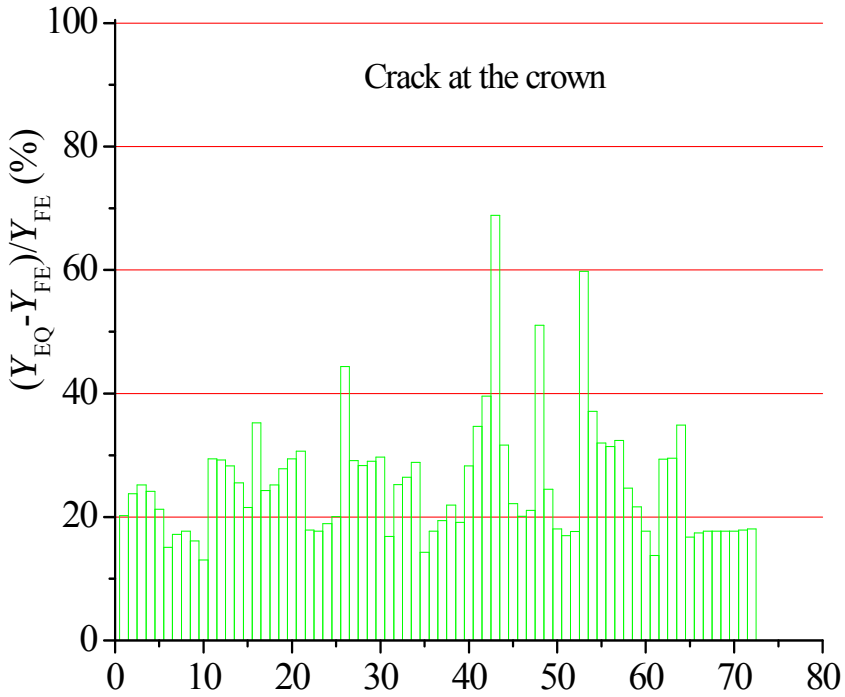

Figure 24. Comparison of Shape Factors of Cracked CHS T/Y-joints Subjected to In-plane Bending

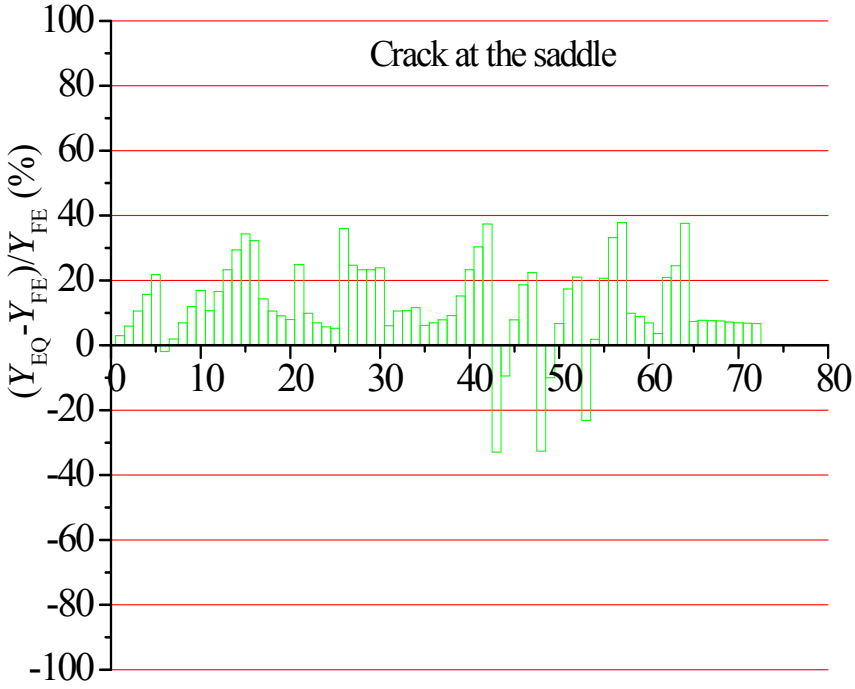

Figure 25. Comparison of Shape Factors of Cracked CHS T/Y-joints Subjected to Out-of-plane Bending

8. CONCLUSIONS

In this study, a new mesh generator is developed to produce high quality FE mesh models of cracked CHS T/Y-joints containing a surface crack. Extensive tests are carried out to calibrate the accuracy and convergence of the designed FE mesh models. It is found that number of element rings enclosing the crack front has a minor impact on the SIFs at crack tips further away from two crack ends. In order to check the path independence of *J*-integral, 4 element rings enclosing the crack front is found to be an optimum choice. For cracked CHS T/Y-joints containing shallow surface crack, element size in the remaining part ahead of the Crack Tube has a significant effect on SIFs and it should be sufficiently fine. A novel mesh refinement scheme is developed to increase element layers in the region ahead of the Crack Tube so as to optimize the transition mesh in this region. It is found that 3 element layers in the remaining part ahead of the Crack Tube are sufficient to produce accurate SIFs for the cracked CHS T/Y-joints.

The new mesh generator is then used to calculate the SIFs of 246 cracked CHS T/Y-joints subjected to axial loading, in-plane bending and out-of-plane bending. The SIFs at the deepest points are also estimated using the indirect method incorporated in BS7910 [14]. It is found that it does not always produce conservative results. For the axial loading, the percentage difference of the SIFs ranges from 1.3% to 77.6% for crack located at the saddle; and -27.5% to -36.9% for crack located at the crown. Therefore, the indirect method has consistently underestimated the SIFs when the crack is located at the crown location. This may due to the fact that parameters used in the indirect method such as the SCF and the DOB obtained are based on FE models where the hot spot stress is always located at the saddle position. For the in-plane bending and out-of-plane bending cases, the percentage difference of the SIFs ranges from 13.1% to 68.9% and -32.9% to 37.9% respectively. Hence, the indirect method should be used with caution as it is not always conservative for every case.

NOMENCLATURES

a	crack depth
c	half crack length
DOB	degree of bending
d_0	chord diameter
d_1	brace diameter
H_{cra}	height of cutting cross-section of the Crack Tube
K	general form of stress intensity factor
K_I	Mode-I stress intensity factor
K_{II}	Mode-II stress intensity factor
K_{III}	Mode-III stress intensity factor
l_0	chord length
l_1	brace length
M_{km}, M_{kb}	weld toe magnification factors due to membrane and bending stresses
M_m, M_b	plain plate shape factor for tension and bending
SCF	stress concentration factor
t_0	thickness of the chord of nozzle and CHS T/Y-joint
t_1	thickness of the brace of nozzle and CHS T/Y-joint
W_{cra}	width of cutting cross-section of the Crack Tube
Y_{EQ}	shape factor calculated from Eq. 5
Y_{FE}	shape factor determined from FE analysis
$Y(g)$	general form of shape factor
α	a ratio of $2l_0/d_0$
β	a ratio of d_1/d_0
γ	a ratio of $d_0/2t_0$
θ	intersecting angle between brace and chord
σ_n	nominal stress
τ	a ratio of t_1/t_0
ϕ	crack front angle

REFERENCES

[1] Shivakumar, K.N. and Raju, I.S., "Treatment of Singularities in Cracked Bodies," International Journal of Fracture, 1990, Vol. 45, No. 3, pp. 159-178.

[2] Madia, M., Beretta, S., Schödel, M., Zerbst, U., Luke, M. and Varfolomeev, I., "Stress Intensity Factor Solutions for Cracks in Railway Axles," Engineering Fracture Mechanics, 2011, Vol. 78, No. pp. 764-792.

[3] Hutař, P. and Náhlík, L., "Fatigue Crack Shape Prediction Based on Vertex Singularity," Applied and Computational Mechanics, 2008, Vol. 2, No. pp. 45-52.

[4] Heyder, M., Kolk, K. and Kuhn, G., "Numerical and Experimental Investigations of the Influence of Corner Singularities on 3D Fatigue Crack Propagation," Engineering Fracture Mechanics, 2005, Vol. 72, No. 13, pp. 2095-2105.

[5] Huang, X. and Hancock, J.W., "The Stress Intensity Factors for Semi-elliptical Cracks in a Tubular Welded T-joint Under Axial Loading," Engineering Fracture Mechanics, 1988, Vol. 30, No. 1, pp. 25-35.

[6] Rhee, H.C., "Fatigue Crack Growth Analyses of Offshore Structural Tubular Joints," Engineering Fracture Mechanics, 1989, Vol. 34, No. 5/6, pp. 1231-1239.

[7] Bowness, D. and Lee, M.M.K., "The Development of an Accurate Model for the Fatigue Assessment of Doubly Curved Cracks in Tubular Joints," International Journal of Fracture, 1995, Vol. 73, No. 2, pp. 129-147.
[8] Bowness, D. and Lee, M.M.K., "Fatigue Crack Curvature under the Weld Toe in an Offshore Tubular Joint," International Journal of Fatigue, 1998, Vol. 20, No. 6, pp. 481-490.
[9] Cao, J.J., Yang, G.J., Packer, J.A. and Burdekin, F.M., "Crack Modeling in FE Analysis of Circular Tubular Joints," Engineering Fracture Mechanics, 1998, Vol. 61, No. 5-6, pp. 537-553.
[10] Lie, S.T., Lee, C.K. and Wong, S.M., "Model and Mesh Generation of Cracked Tubular Y-Joints," Engineering Fracture Mechanics, 2003, Vol. 70, No. 2, pp. 161-184.
[11] Chiew, S.P., Lie, S.T., Lee, C.K. and Huang, Z.W., "Stress Intensity Factors for a Surface Crack in a Tubular T-Joint," International Journal of Pressure Vessels and Pipes, 2001, Vol. 78, No. 10, pp. 677-685.
[12] Peter, T.M., Corrosion Fatigue and Fracture Mechanics of High Strength Jack Up Steels, PhD thesis, Department of Mechanical Engineering, University College London, UK, 1998.
[13] Shao, Y.B. and Lie, S.T., "Parametric Equation of Stress Intensity Factor for Tubular K-joint," International Journal of Fatigue, 2005, Vol. 27, No. 6, pp. 666-679.
[14] BS7910-Amendment 1, Guide to Methods for Assessing the Acceptability of Flaws in Fusion Welded Structures, British Standards Institution, London, UK, 2005.
[15] Newman, J.C. and Raju, I.S., "An Empirical Stress Intensity Factors Equation for the Surface Crack," Engineering Fracture Mechanics, 1981, Vol. 15, No. 1-2, pp. 185-192.
[16] Newman, J.C., Reuter, W.G. and Aveline, C.R., "Stress and Fracture Analysis of Semi-elliptical Surface Cracks," 30th National Symposium of Fatigue and Fracture Mechanics, St. Louis, MO, USA, 1998, pp. 403-426.
[17] Lee, M.M.K. and Bowness, D., "Estimation of Stress Intensity Factor Solutions for Weld Toe Cracks in Offshore Tubular Joints," International Journal of Fatigue, 2002, Vol. 24, No. 8, pp. 861-875.
[18] Lie, S.T., Li, T. and Shao, Y.B., "Estimation of Stress Intensity Factors in Tubular K-joints Using Direct and Indirect Methods". International Journal of Advanced Steel Construction, 2012, Vol. 8, No. 2, pp. 17-37.
[19] America Petroleum Institute, Recommended Practice for Planning, Designing and Constructing Fixed Offshore Platforms-Working Stress Design, API-RP-2A-WSD, Washington, USA, 2005.
[20] Lie, S.T., Li, T. and Shao, Y.B., "Plastic Collapse Load Prediction and Failure Assessment Diagram Analysis of Cracked Circular Hollow Section T-joint and Y-joint," Fatigue & Fracture of Engineering Material & Structure, 2014, Vol. 37, No. 3, pp. 314-324.
[21] FEACrack™, User's Manual, Version 3.2, Quest-reliability-LLC, USA, 2003.
[22] ABAQUS, (2009). Standard User's Manual, Version 6.9. Hibbett, Karlsson & Sorensen, Inc. Providence, Rhode Island, USA.
[23] Ritchie, D., and Huijskens, H.A.M., "Fracture Mechanics Based Prediction of the Effect of Size of Tubular Joint Test Specimens on Their Fatigue Life," The 8th International Conference on Offshore Mechanics and Arctic Engineering, The Hague, Netherlands, 1988, pp. 121-126.
[24] Shen, W. and Choo, Y.S., "Stress Intensity Factor for a Tubular T-joint with Grouted Chord," Engineering Structures, 2012, Vol. 35, pp. 37-47.
[25] Connolly, M.P., Hellier, A.K., Dover, W.D. and Sutomo, J., "A Parametric Study of the Ratio of Bending to Membrane Stress in Tubular Y and T joints," International Journal of Fatigue, 1990, Vol. 12, No. 1, pp. 3-11.

OPTIMUM POSITION OF STEEL OUTRIGGER SYSTEM FOR HIGH RISE COMPOSITE BUILDINGS SUBJECTED TO WIND LOADS

Sabrina Fawzia[1,*] and Tabassum Fatima[2]

[1, 2] *Science and Engineering Faculty, School of Civil Engineering and Built Environment, Queensland University of Technology, Brisbane 4000, Queensland, Australia*
**(Corresponding author: E-mail: sabrina.fawzia@qut.edu.au)*

Received: 16 January 2015; Revised: 17 June 2015; Accepted: 3 July 2015

ABSTRACT: The responses of composite buildings under wind loads clearly become more critical as the building becomes taller, less stiff and more lightweight. When the composite building increases in height, the stiffness of the structure becomes more important factor and introduction to belt truss and outrigger system is often used to provide sufficient lateral stiffness to the structure. Most of the research works to date is limited to reinforced concrete building with outrigger system of concrete structure, simple building plan layout, single height of a building, one direction wind and single level of outrigger arrangement. There is a scarcity in research works about the effective position of outrigger level on composite buildings under lateral wind loadings when the building plan layout, height and outrigger arrangement are varied. The aim of this paper is to determine the optimum location of steel belt and outrigger systems by using different arrangement of single and double level outrigger for different size, shape and height of composite building. In this study a comprehensive finite element modelling of composite building prototypes is carried out, with three different layouts (Rectangular, Octagonal and L shaped) and for three different storey (28, 42 and 57-storey). Models are analysed for dynamic cyclonic wind loads with various combination of steel belt and outrigger bracings. It is concluded that the effectiveness of the single and double level steel belt and outrigger bracing are varied based on their positions for different size, shape and height of composite building.

Keywords: Steel structure, Lateral deflection, Outriggers, Composite building, Multi-storey, Wind load

DOI: 10.18057/IJASC.2016.12.2.4

1. INTRODUCTION

Tall composite building constructions have been rapidly increasing worldwide because of their lightweight and speed of construction. The design of tall structure is usually governed by the lateral loads imposed on the structure. As building gets taller, the structural engineers have been increasingly challenged to achieve structural safety under lateral wind load. The belt and outrigger bracings are commonly used for wind dominated area as one of the structural systems to determine structural safety due to lateral wind load.

Outriggers have been used for approximately four decades although their existence as a structural member has a much longer history. Academic research has limited amount of material on overall performance of composite buildings with steel bracings, however; appreciable amount of literature is present on reinforced concrete, steel structures and very limited on composite structures such as; Nanduri et al [1] used 30 story reinforced concrete building to study the behavior of outrigger, outrigger location optimization and the efficiency of each outrigger when three outriggers are used in the structure. For 30-storey model, the optimum location of the outrigger system is proven to be at the middle height of the structure from the base.

Chung 2010 [2] used reinforced concrete construction with two outrigger-braced core-to-columns building model with height of 300m and 36m x 36m horizontal floor dimensions. His work

principally provided a preliminary guide to assess the performance of outrigger braced system by estimating the restraining moments at the outrigger locations, core base bending moment, the total building deflection, along-wind and crosswind acceleration of a tall building. His study shows that the best location of the outriggers is somewhere at equal distance of the height of the structure from the base.

Kian and Siahaan [3] extrapolated the efficiency of belt-truss and outriggers in concrete high-rise buildings subjected to wind and earthquake loadings. Authors used two dimensional 40- storey model for wind and three dimensional 60-storey model for seismic load analysis. They came up with the optimum location of belt-truss and outriggers with 65% and 18% lateral deflection reduction for wind and earthquake loadings respectively.

Hoenderkamp and Bakker [4] presented a graphical method of analysis for tall building frame braced with outriggers and subjected to uniform lateral loadings. Authors have used steel structures for their two dimensional model. They have concluded that behaviour of steel braced frame with outriggers was similar to concrete wall with outriggers beams and further suggested that horizontal deflection and bending moments were influenced by stiffness and therefore; it should be included in the preliminary design of tall structures.

Hoenderkamp [5] derived an analytical method for preliminary design of outrigger braced high-rise shear walls subjected to horizontal loading. He used a two dimensional analytical model of shear wall with outriggers at two levels, one outrigger has a fixed location up the height of the structure, while the second was placed at various location along the model height. He has provided comparison of deflection reduction for a 29-storey model with few combination of two outriggers floors and concluded that the optimum location of the second outrigger was at 0·577 of the height of the building when the first one was placed at the top of the building.

Lee et al [6] focused on deriving the equations for wall-frame structures with outriggers under lateral loads in which the whole structure was idealized as a shear-flexural cantilever and effects of shear deformation of the shear wall and flexural deformation of the frame were considered. Authors have verified the equation by considering the concrete wall-frame building structure under uniform wind loading. Conclusions highlighted that consideration of shear deformations of walls and flexural deformations of frame in analytical formula gave sufficiently accurate results.

Lee et al [7] used wall frame tall building for octagonal plan building in their study. Authors developed simplified model to calculate average stiffness and determined the global behaviour of the buildings.

Taranath [8, 9] documented different composite systems, different varieties of composite building and different varieties of lateral reistance system available in the world for composite building.

Rahgozar and Sharifi [10] presented mathematical model for calculation of stresses in columns of combined framed tube, shear core and belt-truss system. He applied his mathematical models to 30, 40 and 50 storey buildings and compared the results with SAP 2000 software for its applicability. He concluded with the best outrigger location at 1/4th and 1/6th of the model height. His study was based on pure numerical models and he did not use the actual properties of materials.

In today's tall building engineering, it is a rare event indeed, to come across a building that is regular in plan [8]. Structural engineers are more interested for varieties of plan layout for tall composite building. Moreover it is not difficult to adopt an analytical model based on literature [4, 5 and 6] to obtain the drift and the natural frequencies of the buildings with less efforts for 98 m

height but it is not wise to use available analytical model when building height gets bigger. All of the above researches do not consider a comprehensive study of composite building of dissimilar plan layouts of varied heights with different combinations of belt-truss and outriggers under wind dominated area. Different combination of lateral load resisting system i.e. single floor or double floor bracings, with varied plan layouts and assorted heights would results differently.

Therefore; the aim of this paper is to study the behaviour of multi-storey composite buildings when subjected to cyclonic wind loads, calculated in Australian standards domain. Conclusion will be determined by using frequency and deflection results. The assumption of this study is frequency level considered below 1 Hz. As the study is purely based under wind load authors ignored the effects from vibration and damping. P-D effect which should be unimportant in serviceability limit state also ignored in this study.

A detailed parametric study has been carried out by varying heights (98m, 147m and 199.5m), plans (Rectangular, Octagonal and L-shaped) and number and placement of lateral bracings for commonly used composite building structures in Australia.

2. PARAMETERS OF STUDY

The choice of parameters integrated many factors based on aim and objectives of this paper. These include using of locally available construction material, commonly occurring building types and consideration of local general practices. Hence following parameters are selected for this study;

- Model heights;
- Model plan layout;
- Belt-truss and outriggers variations.

2.1 Models Heights Selection

The following building heights are selected based on the below considerations:

- The maximum allowable height for the applicability of Australian Standards AS1170.2 [11] is 200 m. Therefore; 57-storey (199.5 m with 3.5 m floor to floor height) is chosen to study the effects of wind and seismic loads on maximum given building elevation.
- 42-storey (147.0 m) is most common type of multi-storey rise within the Australian urban environment. Many office and residential buildings are constructed around this height; hence this is an appropriate comparison with the 199.5 m tall model.
- 28-storey is nearly half the height of the 57 storey model, i.e. 98 m and is selected to establish a comparison and to find out the benefits (if any) of belt-truss and outriggers on such a low elevation.

2.2 Layout Selection for Models

The main object in layout selection is to allow maximum variation and maintain distinction. In all models, Z-axis represents the vertical axis, whereas; X-axis and Y-axis are planner axes. The plan layouts selected are;

2.2.1 Rectangular shaped

Rectangular model with plan dimensions of 30 m and 80 m (Figure 1 & Figure 2) is a common shape in Australia because land demarcation is usually rectangular in most of the local municipalities; therefore developers tend to go for this shape of structure. The layout has higher rigidity in one axis

and less in the other; hence it is relevant to study the lateral load effects and frequency modes of this plan layout.

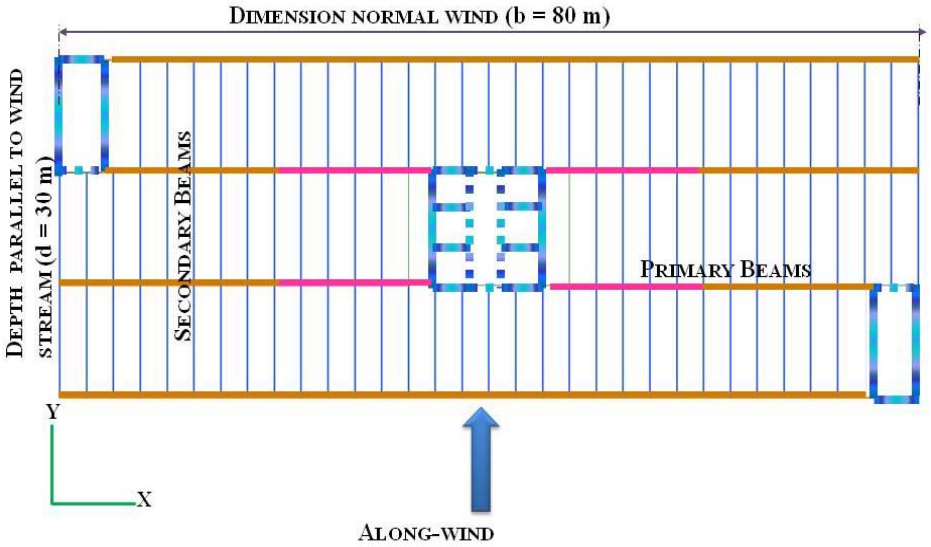

Figure 1. Direction of Wind Rectangular Plan

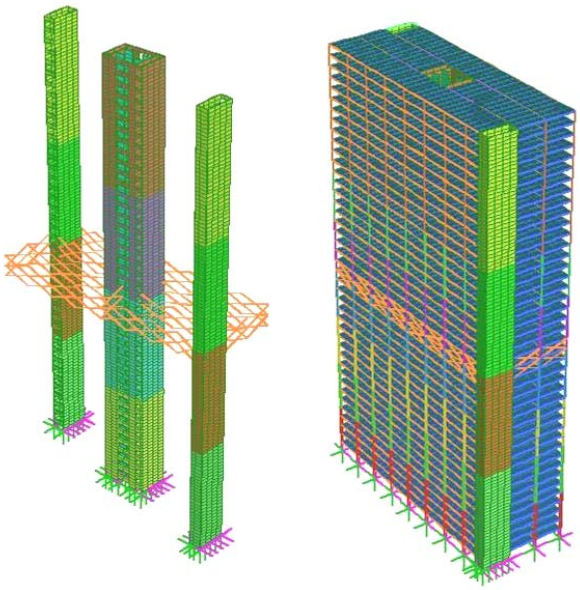

Figure 2. Rectangular Model Elevation (Shear Wall and Full Model)

2.2.2 Octagonal shape

This has equal plane dimensions of 60 m in each direction (Figure 3 and Figure 4) and hence can represent circular and square buildings. However; in square shapes swirling effects can be produced by re-entrant corners. Australian standard AS1170.2 [11] takes account of these effects unless building exceeds the prescribed height and width. This layout is also popular for office building.

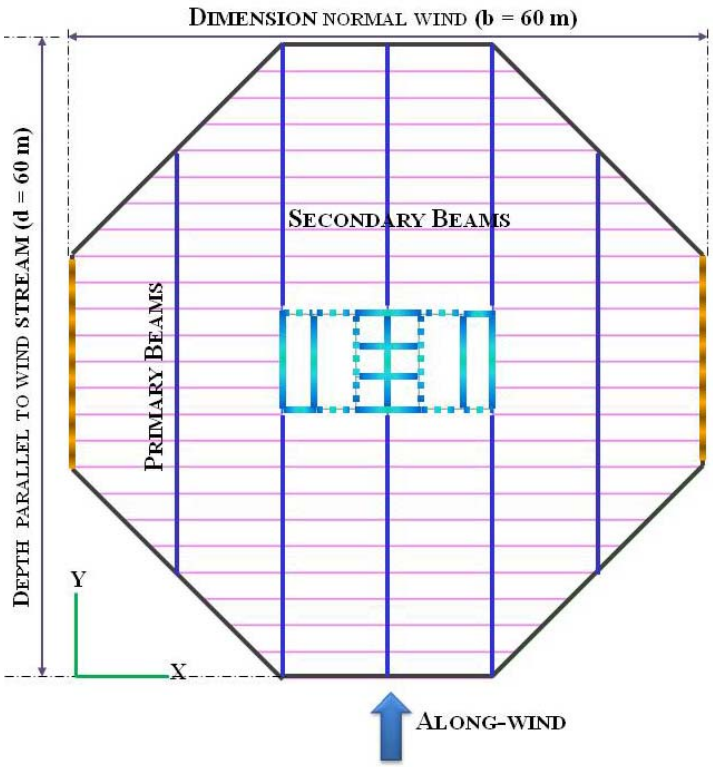

Figure 3. Direction of Wind on Octagonal Layout

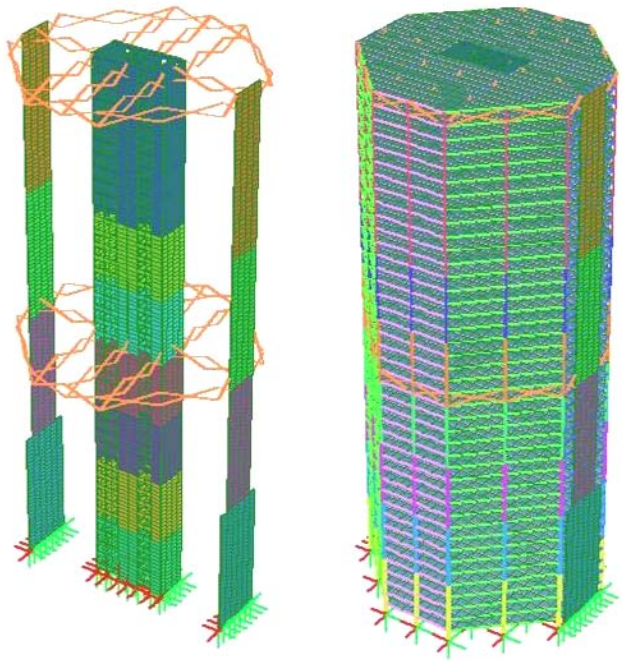

Figure 4. Octagonal Model Elevation (Shear Wall and Full Model)

2.2.3 L-shaped model

L-shaped model with plan dimensions of 60 m and 80 m is selected to study an extended layout with double core walls in both of its arms (Figure 5 & Figure 6). The effects of lateral loads on this model

are studied and compared with the other two less rigid models. The corner wall around the stair well and side walls are needed to stabilise the model and to achieve the desired frequency mode shapes.

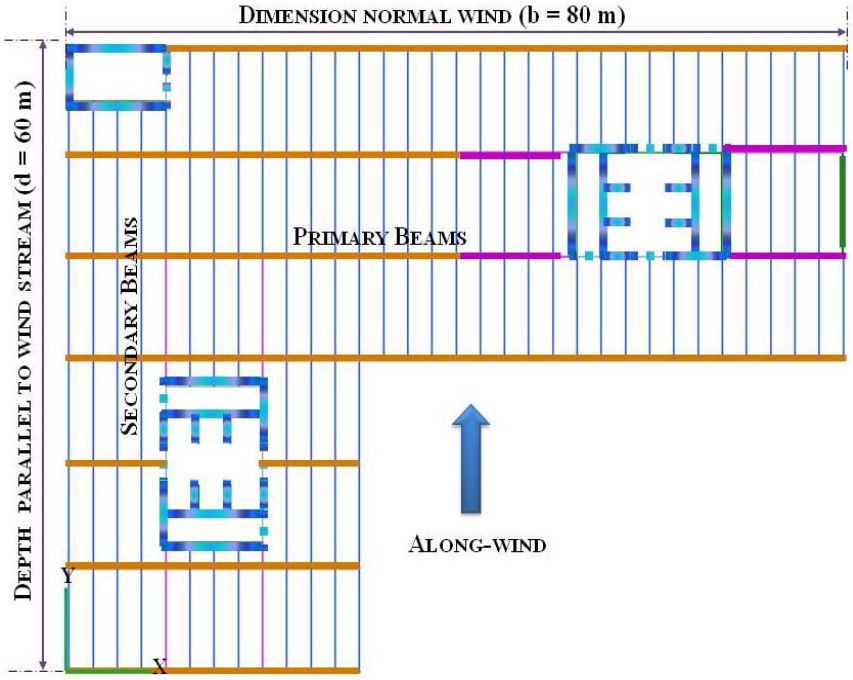

Figure 5. Direction of Wind on L-Shaped Layout

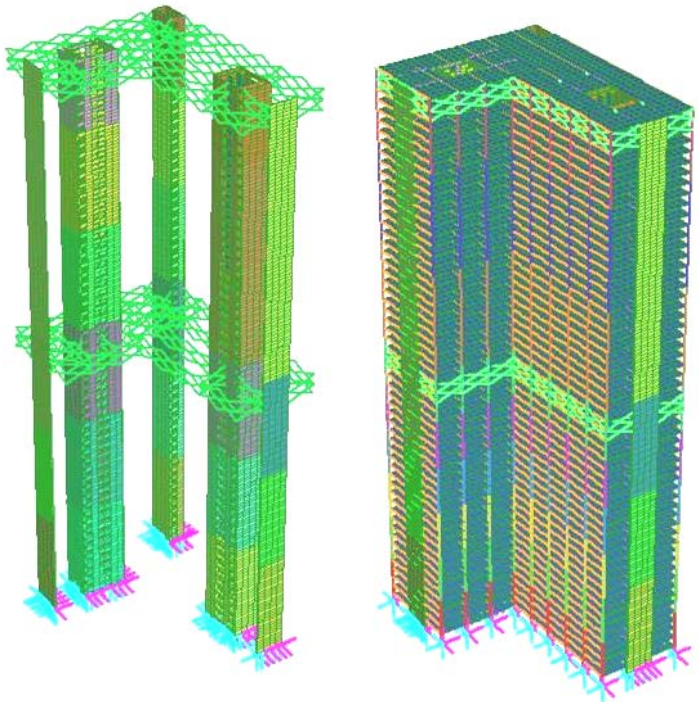

Figure 6. L-Shaped Model Elevation (Shear Wall and Full Model)

2.3 Outriggers Provision in Models

Belt-truss and outriggers are used as secondary bracings for lateral load resistance in conjunction with primary bracings of RCC shear walls. The main focus of this paper is to study the effects of various combinations of belt-truss and outriggers in composite building prototypes.

Many shapes of truss system are available in the market; however, the crucial objective of this study is not the shape of the truss but its location along building height. Therefore, a commonly used system of cross-bracing is adopted. The position of outrigger used in this study are finalised through various model analysis and listed in Table 1. These arrangements are kept same in Rectangular, Octagonal and L-shaped models.

Table 1. Model Arrangements

	Model Title	Model arrangements
Rectangular, L shaped and Octagonal model	***28- Storey***	
	28-1	Without outrigger
	28-2	Outriggers at top
	28-3	Outrigger at mid height
	42-storey	
	42-1	Without outrigger
	42-2	Outrigger at top
	42-3	Outrigger at mid-height
	42-4	Outrigger at top and mid-height
	42-5	Double outrigger at top
	42-6	Double outrigger at mid-height
	57-storey	
	57-1	Without outrigger
	57-2	Outrigger at top
	57-3	Outrigger at 2/3 height (level 38)
	57-4	Outrigger at mid-height (level 29)
	57-5	Outrigger at top and mid-height
	57-6	Outrigger at top, mid-height and 2/3rd height
	57-7	Double outrigger at top
	57-8	Double outrigger at mid-height
	57-9	Double outrigger at 2/3rd height
	57-10	Double outrigger at top and mid-height

3. FRAMING LAYOUT OF MODELS

Models are framed within the applicability of Australian standards AS1170.2 [11] for the maximum height and horizontal dimensions to satisfy requirement of clause 1.1.
Framing components of models consist of:

a. Composite slab is 120 mm thick (overall) including 0.75 mm of corrugated steel sheeting [12]. The transformed properties of composite slab are calculated using Eq. 1 & 2.

Transformed Elastic Modulus of composite Section is given by Eq. 1 :

$$A_c E_c + A_{ST} E_S = A_g E_T \quad (1)$$

Transformed Density of Composite Section is given by Eq. 2 :

$$A_c \gamma_c + A_{ST} \gamma_S = A_g \gamma_T \quad (2)$$

b. Secondary beams are at 2.5 m c/c spacing and structural steel I-sections, selected from design capacity tables of Australian Steel Institute [13].
c. Primary beams are at 10.0 m c/c spacing and structural steel I-sections, selected from design capacity tables of Australian Steel Institute [13].
d. Composite columns are square shaped and placed at 10.0 m spacing, made up of RCC embedded with structural steel I-section selected from design capacity tables of Australian Steel Institute [13]. Columns are divided into two categories i.e. internal column with load catchment area of 100 m^2 / floor and edge columns with load catchment area of 50 m^2 / floor. Transformed properties of column are calculated using Eq. 1 & 2.
e. Shear walls and core walls are provided as RCC walls and serve as primary bracings. Minimum thicknesses and locations of RCC walls are given to satisfy requirements of building code. Shear walls are the main contributor of models optimisation process. The thicknesses and locations of RCC walls are adjusted for each "run" and "re-run" of model to accomplish desired frequencies and vibrational mode shapes of prototypes.
f. Belt-truss and outriggers are structural steel I-sections selected from design capacity tables of Australian Steel Institute [13] and provided as secondary bracings for lateral loads transfer to RCC shear walls. The varied location of belt-truss and outriggers (Table 1) in different models is the basis of this study.
g. Construction type is "Simple Construction", adopted from Australian standard AS 4100[14]. Moment releases are provided at "beam-to-beam" and "beam-to-column" connections (Figure 7).
h. Fixed support is given to columns and RCC walls at the base of model (Figure 8).

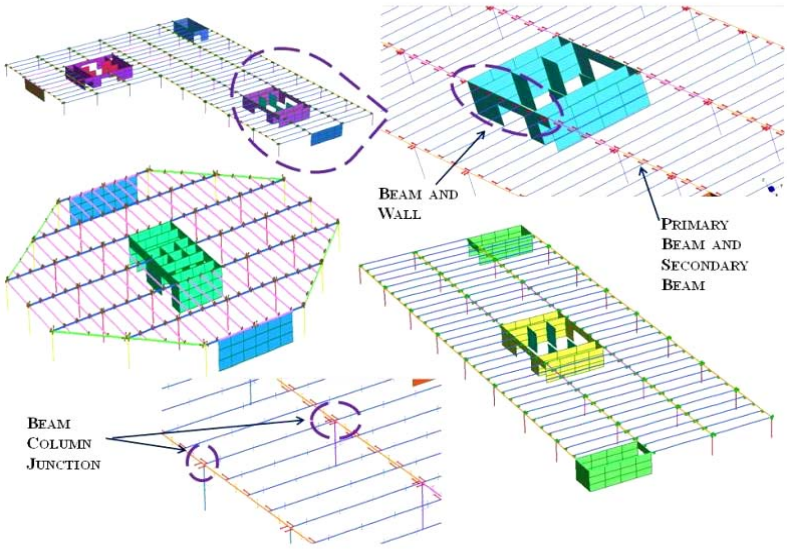

Figure 7. Beam End Releases (Partial Model)

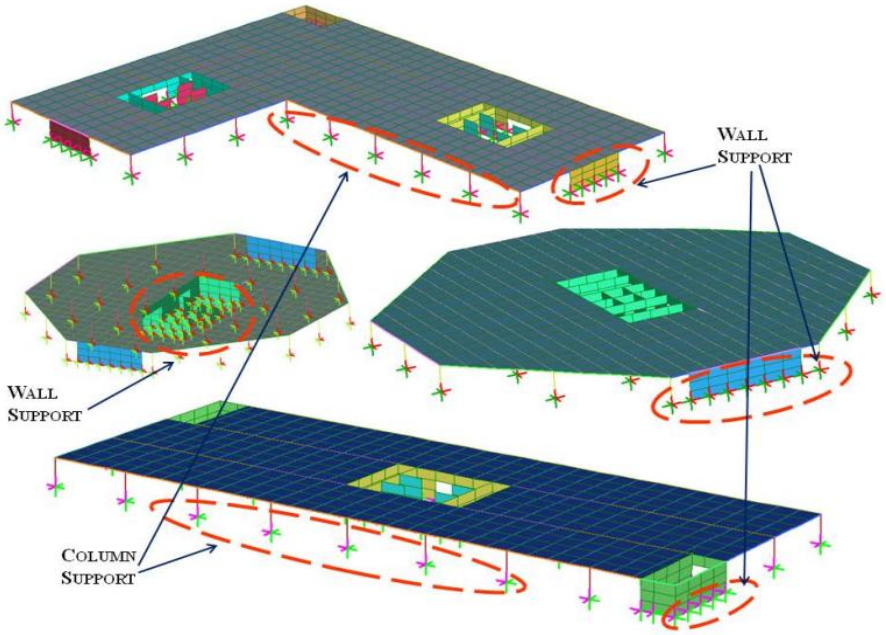

Figure 8. Support at Base (Partial Model)

4. MODELLING VALIDATION

The models are analysed by Strand7 R2.4.4 [15] finite element software. Robustness and accuracy of models are verified by comparing values of interior and exterior column reactions with the manually calculated loads. Further; the results of base shear along wind and cross wind are also compared with those evaluated manually to satisfy the reliability and accuracy of models. The validation summary is given for typical models in Table 2a, 2b and 2c which showed the difference of values calculated manually and through strand7 is within the general acceptable limits of 5% to 10%.

Table 2. Model Validation

Table 2 a: Summary of modelling validation for 57- Storey rectangular model (199.50 m)

Items	Manual Cals	Strand7	Difference
Exterior column load (kN)	11609	11816	1.866%
Interior column load (kN)	24259	24379	0.544%
Base shear – along-wind response (kN)	4398990	4282334	2.65%
Base Shear - crosswind (kN)	3751029	3756480	0.15%

Table 2b: Summary of modelling validation for 42- Storey L- Shaped model (147.0 m)

Items	**Manual Cals**	**Strand7**	**Difference**
Exterior column load (kN)	8315	8363	0.57%
Interior column load (kN)	16929	16631	1.792%
Base shear – along-wind response (kN)	2068261	2177840	5.30%
Base Shear - crosswind (kN)	1983308	1824130	8.03%

Table 2c: Summary of modelling validation for 28- storey octagonal model (98.0 m)

Items	Manual Cals	Strand7	Difference
Exterior column load (kN)	5392	5192	3.7%
Interior column load (kN)	9770	10008	2.44%
Base shear – along-wind response (kN)	798422	733977	8.07%
Base Shear - crosswind (kN)	634895	711264	10.73%

5. WIND ACTION FOR MODELS

Wind actions on any structure or structural component can be "static" or "dynamic" as classified by Australian standard AS1170.2 [11]. The decision of type of actions to be applied on any structure or structural component depends on variables such as frequency, dimensions and site location [16, 17].

Australian Standard AS1170.2 [11] recommended that any structure or structural component with frequency less than 1.0 Hz must be analysed and designed for dynamic wind loads. Models used in this study have frequencies below 1 Hz, therefore; dynamic wind loads are applied in FEM analysis.

6. APPLICATION OF WIND LOADS ON MODELS

Wind action is considered as global phenomenon i.e. acting on overall structure because target is to examine the overall structural serviceability performance. Therefore; these forces are applied as "*Global Pressure*" in kN/m by selecting horizontal beam members on each level in Y-dir. and X-dir. for along-wind and crosswind pressure respectively (Figure 9, Figure 10 & Figure 11).

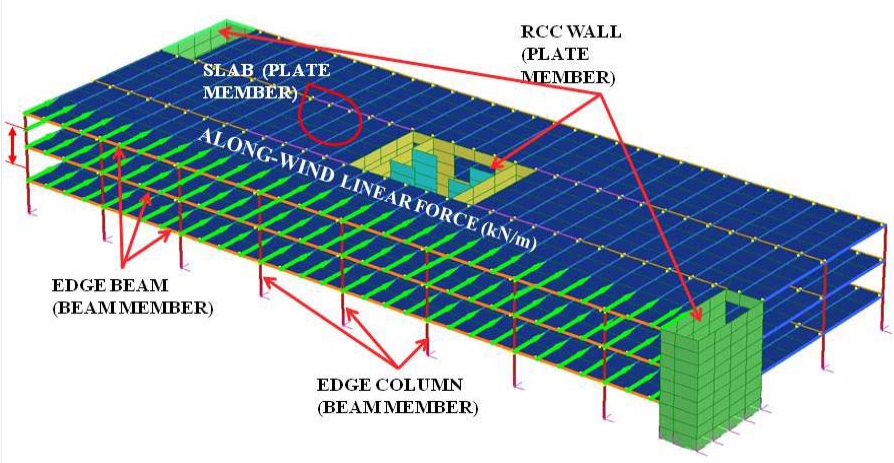

Figure 9. Along-Wind Linear Force on Rectangular Model (Partial Model)

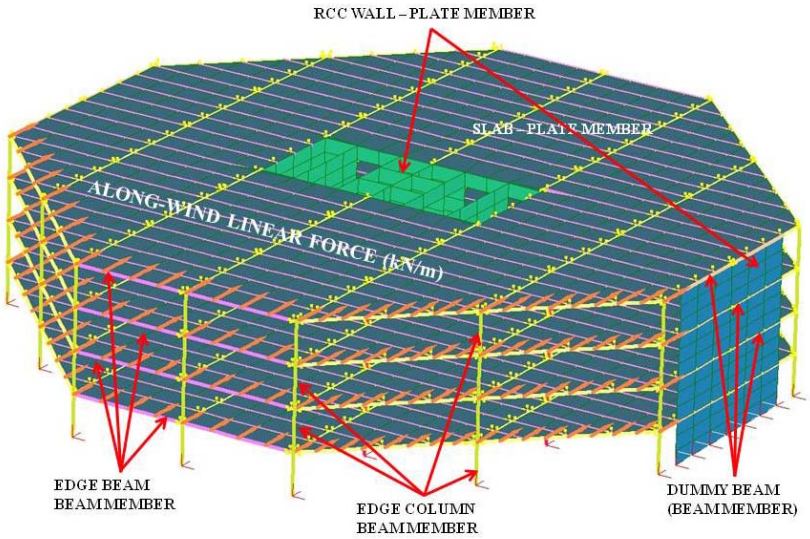

Figure 10. Along-Wind Linear Force on Octagonal Model (Partial Model)

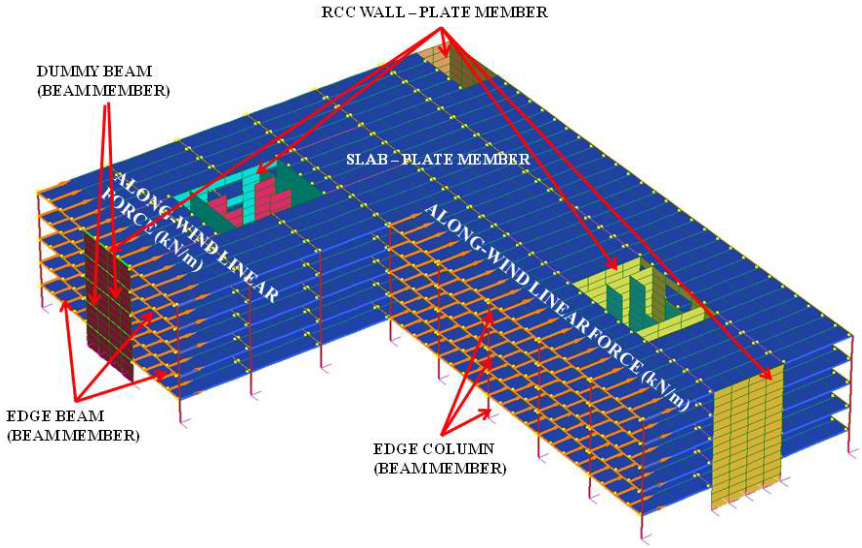

Figure 11. Along-Wind Linear Force on L-Shaped Model (Partial Model)

7. LOAD COMBINATION

The load combination used is as per the guidelines of Australian Standard AS1170.1 [18] and is given in Eq. 3 :

$$Load\ Combination = 0.5G + 1.0\,Wx + 1.0\,Wy \tag{3}$$

In the above equation G stands for gravitational loads whereas, *Wy* and *Wx* are wind in along wind and crosswind direction respectively.

8. RESULTS AND COMPARISON

Table 3, Table 4 and Table 5 are representing the values of frequency and deflections which are extracted from model analysis results. Along wind and cross wind acceleration calculation was not the scope of this research therefore neglected. But future researcher can assess the performance of the location of outrigger braced system by estimating acceleration of multistorey building.

Table 3. Results for Rectangular Models

Rectangular plan models				
Model title	**Frequency**		**Deflection at top**	
	Mode 1 (Y-dir)	**Mode 2 (X-dir)**	**Δ_X**	**Δ_Y**
	Hz	**Hz**	**mm**	**mm**
28-1	0.4253	0.4532	91	136
28-2	0.4466	0.4702	81	122
28-3	0.4492	0.4857	78	125
42-1	0.2160	0.2466	316	480
42-2	0.2314	0.2590	278	411
42-3	0.2322	0.2677	269	419
42-4	0.2456	0.2788	241	368
42-5	0.2428	0.2687	252	369
42-6	0.2475	0.2861	237	372
57-1	0.1682	0.2071	344	624
57-2	0.1745	0.2140	326	592
57-3	0.1761	0.2184	318	591
57-4	0.1751	0.2176	322	601
57-5	0.1806	0.2240	299	556
57-6	0.1863	0.2334	275	522
57-7	0.1797	0.2206	303	554
57-8	0.1812	0.2273	297	563
57-9	0.1830	0.2287	290	547
57-10	0.1905	0.2392	261	496

Table 4. Results for Octagonal Model

Octagonal plan model				
Model title	**Frequency**		**Deflection at top**	
	Mode 1 (Y-dir)	**Mode 2 (X-dir)**	**Δ_X**	**Δ_Y**
	Hz	**Hz**	**mm**	**mm**
28-1	0.415875	0.486169	81	110
28-2	0.415875	0.486169	81	110
28-3	0.415875	0.486169	81	110
42-1	0.199592	0.268083	309	496
42-2	0.236321	0.278908	264	328
42-3	0.254542	0.297667	260	305
42-4	0.284011	0.307887	231	227

Octagonal plan model				
Model title	**Frequency**		**Deflection at top**	
	Mode 1 (Y-dir)	**Mode 2 (X-dir)**	**Δ_X**	**Δ_Y**
	Hz	**Hz**	**mm**	**mm**
42-5	0.251109	0.284212	241	278
42-6	0.285162	0.313097	233	243
57-1	0.16054	0.25698	320	632
57-2	0.17992	0.26406	290	481
57-3	0.19174	0.26836	284	437
57-4	0.1867	0.26629	293	475
57-5	0.20284	0.27226	268	381
57-6	0.22038	0.28032	248	316
57-7	0.18935	0.2697	270	419
57-8	0.20499	0.20499	272	393
57-9	0.21042	0.27729	261	356
57-10	0.22654	0.28414	237	295

Table 5. Results for L-Shaped Model

L-shaped plan model				
Model title	**Frequency**		**Deflection at top**	
	Mode 1 (Y-dir)	**Mode 2 (X-dir)**	**Δ_X**	**Δ_Y**
	Hz	**Hz**	**mm**	**mm**
28-1	0.52037	0.562095	37	82
28-2	0.541861	0.585756	33	75
28-3	0.549083	0.592318	33	76
42-1	0.272314	0.293305	140	317
42-2	0.288653	0.310919	120	284
42-3	0.293108	0.316163	120	285
42-4	0.306936	0.331709	106	260
42-5	0.300782	0.324645	106	260
42-6	0.314111	0.340426	104	256
57-1	0.194008	0.208954	247	594
57-2	0.204443	0.218722	218	538
57-3	0.20871	0.222793	215	529
57-4	0.205941	0.220009	222	544
57-5	0.215409	0.229007	199	499
57-6	0.226422	0.239875	180	462
57-7	0.212267	0.226722	197	501
57-8	0.216236	0.229961	204	506
57-9	0.220845	0.23482	192	483
57-10	0.231927	0.246057	168	441

8.1 Graphical Representation of Output

8.1.1 28-storeys

Deflections and frequencies of 28-storeys models are compared in Figure 12 and Figure 13.

Fundamental Frequency of 28- Storeys Models

respectively. The straight line of octagonal model shows that insertions of outriggers have no effect on deflections. In octagonal model deflection in X-dir. is 80mm while in Y-dir. is 110 mm because of core wall layout contribution of rigidity is higher in X-dir. than in Y-dir.

Graph is similar in L-shaped model for frequency and deflection with higher values in Y-dir. The deflection values are almost unchanged in 28-2 and 28-3 in X-dir. and Y-dir. frequency is also slightly varied in X-axis and Y-axis.

Y-dir. in Rectangular model showed trivial reverse curve in deflection. This stipulates that outriggers at top provide better deflection control.

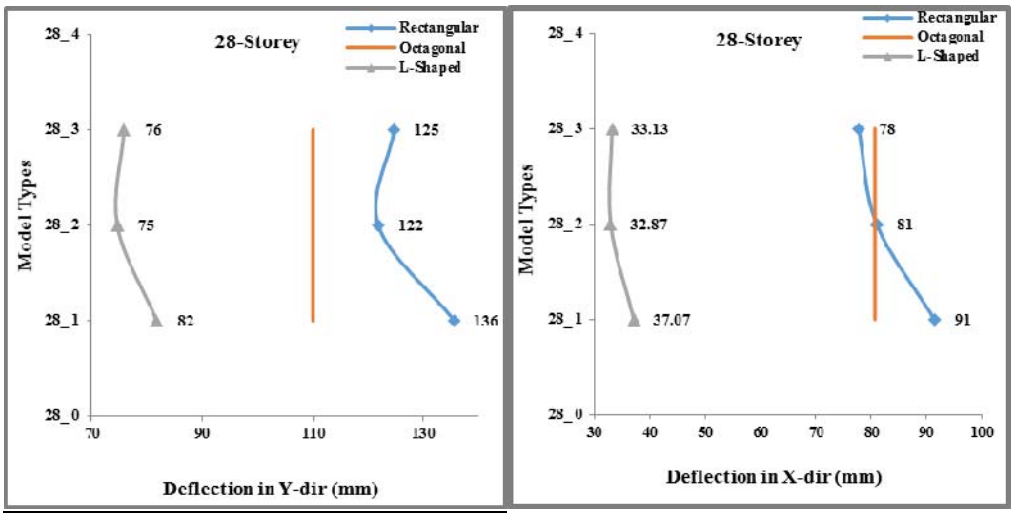

Figure 12. Deflection Comparison of 28- Storeys Models

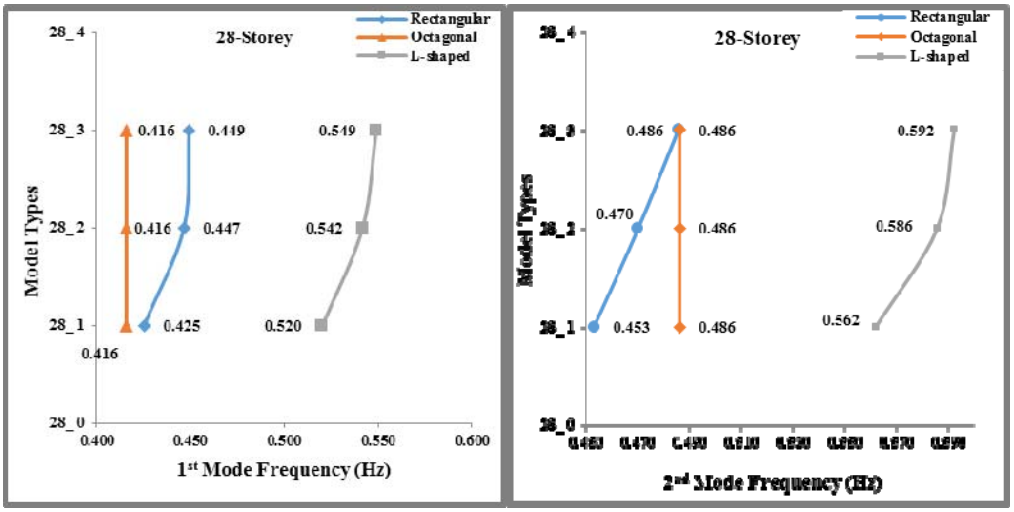

Figure 13. Fundamental Frequency of 28- Storeys Models

8.1.2 42-storey

Six variations of 42-storey models with various arrangements of belt-truss and outriggers are compared in Figure 14 and Figure 15. In octagonal 42-4 model, curve reversed and moved toward right. Although; 42-2 and 42-5 have two outriggers levels but their arrangement effects on deflection.

Rectangular model has reversed curvature between 42-2 and 42-3 which showed that outrigger at top is more effective than in middle. The values of deflection in X-dir. are very similar in Octagonal and Rectangular model whereas; L-shaped model has markedly less deflection. The planar X-dimension of Rectangular and L-shaped models is 80 m. But the shear wall contribution in L-shaped model is higher than in rectangular model.

The frequency variation in octagonal model showed the outrigger affectivity. The 2nd mode frequency in all three plan options have reverse curve at 42-5. 42-4, 42-5 and 42-6 all have double outriggers with different arrangement. The least effective is double outrigger at top i.e. 42-5. Provision of mid-height outrigger has better effects due to the reversal of curvature at mid-height.

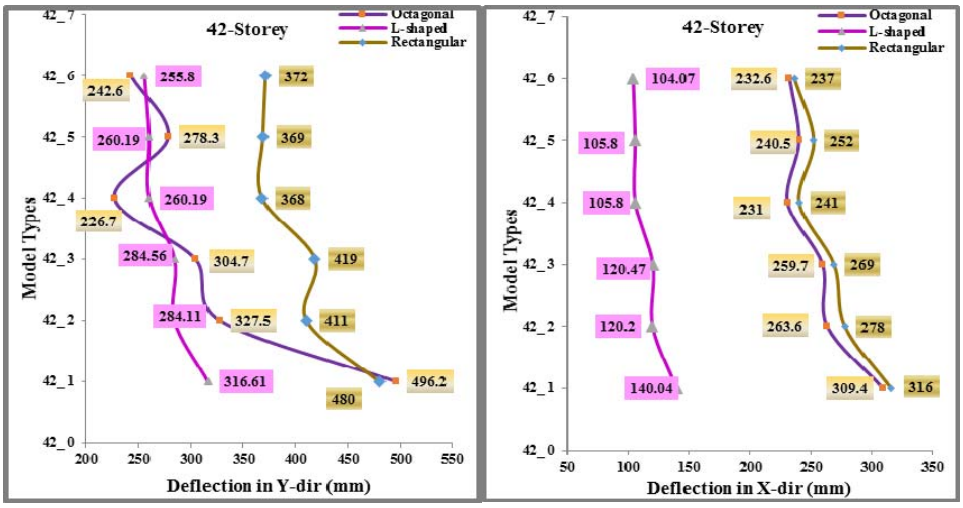

Figure 14. Deflection Comparison of 42- Storeys Models.

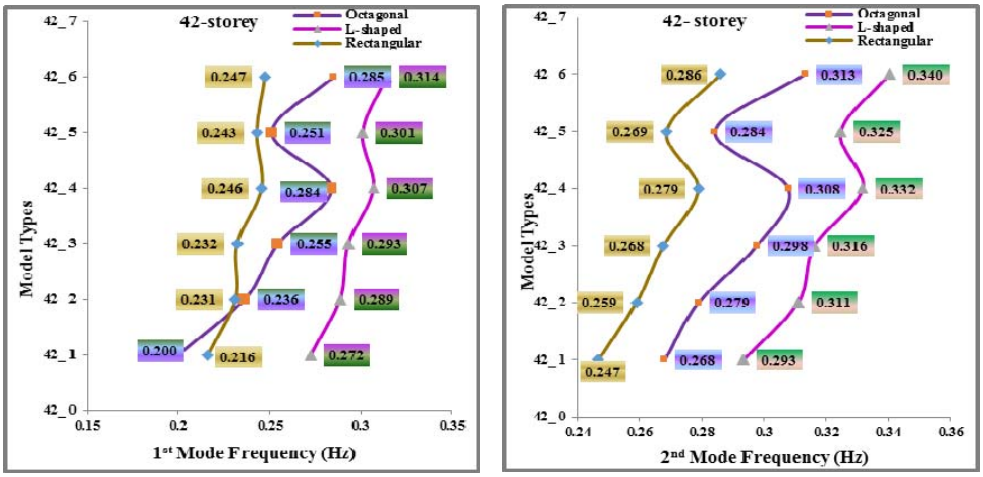

Figure 15. Fundamental Frequency of 42- Storeys Models

8.1.3 57-storeys

Error! Reference source not found. shows deflection curve for 10 models of 57-storeys. Generally; a sharp decline in deflection is observed as one outrigger level is inserted at top floor. This trend continued up to 57-3 which has outriggers at 2/3rd height, however; graph reversed at 57-4 as the outrigger position has changed to mid-height of the model. Addition of outrigger at two positions i.e. at top and mid-height (57-5), again lead to decay of frequency.

The options 57-5, 57-7, 57-8 and 57-9 all have two outrigger levels but minimum deflection is achieved in both axes of 57-9 which is double outrigger at 2/3rd height. The sharpest curve is for octagonal model as seen in **Error! Reference source not found.** and milder curve is of rectangular plan model. The strident increase of frequency by inserting three outrigger levels (i.e. 57-6) and then an abrupt descent in values by providing double outrigger at top (57-7) indicates that frequency is affected by placement of bracings.

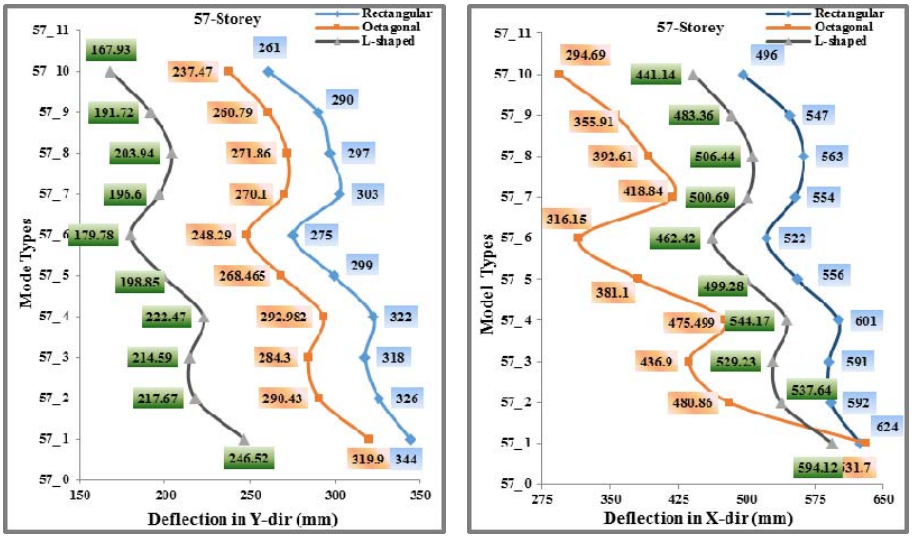

Figure 16. Deflection Comparison of 57- Storeys Models

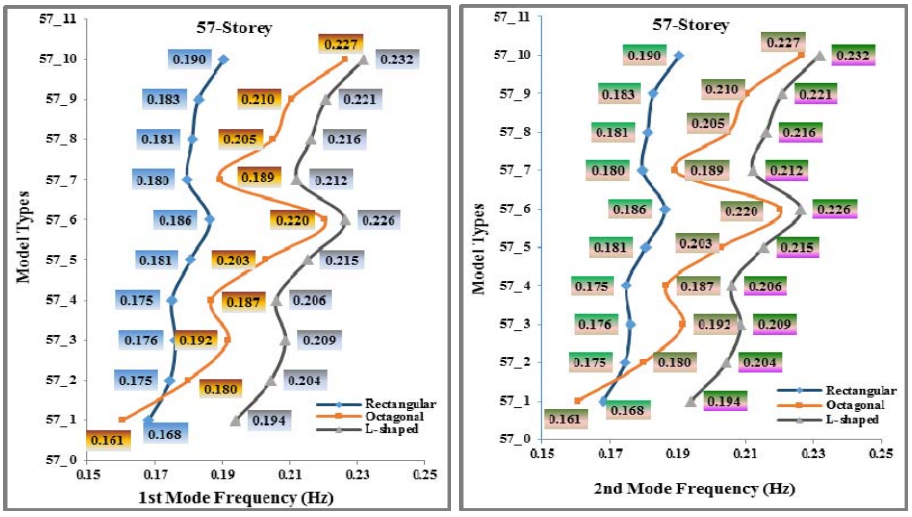

Figure 17. Frequency Comparison of 57- Storeys Models

8.2 Percentage Reductions in Deflection

The relationship of percentage deflection decline in various models in comparison of model "without belt-truss and outriggers" is given by Eq. 4. The values of lateral displacement decrement are provided in Table 6.

$$\%\Delta_{(reduction)} = \frac{\Delta_{(model\ without\ outrigger)} - \Delta_{(any\ model\ arrangement)}}{\Delta_{(model\ without\ outrigger)}}\ x\ 100 \quad (4)$$

28-storey octagonal model is not affected by any of the outrigger arrangements. Rectangular model has least value in 28-2 while L-shaped has lowest value in 28-3. Rectangular and octagonal models have maximum reduction in deflection in 42-6 for X-axis and 42-4 for Y-axis. L-shaped model has maximum deflection reduction in 42-6 in both axes. In all 57-storeys maximum reduction of deflection is obtained in 57-10.

Table 6. Percentage Reduction in Deflection

% Reduction in deflection						
Model title	**Rectangular**		**Octagonal**		**L-shaped**	
	$\%\Delta_X$	**$\%\Delta_Y$**	**$\%\Delta_X$**	**$\%\Delta_Y$**	**$\%\Delta_X$**	**$\%\Delta_Y$**
28-1	0%	0%	0%	0%	0%	0%
28-2	11.50%	10.20%	0%	0%	11.30%	8.70%
28-3	15.10%	8.10%	0%	0%	10.60%	7.20%
42-1	0%	0%	0%	0%	0%	0%
42-2	12.10%	14.60%	14.80%	34.00%	14.20%	10.30%
42-3	14.90%	12.80%	16.10%	38.60%	14.00%	10.10%
42-4	23.90%	23.40%	25.30%	54.30%	24.50%	17.80%
42-5	20.20%	23.20%	22.30%	43.90%	24.50%	17.80%
42-6	25.20%	22.70%	24.80%	51.10%	25.70%	19.20%
57-1	0%	0%	0%	0%	0%	0%
57-2	5.50%	5.20%	9.20%	23.90%	11.70%	9.50%
57-3	7.80%	5.40%	11.10%	30.80%	13.00%	10.90%
57-4	6.50%	3.80%	8.40%	24.70%	9.80%	8.40%
57-5	13.10%	11.00%	16.10%	39.70%	19.30%	16.00%
57-6	20.10%	16.50%	22.40%	50.00%	27.10%	22.20%
57-7	12.10%	11.40%	15.60%	33.70%	20.20%	15.70%
57-8	13.80%	9.90%	15.00%	37.80%	17.30%	14.80%
57-9	15.80%	12.40%	18.50%	43.70%	22.20%	18.60%
57-10	24.30%	20.60%	25.80%	53.30%	31.90%	25.70%

8.3 Percentage Frequency Increments

The frequencies in Table 7 shows very similar trend for all three model heights and the highest frequency value is achieved with maximum number of belt-truss and outriggers floors. These are calculated according to Eq. 5.

$$\%f_{(increment)} = \frac{f_{(any\ model\ arrangement)} - f_{(model\ without\ outrigger)}}{f_{(model\ without\ outrigger)}}\ x\ 100 \quad (5)$$

The frequency is a characteristic of stiffness, more stiffness higher frequency however; frequency also get affected by belt-truss and outriggers placement. For instance; 57-5, 57-7 57-8 and 57-9 have two outrigger floors at various levels. Theoretically the overall stiffness is same in these three options, however; maximum percentage increment is attained in 57-9, which is double outrigger level at 2/3rd height of building. The placement of belt-truss and outriggers change the centre of gravity of model and impact on vertical curvature which in turn affect the frequency of model.

In 42-storeys, comparison of 42-4, 42-5 and 42-6 showed that the maximum frequency increment is obtained in 42-6. Although; three of these have the same mass but different truss placement changes the centre of gravity of model and results in changed frequency.

Table 7. Percentage Increment in Frequency

% Increase in frequency values						
Model title	**Rectangular**		**Octagonal**		**L-shaped**	
	%f_{1st}	**%f_{2nd}**	**%f_{1st}**	**%f_{2nd}**	**%f_{1st}**	**%f_{2nd}**
28-1	0.00%	0.00%	0%	0%	0.00%	0.00%
28-2	5.00%	3.76%	0%	0%	4.13%	4.21%
28-3	5.62%	7.17%	0%	0%	5.52%	5.38%
42-1	0%	0%	0%	0%	0%	0%
42-2	7.16%	5.00%	18.40%	4.04%	6.00%	6.01%
42-3	7.51%	8.53%	27.53%	11.04%	7.64%	7.79%
42-4	13.72%	13.05%	42.30%	14.85%	12.71%	13.09%
42-5	12.45%	8.95%	25.81%	6.02%	10.45%	10.69%
42-6	14.60%	15.99%	42.87%	16.79%	15.35%	16.07%
57-1	0.00%	0.00%	0.00%	0.00%	0.00%	0.00%
57-2	3.77%	3.34%	12.07%	2.76%	5.38%	4.67%
57-3	4.69%	5.46%	19.44%	4.43%	7.58%	6.62%
57-4	4.08%	5.06%	16.30%	3.62%	6.15%	5.29%
57-5	7.36%	8.15%	26.35%	5.95%	11.03%	9.60%
57-6	10.74%	12.68%	37.28%	9.08%	16.71%	14.80%
57-7	6.84%	6.51%	17.95%	4.95%	9.41%	8.50%
57-8	7.71%	9.75%	27.69%	6.73%	11.46%	10.05%
57-9	8.78%	10.41%	31.07%	7.90%	13.83%	12.38%
57-10	13.25%	15.50%	41.11%	10.57%	19.55%	17.76%

9. CONCLUSIONS

This study investigated the behaviour of multi-storey composite buildings when subjected to cyclonic wind loads with different combination of steel belt-truss and outriggers for different plan layouts and for different heights of the building. The results demonstrate that wind action is responsive to the number and placement of belt-truss and outriggers as well as to the different plan layout and height of the building. The findings of the investigation can be summarizes as:

- 28-storey provided best result with the addition of bracings at top level of model in three plan layout.
- Provision of single outrigger level in 42-storey has varied outcome in three different plans for single outrigger option. However; provision of single level outrigger at mid-height of model is more desired option.

- In double outrigger option, provision of double level of outrigger at mid-height in 42-storey provide maximum reduction of lateral deflection.
- In 57-storey it is found out that if one floor of outrigger is required to be placed in building than provision of one level outrigger at 2/3rd height (measured from ground level) is the best option.
- In case of double belt-truss and outriggers levels in 57-storey model, the provision of secondary outrigger at 2/3rd height (measured from ground level) is the most suitable alternative.
- Three single level outrigger at top of model, 2/3rd height from base and mid-height of building is more appropriate than providing two double outrigger levels.

NOTATION

A_c = Area of concrete
A_g = Gross area of section
A_{ST} = Area of steel
E_c = Elastic modulus of concrete
E_s = Elastic Modulus of steel
E_T = Elastic modulus of transformed section
FEM = Finite Element Modelling
RCC = Reinforced Concrete Cement
γ_c =Density of concrete
γ_s = Density of steel
γ_T = density of transformed section
G = gravitational loads
Wx = wind in X-direction
Wy = wind in Y-direction

REFERENCES

[1] Nanduri, P.M.B., Raj, Kiran., Suresh, B., Hussain, M.D. and Ihtesham., "Optimum Position of Outrigger System for High-rise Reinforced Concrete Buildings under Wind and Earthquake Loadings", American Journal of Engineering Research (AJER), 2013, Vol. 2, No. 8, pp. 76-89.

[2] Chung, Y.K., "Optimization of Outrigger Locations in Tall Buildings Subjected to Wind Loads", Masters Research Thesis, 2010, –School of Civil and Environmental Engineering, The University of Melbourne.

[3] Kian, P.S. and Siahaan, F.T., "The Use of Outrigger and Belt Truss System for High-rise Concrete Buildings", Dimensi Teknit Sipil, 2001, Vol. 3, No. 1, pp. 36-41.

[4] Hoenderkamp, J.C.D., and Bakker, C.M., "Analysis of High-rise Braced Frames with Outriggers", Journal of Structural Design of Tall and Special Buildings, 2003, Vol. 12, pp. 335-350.

[5] Hoenderkamp, J.C.D., "Second Outrigger at Optimum Location on High-rise Shear Wall", Journal of Structural Design of Tall and Special Buildings, 2007, Vol. 17, pp. 619–634.

[6] Lee, J., Bangi, M. and Kim, J., "An Analytical Model for High-rise Wall-frame Structures with Outriggers", Journal of Structural Design of Tall and Special Buildings, 2008, Vol. 17, pp. 839–851.

[7] Lee, J., Park, D., Lee, K., and Ahn, N., "Geometric Nonlinear Analysis of Tall Building Structures with Outriggers", Structural Design of Tall and Special Buildings, 2013, Vol. 22, pp. 454-470.

[8] Taranath, B.S., "Structural Analysis and Design of Tall Buildings: Steel and Composite Construction", CRC Press 2011, Print ISBN: 978-1-4398-5089-3, eBook ISBN: 978-1-4398-5090-9, 2012.

[9] Taranath, B.S., "Wind and Earthquake Resistant Buildings: Structural Analysis and Design", CRC Press 2004, Print ISBN: 978-0-8247-5934-6, eBook ISBN: 978-0-8493-3809-0, 2005.

[10] Rahgozar, R. and Sharifi, Y., "An Approximate Analysis of Framed Tube, Shear Core and Belt Truss in High-rise Building", Struct. Design Tall Spec Build, 2009, Vol. 18, pp. 607–624.

[11] AS1170.2., "Structural Design Actions: part 2 – Wind Actions (AS/NZS 1170.2:2011)", 2011, Retrieved from http://www.saiglobal.com/

[12] Lysaght Bondek., "Structural Steel Decking Syaytem Design and Construction Manual", Bluescope Steel Limited, 2012, Retrieved from http://www.bluescopesteel.com.au/files/dmfile/BondekDesignAnd ConstructionManualJune2012.pdf

[13] Australian Steel Institute, "Design Capacity Tables for Structural Steel", Volume 1- Open Sections [5th ed.], 2009, Sydney, NSW: ASI Publishing.

[14] AS4100, "Steel Structures", Australian Standard. 1998, Retrieved from http://www.saiglobal.com.ezp01.library.qut.edu.au/online/autologin.asp.

[15] Strand7 Release 2.4.4., "Strand7 Pty Ltd", 2011, Copyright Strand7 Pty Ltd. Retrieved from http://www.strand7.com/.

[16] Fawzia, S., Nasir, A. and Fatima,T., "Study of the Effectiveness of Outrigger System for High-rise Composite Buildings for Cyclonic Region", Proceedings of the World Academy of Science, Engineering and Technology, Phuket, Thailand, 2011, pp. 937-945.

[17] Fawzia, S. and Fatima, T., "Deflection Control in Composite Building by Using Belt Truss and Outrigger System", Proceedings of the 2010 World Academy of Science, Engineering and Technology conference, Singapore 2010, pp. 25-27.

[18] AS 1170.1., "Structural Design Actions Part 1: Permanent, Imposed and Other Actions (AS/NZS 1170.1:2002)", 2002, Retrieved from http://www.saiglobal.com/.

BEHAVIOUR OF SEMI-RIGID STEEL FRAMES WITH STEEL PLATE SHEAR WALLS

J.G. Yu [1,*] and J.P. Hao [2]

[1] *Associate Professor, Department of Civil Engineering, Xi'an University of Architecture and Technology, Xi'an, China*
[2] *Professor, Department of Civil Engineering, Xi'an University of Architecture and Technology, Xi'an, China*
**(Corresponding author: E-mail: yjggordon@163.com)*

Received: 17 February 2015; Revised: 7 May 2015; Accepted: 28 July 2015

ABSTRACT: This paper describes an investigation on the seismic behaviour of a new lateral resistance system which combines semi-rigid steel frames (SRSFs) with steel plate shear walls (SPSWs). A laboratory test, including two 1/3-scale one-bay, two-storey SRSFs with SPSWs, was conducted to study the influence of the stiffeners on SPSWs and the stiffness of beam-column connections. The results indicate that the new system inherits the merits both of SRSFs and SPSWs. It exhibits excellent seismic performance in terms of load carrying capacity, ductility, stiffness and energy dissipation. The stiffeners on SPSWs not only effectively reduce the forces taken by beams and columns but also improve the overall cyclic performance of structural systems. Moreover, they increase the initial stiffness and buckling load capacity of SPSWs especially. Further, the finite element analysis method was adopted for parametric study of the influence of connection stiffness and stiffener rigidity on the behaviour of SRSF-SPSW. It demonstrates that the SPSW in the proposed structural system undertakes 70%-80% of overall lateral load. The influence of connection stiffness on the load carrying capacity depends on the stiffness of columns and thickness of infill plates. This influence is enlarged with increasing stiffness of columns and reducing thickness of infill plates. The load carrying capacity of a structural system is increased by 42.2% when connections are changed from pin to rigid. Generally, this research provides a basis for engineering application and theoretical analysis of the SRSF-SPSW structural system.

Keywords: Steel frame, Semi-rigid connection, Steel plate shear wall, Seismic behavior, Beam-column connection stiffness, Nonlinear finite element analysis

DOI: 10.18057/IJASC.2016.12.2.5

1. INTRODUCTION

Steel plate shear walls (SPSWs) have many advantages, including high initial lateral stiffness, stable hysteresis behaviour and good energy dissipation as evidenced by a series of analytical and experimental studies at the University of Alberta [1]. Many experimental studies on single or multi-storey SPSWs were performed to assess the influence of design parameters [2]-[12]. Parts of the experimental investigations are summarized in Table 1. Tsai and Li [7], Alinia and Dastfan [13], Alavi and Nateghi [14] and Nie *et al.* [15] further investigated SPSWs with various types of stiffener, including longitudinal stiffener, transverse stiffener, cross stiffener, diagonal stiffener, vertical and horizontal ribbed stiffener, etc.

In the traditional analysis and design of steel frames, beam-column connections are often assumed to be rigid or pinned. However, beam-column connections in a structure normally lie in between the above-mentioned two conditions. It is reasonable to consider them as semi-rigid connections in the design of steel frames. The seismic behaviour of steel frames with semi-rigid beam-column connections has been widely studied in the past [16]-[20]. Azizinamini and Radziminski [16], Elnashai and Elghazouli [17] and Kishi *et al.* [18] verified that semi-rigid frames possess excellent ductility and stable hysteretic behaviour. Bernuzzi *et al.* [19] demonstrated that semi-rigid

connections have adequate energy dissipation capacity. Nevertheless, low stiffness and a nonlinear response of semi-rigid connection restrain the application of this structural system. For instance, semi-rigid connections weaken overall stability of structures, especially at large drift ratio [20]. Therefore, it is beneficial to enhance the lateral stiffness of semi-rigid steel frames (SRSFs).

A new structural system taking advantage of SRSFs and SPSWs is proposed in this study. Incorporation of SPSWs in a SRSF can alleviate its ductility requirements in beam-column connections as well as improve the mechanical behaviour of connections, increase stiffness and energy dissipation of the structural system, and realize multi-failure criteria [21]. Beam-column connections are normally designed as rigid ones in most tests and analysis of the SPSW system. SPSW systems with hinged connections or with consideration of connection stiffness are analyzed only in a few studies. Caccese *et al.* [22] tested six unstiffened thin SPSW specimens with moment-resisting connections or shear connections. The test results indicated that initial stiffness of beam-column connections had little influence on the overall behaviour of the SPSW system. However, Kulak *et al.* [23] pointed out that the overall behaviour of the SPSW system is affected by lots of factors, such as material properties, welding cracks and geometric defect. In addition, Xue [24] and Alinia and Dastfan [25] also concluded that beam-column connections had no obvious influence on the overall behaviour of SPSWs based on finite element studies. Nowadays, the influence of beam-column connections on the behaviour of SPSWs is still debatable. More investigation of SPSW with different beam-column connections is needed.

Table 1. Summary of tests on SPSWs

Reference	Specimen	Scale	Depth-width ratio	Height-thickness ratio	Column flexibility factor
Lubell and Prion [2]	SPSW2	1:4	1.00	549	3.35
Chen and Guo [3]	-	1:3	1.00	273	2.52
	-	1:3	1.00	170	2.28
Wang [4]	H1, H2	1:3	1.28	363	2.79
	F1, F2	1:3	1.28	363	2.12
Lin and Tsai [5]	S	1:2	0.50	511	1.01
Park *et al* [6]	SC2T	1:3	0.68	500	1.24
	SC4T	1:3	0.68	250	1.44
	SC5T	1:3	0.68	167	1.58
Tsai and Li [7]	SPSW N	1:1	1.52	1144	2.50
	SPSW S	1:1	1.52	1143	3.01
Qu and Bruneau [8]	-	1:1	1.00	1123	1.95

This paper systematically studies the influences of connection stiffness on the behaviour of SPSWs and examines the seismic behaviour of the SRSF-SPSW structural system. In addition, explanations for insignificant influence of beam-column connection on the overall behaviour of the SPSW system are addressed. This is mainly attributed to the fact that large column flexibility of specimens dominates the overall behaviour of the SPSW system. In this paper, the seismic behaviour of the SRSF-SPSW structural system is investigated through experimental and numerical studies. Two one-bay, two-storey SRSF-SPSWs were tested under constant axial loading and lateral cyclic loading. Steel plates with and without stiffeners and stiffness of beam-column connections were compared in the test. In addition to experimental study, a nonlinear finite element analysis was performed for parametric study. It estimated the influence of connection stiffness and stiffener rigidity of SPSWs on the seismic behaviour of the structural system.

2. EXPERIMENTAL PROGRAMME

2.1 Specimens

A one-bay, two-storey frame was designed to represent the bottom two floors of a frame-shear wall structure. Two specimens namely HAC and HPP were differentiated by beam-column connection and stiffeners on SPSWs. Details of the specimens are shown in Figure 1. The span of the specimen was 1350 mm and the height was 2750 mm. The cross-sections of the bottom beam, intermediate beam and top beam were H410×350×12×25, H200×100×5.5×8 and H300×150×6.5×9, respectively. Both columns had cross-sections of H150×150×7×10. L140×90×8 was adopted for the top and seat angle while L70×8 was used for the web angle in the semi-rigid connection. The thickness of the infill steel plate was 4 mm. Steel plates with 40 mm depth and 4 mm thick were used for stiffeners. The infill plates were welded to the columns and the beams by fish plates. Semi-rigid beam-column connections were adopted in both specimens. Top and intermediate beam-column connections were identified as HAC-T and HAC-M in specimen HAC (or HPP-T and HPP-M in specimen HPP), respectively. The details of beam-column connections are shown in Figure 2.

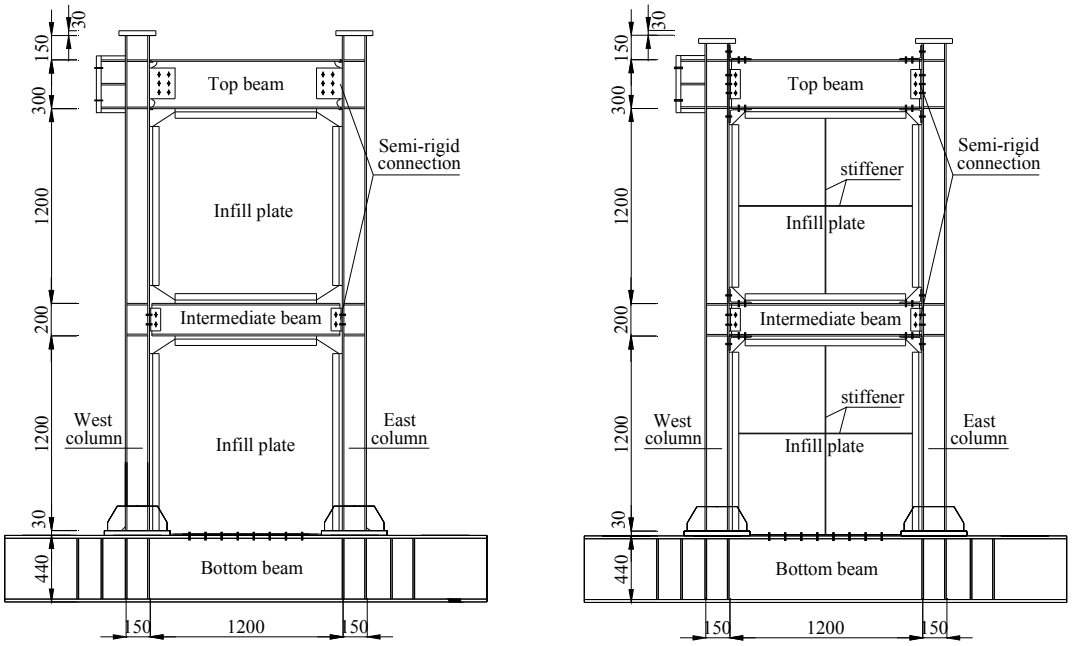

(a) Specimen HAC (b) Specimen HPP

Figure 1. Details of the Specimens

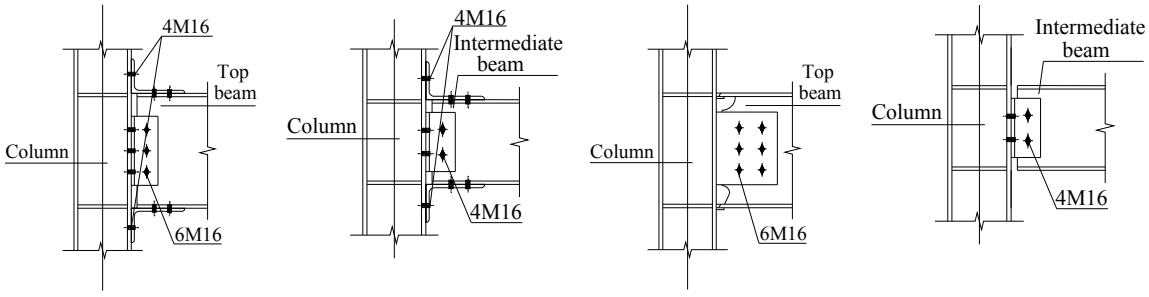

(a) HAC-T (b) HAC-M (c) HPP-T (d) HPP-M

Figure 2. Details of the Semi-rigid Connections

The model scale was about 1/3. The specimens were built using Q235 steel which has a characteristic yield strength of 235N/mm^2. A material property test was conducted according to Chinese national standards "Metallic materials-Tensile testing at ambient temperature (GB/T228-2002)" [27] and "Steel and steel products-Location and preparation of test pieces for mechanic testing (GB/T 2975-1998)" [26]. The material properties of each component are shown in Table 2.

Table 2. Material Properties

Member	Yield stress f_y (N/mm^2)	Ultimate stress f_u (N/mm^2)	Elongation (%)	Elastic modulus E (10^5N/mm^2)
H300×150×6.5×9	275.67	445.33	27.70	2.16
H200×100×5.5×8	314.77	455.47	24.66	2.21
H150×150×7×10	269.33	428.23	21.16	2.00
4.0mm steel plate	356.50	515.53	22.59	2.15
L70×8	353.31	461.62	19.06	2.10
L140×90×8	284.60	424.20	22.20	2.10

2.2 Test Setup, Loading Sequence and Instrumentation

The test setup for the specimen is shown in Figure 3. The tests were conducted in the Structural Engineering Research Laboratory at Xi'an University of Architecture and Technology. The specimens were fixed on the strong floor through high strength steel rods. A reaction beam was established for applying axial load. A lateral support system was established for restraining out-of-plane movement of the specimen. Vertical constant axial loading was applied by two 2000 kN jacks while lateral loading was applied by a two-direction 1000 kN MTS hydraulic actuator. To study the overall connection performance of the structure, the arrangement of displacement transducers was as shown in Figure 4.

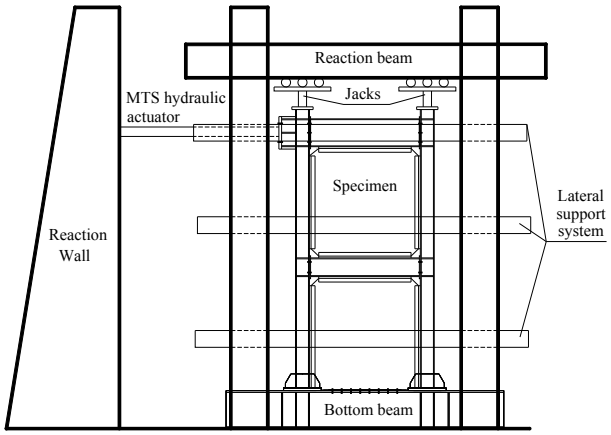

Figure 3. Test Setup

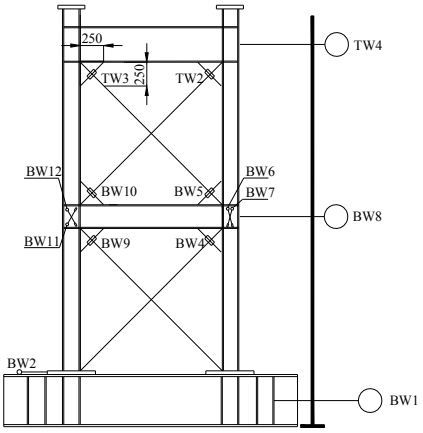

Figure 4. Displacement Transducers Configuration

The loading sequence for testing the specimen was determined according to provisions in "Specification of Testing Methods for Earthquake Resistant Building (JGJ 101-96)" [28]. In order to study the behaviour of SPSWs with pre-compressed frame columns, vertical constant axial loading was first applied on the top of the columns at 200 kN. In the second stage of loading, lateral cyclic loading was applied along the centre line of the top beam. It was noted that only one concentrated load was considered due to the limitation of the test setup. Lateral loading was applied in two steps: loading control in the elastic stage and displacement control after yield. Yield displacement was determined based on the load-displacement response to check strains of steel at critical sections (e.g. the top and bottom of column). Subsequently, lateral displacement was

applied at 1, 1.5, 2, 2.5, … 0.5n times of yield displacement and was repeated three times at each specific displacement. The test was stopped when the lateral displacement reached the maximum deformation at H/50, where H is the height of the specimen.

3. EXPERIMENTAL RESULTS

3.1 General Behaviour

3.1.1 Specimen HPP

The typical behaviour of specimen HPP during the test is shown in Figure 5. At the initial stage of loading, the infill plate in the first storey tended to buckle along the diagonal direction when lateral load reached 300 kN while that remained elastic in the second storey. As a result, residual deformation of the infill plate in the first storey was observed. The specimen HPP yielded at a lateral load of 450 kN. Under this load, yielding displacement δ_y was measured as 12 mm. Subsequently, specimen HPP was tested under displacement control. At a lateral displacement of $1.5\delta_y$, tension straps were found in the infill plate in the first storey while buckling in the flange of the first storey east corner column was found as shown in Figure 5(a). As lateral displacement increased, crossed out-of-plane residual deformation of the infill plate in the first storey was found at a displacement of $2\delta_y$. Afterwards, the specimen reached the peak lateral load in the push direction at the first cycle of $2.5\delta_y$ displacement. The east column in the first storey exhibited out-of-plane bending as shown in Figure 5(b). As displacement reversed, the infill plate in the first storey fractured at the west upper corner as shown in Figure 5(c). Meanwhile, the infill plate in the second storey remained elastic. The specimen reached peak lateral load in the pull direction at the first cycle of $3\delta_y$ displacement. The infill plate in the first storey cracked from the fish plate in the east upper direction. The east column exhibited out-of-plane bending while the west column had obvious concavities. At a displacement of $3.5\delta_y$, the column flange distorted in the west upper corner of the first storey and the infill plate in the first storey formed the first penetrating crack as shown in Figure 5(d). Beam-column connections rotated and the beam separated from the flange of columns with 1-3 mm as shown in Figure 5(e). At an advanced stage of loading, a tension field was formed in the infill plate in the second storey while diagonal "X"-shaped cracks occurred in the infill plate of the first storey. The test was stopped at a displacement of $4.5\delta_y$ when lateral loading decreased to approximately 80% of the peak lateral load. Cracks formed of about 4 mm wide between outside flanges of the columns and foots as shown in Figure 5(f), i.e., the specimen failed with plastic hinges in the columns. No deformation of the top beam-column connection was recorded throughout the test.

(a) Buckling of column flange

(b) Out-of-plane buckling of column

(c) Plate weld tearing

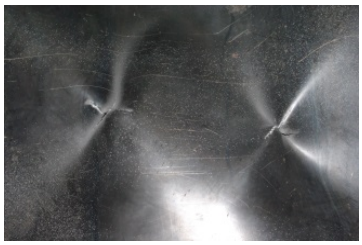

(d) Tearing of infill plate in the first story

(e) Connection rotating

(f) Tearing at the column foot

Figure 5. Typical Behavior of Specimen HPP during the Test

3.1.2 Specimen HAC

The typical behaviour of specimen HAC during the test is shown in Figure 6. With the reinforce of stiffeners, buckling of the infill plate in the specimen HAC occurred at higher lateral loading compared with HPP. The infill plate in the first storey bulged slightly in the upper right region in the first cycle of 500 kN lateral loading. Top and seat angles in the west top connection were opened and closed during the cyclic loading. The yield displacement for specimen HAC was 11.9 mm and the corresponding lateral load was 450.9 kN. The infill plate in the first storey buckled at the upper region in the first cycle of $1.5\delta_y$ displacement. Tension straps in both infill plates developed gradually while top and seat angles at the connections deformed with residual displacement. Buckling of the vertical stiffener occurred in the infill plate of the first storey at a displacement of $2.0\delta_y$. Local buckling at the west column induced fracture of the angle plate connecting the beam to the column as shown in Figure 6(a). As the purpose of the test was to investigate the effect of SPSWs on seismic performance of composite frames, the angle plate was replaced before continuing the test. At a displacement of $2.5\delta_y$, out-of-plane deformation of the infill plate was significant. Buckling of the infill plate reversed with a loud noise during the test. The column buckled at the inner flange below the intermediate beam while the welding of the west column to foot cracked. Meanwhile, welding of stiffeners in the top connection of the west column fractured. Subsequently, both columns buckled below the middle connections in the second cycle of $3.0\delta_y$ displacement as shown in Figure 6(b). Buckling of stiffeners in the first storey infill plate occurred at the third cycle of $3.0\delta_y$ displacement as shown in Figure 6(c). At an advanced stage of loading, the residual out-of-plane deformation of the first storey infill plate was about 8 mm. The lateral load decreased significantly as welding of the west column cracked as shown in Figure 6(d). The test was stopped at $3.5\delta_y$ displacement when serious out-of-plane flexural and torsional buckling occurred for the specimen as shown in Figure 6(e).

(a) Fracture of Angle Plate

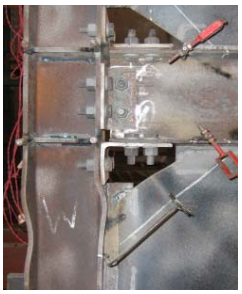

(b) Buckling of Column Flange


(c) Multi-buckling of stiffeners


(d) Welds tearing at column foot


(e) Out-of-plane buckling of column

Figure 6. Typical Behavior of Specimen HAC during the Test

3.2 Failure Modes

The failure modes of the specimens are shown in Figure 7. Specimen HPP exhibited obvious tension straps in infill plates and local tearing at the intersection of tension straps. Plastic hinges formed at column-foot connections and under intermediate beam-column connections accompanied by buckling of the column and angle plate above the connections. Residual deformation of the upper infill plate was smaller than that of the bottom infill plate. For specimen HAC, multi-buckling of stiffeners occurred in both infill plates. However, stiffeners are effective to restrain out-of-plane deformation of the infill plate and to reduce the concavity of the columns. Similar to specimen HPP, plastic hinges formed at column-foot connections and under intermediate beam-column connections. The out-of-plane residual deformation was as much as 10 mm in the bottom infill plate. Bending and torsion out-of-plane deformation of the frame columns was significant. Three types of buckling in the stiffened SPSW were identified, including overall buckling, local buckling in the cell grids and relative buckling.


(a) Specimen HPP


(b) Specimen HAC

Figure 7. Failure mode of test specimen

3.3 Hysteresis Behaviour and Energy Dissipation

The hysteresis behaviour in the lateral load-displacement relationships of specimens HPP and HAP are plotted in Figure 8. The pinching effect is more obvious in specimen HAC than that in specimen HPP. It demonstrates that incorporation of stiffeners on the infill plate is effective in enhancing the seismic performance of SPSWs.

The energy dissipation of the specimens was computed from the area hysteretic loops at each cycle. The decomposition of energy dissipation at the first and second floors is given in Table 3. Energy dissipation of specimen HAC is higher than that in specimen HPP. This is attributed to the failure of specimen HPP being concentrated in the first floor. As a result, the second storey of the structural system seldom contributes to the dissipation of energy. The addition of stiffeners, which divided the thin steel plates, reduced the height-thickness ratio of the infill plates. This is of benefit for resisting lateral loads as well as delaying the buckling of infill plates. It means that the lateral stiffness is enhanced for the specimens and the capability of the two infill plates can be fully used.

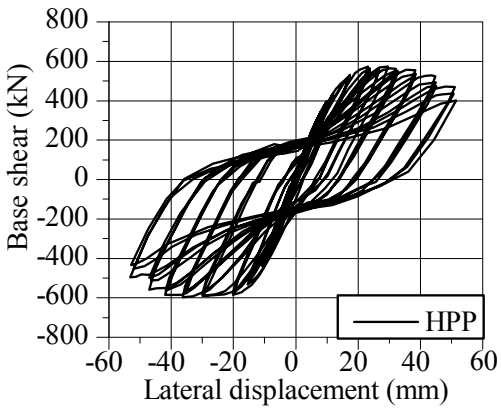

(a) Hysteresis curve of HPP

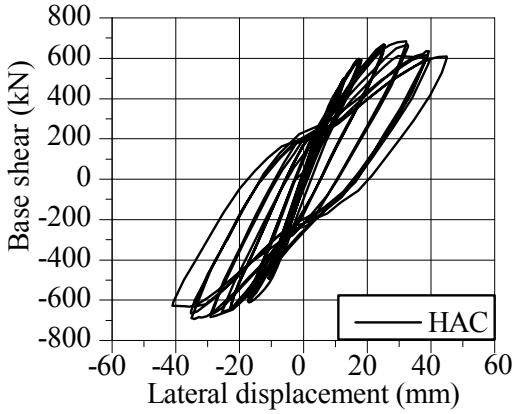

(b) Hysteresis curve of HAC

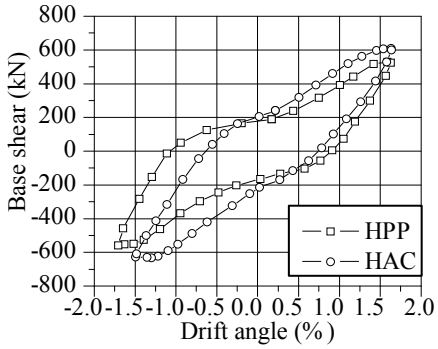

(c) Hysteresis curve of the two specimens at 1.6% drift

Figure 8. Load-displacement Hysteresis Curves

Table 3. Energy Dissipation of Specimens

Loading levels	Specimen HPP			Specimen HAC		
	Entirety	First story	Second story	Entirety	First story	Second story
100kN	50	21	29	49	26	24
400kN	736	368	367	2130	1486	643
$1\delta_y$	1127	492	545	2416	1680	736
$2\delta_y$	723	4526	2714	10263	5611	4652
$3\delta_y$	17915	11969	5909	23711	12885	10826
$3.5\delta_y$	23376	13767	7745	30437	16417	14021
$4\delta_y$	29588	19250	10314	Unit: kN·mm		

3.4 Skeleton Curve

A skeleton curve is a hysteresis curve which is the peak point of the first cycle connected at each loading level. The skeleton curves of specimens HPP and HAC are shown in Figure 9. A summary of test results is given in Table 4. Here, P_y and P_{max} are the yield load and peak load respectively; δ_y is the yield displacement and δ_{max} is defined as the displacement at peak load; δ_u is defined as the displacement when lateral loading decreased to 85% of the peak load; h represents the storey height. Ductility is defined as the ratio of ultimate displacement to yielding displacement, i.e. $\mu=\delta_u/\delta_y$, according to "Specification of Testing Methods for Earthquake Resistant Building (JGJ 101-96)" [28]. As depicted in Figure 10, the yield point (δ_y, P_y) is determined through the concept of equal plastic energy. The area under the idealized elastic-plastic curve was equal to that of the actual pushover curve. The initial stiffness of the two specimens was almost the same. As seen in Table 4, the specimens did not exhibit symmetrical behaviour in the push and pull directions. Stiffness in the push direction was smaller than that in the pull direction. This may be attributed to other influential factors, such as the initial defects and strong column constraints in the loading side.

Installation of the stiffeners increased the stiffness and load carrying capacity of the specimen. Lateral stiffness, yield load, and peak load of the stiffened SPSW were approximately 1.06, 1.05, and 1.18 times that of the non-stiffened SPSW, respectively. The ductility coefficient of the non-stiffened SPSW was about 1.07 times that of the stiffened SPSW. It was illustrated that stiffened SPSWs have a higher lateral load carrying capacity but lower ductility as compared to non-stiffened SPSWs. It is worth noting that the SRSF-SPSW system possessed ductility of above 4.0, which demonstrated a good plastic deformation capacity.

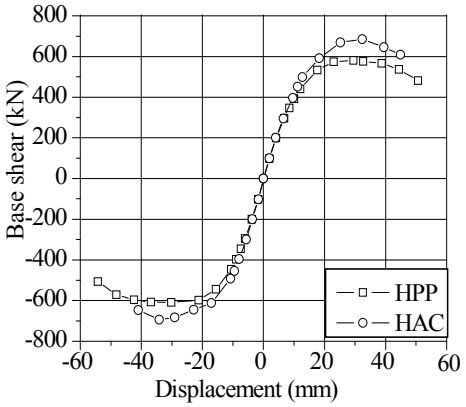

Figure 9. Load-displacement Envelope

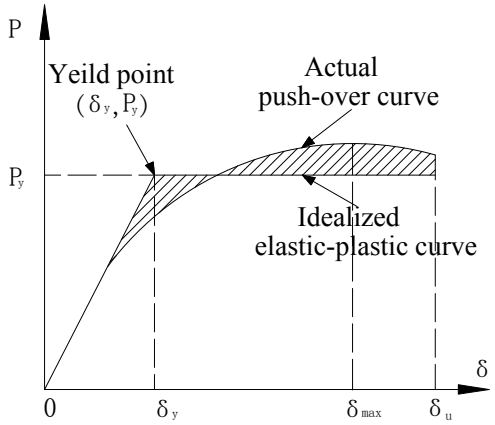

Figure 10. Definition of a Yield Point

Table 4. Summary of Test Results

Specimen		Lateral stiffness	Yielding load			Peaking load			Ultimate displacement		Ductility coefficient
	Direction	P_y/δ_y (kN/mm)	P_y (kN)	δ_y (mm)	δ_y/h	P_m (kN)	δ_{max} (mm)	δ_{max}/h	δ_u (mm)	δ_u/h	μ
HAC	Push(+)	36.00	450.0	12.50	1/220	684.6	29.20	1/93	44.92	1/61	3.60
	Pull(-)	40.08	451.7	11.27	1/244	690.0	35.35	1/77	46.49	1/59	4.12
	Average	37.89	450.9	11.90	1/232	687.3	32.29	1/85	45.71	1/60	3.86
HPP	Push(+)	33.67	428.9	12.74	1/216	574.43	23.15	1/118	51.33	1/54	4.03
	Pull(-)	37.79	434.2	11.49	1/239	596.04	36.37	1/75	52.82	1/52	4.60
	Average	35.61	431.6	12.12	1/227	585.23	29.76	1/92	52.13	1/53	4.32

3.5 Mechanical Analysis of the Semi-rigid Connections

Dial gauges were installed (e.g. BW4, BW5, BW9, BW10, TW2 and TW3) at the end of the beams (as shown in Figure 4) to measure the load-rotation relationship of the beam-column connections. It aimed to investigate the interaction between semi-rigid connections and the SPSW. Based on the Pythagorean theorem, rotation α could be calculated with Equation (1).

$$\alpha = \arccos\left[\frac{2\times 250^2 - (250\sqrt{2} + disp)^2}{2\times 250^2}\right] - \frac{\pi}{2} \tag{1}$$

where, *disp* is the data tested by the dial gauges.

Load-rotation relationships at the ends of intermediate beams in both specimens are shown in Figure 11. In the elastic stage, data measured by two gauges could properly reflect the real condition of the connections. At the level of $1.0\delta_y$, the specimen was partly in plastic and out-of-plane deformation; the gauges at the connection were out of order. However, there was no obvious degradation tendency for the connection stiffness during the test. Development of plastic strain in the infill plates had limited impact on the performance of the connections. Comparing the stiffness degradation of the connections in both specimens, it could be illustrated that stiffness of the specimen HAC was approximately three times that of specimen HPP. Therefore, stiffened SPSWs could reduce the ductility requirement of the connections.

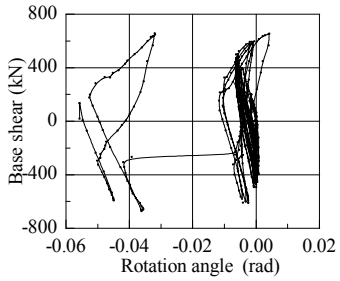

(a) HAC Up east (BW5)

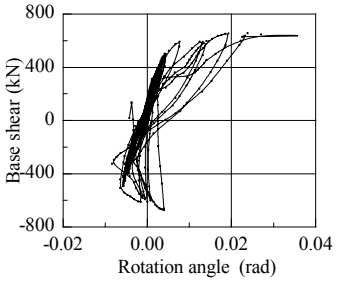

(b) HAC Up west (BW10)

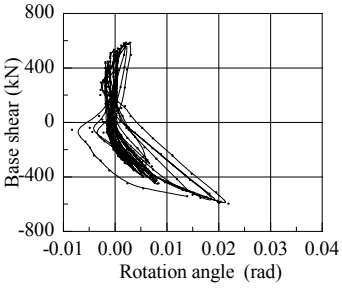

(c) HPP Up east (BW5)

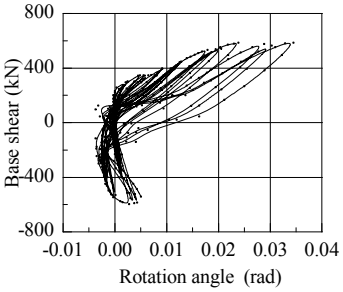

(d) HPP Up west (BW10)

Figure 11. Rotation Versus Load of Intermediate Beam

4. FINITE ELEMENT ANALYSIS

4.1 FE Model

The nonlinear finite element models for tested specimens were built in the ANSYS package. The steel frames, infill plates and stiffeners were modelled using the Shell181 element. As beam-column connections were complex, a rigid plate combined with Combin39 element was adopted. The finite element model of the specimen is illustrated in Figure 12. The model had identical geometry, boundary conditions, material properties and loading sequence as the specimens in the experimental investigation.

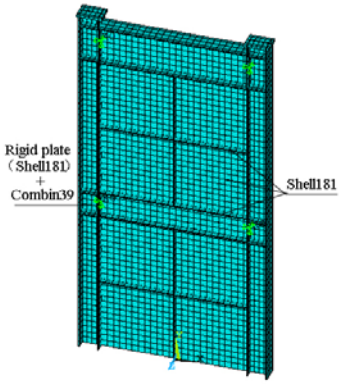

Figure 12. FE Model

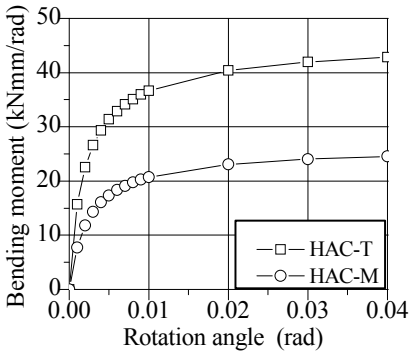

Figure 13. Moment-rotation Relationship

An M-θ relationship is needed for defining parameters of the Combin39 element. In this paper, Kishi-Chen's three-parameter power function model was used to define the nonlinear moment-rotation relationship. This model is a semi-empirical connection model consisting of three parameters: initial stiffness R_{ki}, ultimate moment M_u and shape parameter n. Equation (2) shows Kishi-Chen's model.

$$M = \frac{R_{ki}\theta_r}{[1+(\theta_r / \theta_0)^n]^{1/n}} \tag{2}$$

where θ_0 is the plastic rotation corresponding to the ultimate moment M_u; θ_r is the rotation of the specimen. The moment-rotation relationships of each connection in the specimens are shown in Figure 13.

4.2 Model Validation

Figure 14 shows the simulated hysteretic behaviour of specimen HPP using the FE model. The pinching behaviour of the hysteresis curve in the FE model is smaller than that of the experimental results. Specifically, fluctuation of lateral loading at zero displacement is higher in the FE model as compared with the experimental result. At the elastic-plastic stage, the differences of hysteresis curves between the experiments and Finite Element Analysis became larger. The FE model exhibited a gradual decrease in lateral loading in the inelastic stage of loading. Generally, peak loads achieved in the FE model (i.e. 686.4 kN in push and 696.2 kN in pull) were consistent with those obtained from the experiments (i.e. 684.6 kN in push and 690.0 kN in pull). Figure 15 shows the von Mises stress of specimen HPP at -42 mm displacement. Compared to the failure mode in Figure 7(b), the FE model captures the typical characteristics of the specimen.

The stiffness degradation of the specimens is determined by peaking secant stiffness as specified in section 5.5.3 of the Specifications of Testing Methods for Earthquake Resistant Building (JGJ 101-96). Figure 16 shows the comparison of stiffness degradation obtained from the FE model and experiments. Stiffness in the FE model was higher than that of the experiment at the initial stage of loading (the maximum error was 28%). However, stiffness degradation tended to be the same at the final stage of loading (the error was about 5%). This was mainly attributed to initial defects in the test. It can be explained as follows. (1) The defect distribution of specimens in the test is different from that in the FE model. The FE model only considers the defects of the infill plate, but without the defects of beams, columns and stiffeners. As the FE model is nearly perfect at the initial stage of loading, it has higher load carrying capacity and stiffness. (2) There is an inevitable initial eccentricity for the applied load in the test. As a result, additional bending and torsion caused by initial eccentricity would reduce the load carrying capacity and stiffness of the SPSW. For the FE model, the column exhibits some degrees of out-of-plane deformation at an advanced stage of loading, which reduced the difference between the test results and FE analysis. (3) Constraints in the FE model are greatly idealized compared with the test specimen. It also can enhance the load carrying capacity and stiffness of specimens. In general, the FE model provides reasonable prediction for the tested specimen.

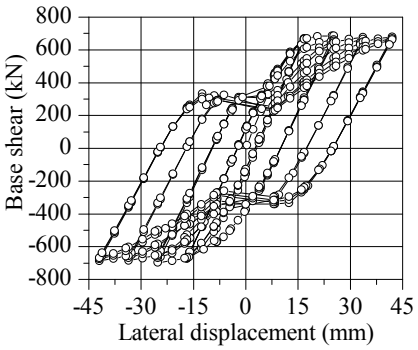

Figure 14. Hysteretic curves of FE

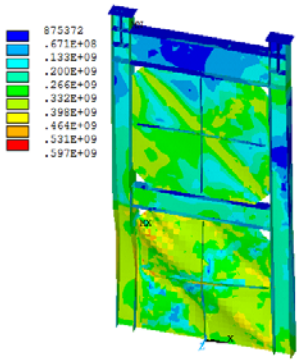

Figure 15. Von Mises Stress at -42mm Displacement

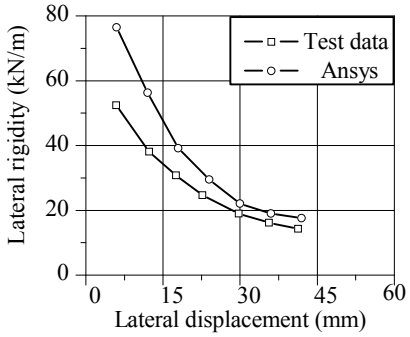

Figure 16. Degeneration of Rigidity

4.3 Parametric Study

A parametric study was performed to assess the influence of connection stiffness and stiffeners stiffness on the performance of the new structural system through FE analysis. The tested specimen was set as the basic model (HAC-B). Seven models were divided into two groups, including HAC-SW series and HAC-PR series. The former investigated the effect of stiffener-panel stiffness ratio while the latter aimed to reveal the effect of connection stiffness. FE analysis was conducted for the specimens under monotonic loading. The axial load ratio was the same as that in the experiment.

4.3.1 Stiffener-panel stiffness ratio (HAC-SW series)

In this series, the stiffener-panel stiffness ratio is defined as the ratio of stiffener with unit width to panel. It aimed to compare the effect of the stiffener-panel stiffness ratio on load carrying capacity, ductility and horizontal shear force distribution. Stiffener-panel stiffness ratios considered for the specimens are given in Table 5.

Table 5. HAC-SW Design Parameter

Specimen	HAC-SW1	HAC-B	HAC-SW2	HAC-SW3
Stiffener-panel stiffness ratio	0	12	40	80

Figure 17 illustrates the load-displacement curves of the specimens in the HAC-SW series. It is obvious that the addition of stiffeners in SPSWs can significantly increase peak load and ductility of SRSFs by comparing HAC-SW1 with the other three specimens. For instance, the peak load of specimen HAC-B increased by 14% compared with that of specimen HAC-SW1. For SPSW with stiffeners, increasing stiffener-panel stiffness ratio led to a slight enhancement of peak load. The peak load of specimen HAC-SW3 was enhanced by about 3% when compared with specimen HAC-B. This is attributed to the fact that the stiffeners could restrain out-of-plane deformation of the infill plates efficiently with a certain degree of stiffness. Therefore, continuous increasing of stiffness of the stiffeners could only produce a limited increase to the constraints of SPSW. Considering economic requirements, a stiffener-panel stiffness ratio of 40 is recommended in this paper.

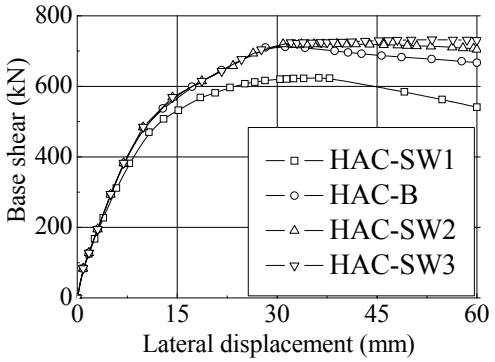

Figure 17. Load-displacement Envelopes of Specimens in HAC-SW

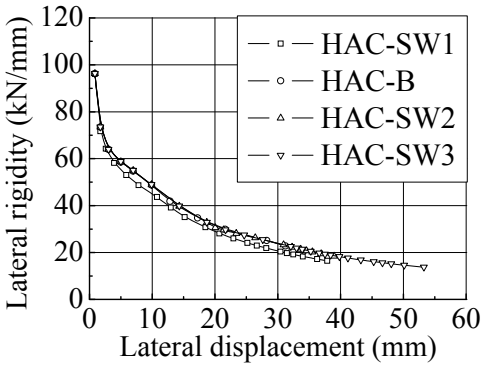

Figure 18. Stiffness Degradation of Specimens in HAC-SW

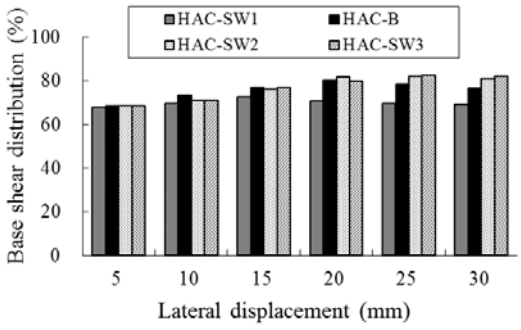

Figure 19. HAC-SW Force Distribution Comparison

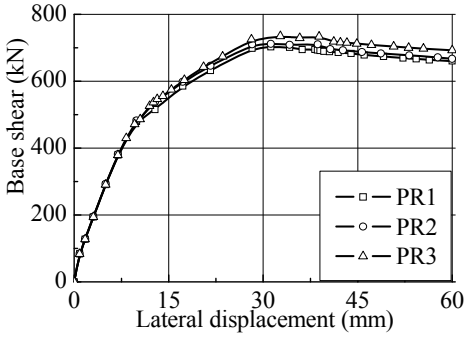

Figure 20. HAC-PR Load-displacement Envelope

Figure 18 shows the stiffness degradation of the specimens in the HAC-SW series. Force distribution curves of specimens in the HAC-SW series are illustrated in Figure 19. It can be seen that all specimens have similar stiffness degradation through the numerical simulation. At the initial stage of loading, the infill plates made a primary contribution to the lateral shear force plates and this effect was basically identical for the four specimens. It demonstrates that the infill plates are efficient in resisting lateral force at the initial stage of loading. At that time, the infill plates did not buckle and the role of the stiffeners was unobvious. However, the stiffness and the distributed shear force of the non-stiffened SPSW were lower than those of the stiffened SPSW after buckling of the infill plates as lateral displacement increased. Lateral loads were mainly resisted by two portions including the steel frame and connections between the fish plates and the infill plates. Load taken by the frame was limited due to the semi-rigid connections weakening the overall stiffness of the structure. After buckling of the infill plates, stiffeners reduced the load taken by the frame which is beneficial for the requirement of double-protection measures. It has demonstrated that SPSW in the proposed structural system undertakes 70%-80% of overall lateral load.

4.3.2 Connection stiffness (PR series)

FE analysis of the PR series aimed to investigate the effect of connection rotational stiffness on the behaviour of SRSF-SPSW. It was achieved through adjusting the bending capacity of the connections. The parameters of the connections are summarized in Table 6.

Table 6. HAC-PR Design Parameter

Specimen number	Connections	PR1	PR2	PR3
Bending capacity of connections	HAC-T	$0.20M_p$	$0.40M_p$	infinite
	HAC-M	$0.20M_p$	$0.56M_p$	infinite

Figure 20 shows the load-displacement curves of specimens in the HAC-PR series. All specimens with different connection stiffness had similar responses in terms of peak lateral load and stiffness. In the plastic stage, increasing connection stiffness enhanced the peak lateral load of the specimens. However, the magnitude of the increase ratio was not significant. The peak load of specimen HAC-PR2 increased by 5% as compared with that of specimen HAC-PR1. Therefore, the influence of beam-column connections on lateral load capacity is limited. This is mainly attributed to the large flexibility factor of the column. For a definition of flexibility factor ω_t of a column one can refer to Qu and Bruneau [8]. It also specifies that the ω_t is no larger than 2.5. In this study, the flexibility factor of specimens HAC and HPP were equal to 2.69 which is larger than 2.5. As shown in Figure 7(a), W-column and E-column show obvious curved concave deformation.

In order to further study the influence of the beam-column connection characteristics on the behaviour of the SRSF-SPSW system, the first storey of specimen HAC was modelled as shown in Figure 21(a). It can be equivalent to the model shown in Figure 21(b). The size of SPSW was L×H (L is the height of model, H is the width of model and the base size is 1200 mm×1200 mm). The bottom of the column was hinged to the foundation. A beam is considered as a rigid beam by using the method of DOF coupling, thereby removing the influence of the flexible boundary beam. In order to improve the efficiency of analysis, the Beam188 element was used to simulate the boundary members while the Shell181 element was adopted to simulate the infill plate. Using the ideal elastic-plastic model as stress-strain curve, setting the yield strength of steel as 235 N/mm^2, the modulus of elasticity as 2.1×10^5 N/mm^2 and 0.1% of the out-of-plane buckling deformation as the initial imperfection of model specimen, the finite element specimen is shown in Figure 21(c).

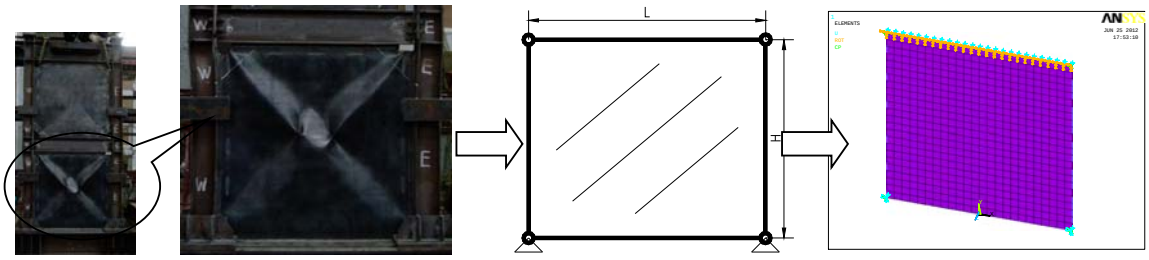

(a) (b) (c)

Figure 21. Establishment of Finite Element Model

The relationship between the stress uniformity ratio $\gamma = S_{average}/S_{max}$ and the flexibility factor (i.e., ω_t) is shown in Figure 22. Where $S_{average}$ is average of the infill plates tension force components parallel with the beam; S_{max} is maximum of the web tension force components parallel with the beam. As shown on that curve, for smaller values of ω_t (e.g., in the range $0 \leqslant \omega_t \leqslant 1$), for which the SPSW have relatively stiff columns, the stress uniformity ratio approximately equals 1 (which physically means that the maximum stress is close to the average stress), indicating development of a uniform infill plates tension field. However, with increases in the flexibility factor, the stress uniformity ratio decreases, indicating formation of a less uniform infill plates tension field in SPSW having more flexible columns.

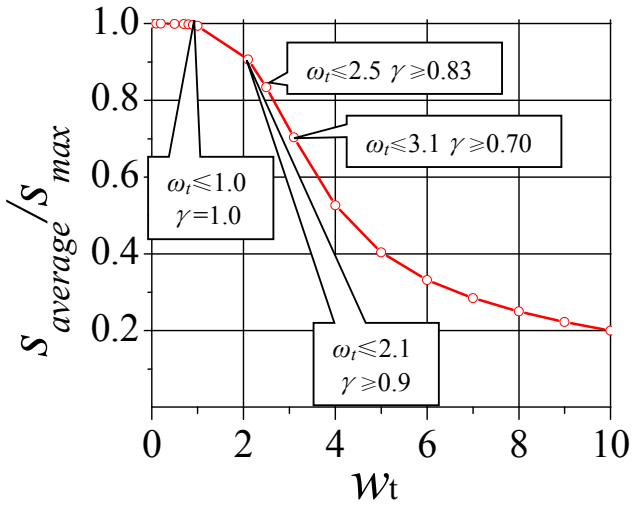

Figure 22. Relationship between $S_{average}/S_{max}$ and ω_t

The main influencing factors on the load carrying capacity of the tested specimen are column flexibility and ratio of SPSW height to thickness. This study set the ratio of height to thickness at 100, 200, and 400, and the column flexibility ω_t as 1.0, 2.1, 2.5, and 3.1, which respectively correspond to 1.00, 0.90, 0.83, and 0.70, setting four levels of stress uniformity coefficient γ as shown in Figure 22. The orthogonal test table is summarized in Table 7.

Table 7. The Orthogonal Test Table

Factors			Specimen number		
Column flexibility	C1	1.0	C1-W1	C1-W2	C1-W3
	C2	2.1	C2-W1	C2-W2	C2-W3
	C3	2.5	C3-W1	C3-W2	C3-W3
	C4	3.1	C4-W1	C4-W2	C4-W3
Ratio of height to thickness （H/t_w）			100 W1	200 W2	400 W3

Peak lateral loads of specimens could be obtained by calculating the conditions of different column flexibility and SPSW height to thickness ratio as shown in Table 8. Theoretical shear strength of the infill plates (the infill plates under complete shear mechanism) can be computed by $V_{pu}=f_v t_w L$. Based on these, this paper compares the enhancement effect, of different connection types, i.e., super action of frame, which could greatly influence the column flexibility, in the following paragraphs.

Table 8 compares the load carrying capacities of specimens with different connection stiffness. Generally, the load carrying capacity of a specimen increases as the stiffness of connections increases. Also, the influence of connection stiffness on load carrying capacity is related to the stiffness of column and thickness of the infill plate. This influence is enlarged when increasing the stiffness of the column and reducing the thickness of the infill plate. As a result, the load carrying capacity of a specimen with a strong column-weak plate is highly affected by connection stiffness. Among all the specimens, specimen C1-W3 exhibited the maximum response to connection stiffness. Specifically, the load carrying capacity of specimen C1-W3 increased by 42.2% when the connection was changed from pin to rigid. The load carrying capacity of specimen C1-W3 with rigid connection was 13.8% higher than that of specimens with semi-rigid connections. For the specimens with a flexibility coefficient of column of 2.5 (e.g. for series C3), the load carrying capacity was enhanced by about 10% when changing pinned connections to rigid connections. The load carrying capacity of specimens with semi-rigid connections was 3.0% higher than that of specimens with rigid connections. When replacing pinned connections with rigid connections for the specimens with the columns which flexibility coefficient is 2.1 (e.g. in series C2), the load carrying capacity increased by 23.5%. The load carrying capacity of specimens with semi-rigid connections was similar to that of specimens with rigid connections. Due to the super action of frames in SRSF-SPSW, the load carrying capacity of specimens with semi-rigid connections was higher than the shear strength of the infill plate. Thus, SRSF-SPSW can be designed according to the shear strength of the infill plate while super action is considered as a safety factor. Specimens in series C-RP were stiffened by specimen HAC-SW2. Table 8 only shows the results of specimens in series W3. Due to the stiffening effect of the infill plate, the influence of connection stiffness on load carrying capacity decreased for the specimens in series C-PR. The load carrying capacity of specimens with rigid connections was about 30% higher than that with pinned connections and about 8% higher than those with semi-rigid connections. This indicates that stiffeners prevent the buckling of infill plates, which weakens the adverse influence of flexible connection on the frame load carrying capacity.

Table 9 compares the relationship between the shear distributions of the infill plate with different types of connections. For the specimens with ratio of height to thickness of 400 (e.g. series W3), shear forces taken by infill walls were almost the same regardless of the flexibility of column and connection stiffness. With the increase of beam-column connection rotational stiffness, the load carrying capacity of the steel frame is slightly increased. For the unstiffened thin SPSW (e.g. for series P-PR), shear force taken by infill plates is seldom affected by connection stiffness when the flexibility of columns is no larger than 2.5. When the column is relatively flexible, connection stiffness has a certain influence on the shear force taken by infill plates. For the stiffened thin SPSW (e.g. for series C-PR), shear forces taken by infill plates are almost the same, around 460 kN. However, shear forces taken by the whole system increase as connection stiffness increases. It indicates that forces taken by columns is proportional to the connection stiffness increases. Meanwhile, setting the stiffener could improve the tension field for shear resistance. Shear force taken by infill plates in the C-PR series specimens was close to the shear resistant capacity V_{pu} of the infill plates under complete shear as shown in Table 8. There is a significant “lining” effect in the corner of the stiffened steel plates and thick plates, which strengthens the beam-column connections. Thus, even if a simple beam-column connection is used in a steel frame, it could

contribute to resist bending. Because the effect improvement is limited, it could be considered as a factor of safety.

Table 8. ANSYS Load Carrying Capacity Calculation (unit: kN)

Category	Specimen	PR 1	PR 2	PR 3	PR3 /PR1	PR2 /PR1	PR3 /PR2	Vpu	PR1 / Vpu	PR2 / Vpu	PR3 / Vpu
P-PR	C1-W1	1975.5	2002.7	2117.8	1.072	1.014	1.057	1952.5	1.012	1.026	1.085
	C1-W2	930.64	1027.1	1078.9	1.159	1.104	1.050	976.28	0.953	1.052	1.105
	C1-W3	464.89	581.00	660.94	1.422	1.250	1.138	488.14	0.952	1.190	1.354
	C2-W1	1972.6	1998.0	2097.53	1.063	1.013	1.050	1952.5	1.010	1.023	1.074
	C2-W2	906.94	1010.6	1024.73	1.130	1.114	1.014	976.28	0.929	1.035	1.050
	C2-W3	462.80	558.74	571.50	1.235	1.207	1.023	488.14	0.948	1.145	1.171
	C3-W1	1967.22	1992.4	2052.2	1.043	1.013	1.030	1952.5	1.008	1.020	1.051
	C3-W2	882.38	955.76	970.44	1.100	1.083	1.015	976.28	0.904	0.979	0.994
	C3-W3	454.46	489.67	490.07	1.078	1.077	1.001	488.14	0.931	1.003	1.004
	C4-W1	1959.87	1973.97	1988.96	1.015	1.007	1.008	1952.5	1.004	1.011	1.019
	C4-W2	812.97	846.35	857.43	1.055	1.041	1.013	976.28	0.833	0.867	0.878
	C4-W3	405.91	421.74	420.69	1.036	1.039	0.998	488.14	0.832	0.864	0.862
C-PR	C1-W3	499.25	615.81	665.05	1.332	1.233	1.080	488.14	1.023	1.262	1.362
	C2-W3	496.91	599.65	618.87	1.245	1.207	1.032	488.14	1.018	1.228	1.268
	C3-W3	495.04	547.59	550.70	1.112	1.106	1.006	488.14	1.014	1.122	1.128
	C4-W3	486.55	499.56	500.43	1.029	1.027	1.002	488.14	0.997	1.023	1.025

Note: P and C halves are SPSW with and without stiffeners, respectively.

Table 9 The shear distribution of infill plate (unit: kN)

Category	Specimen	PR1			PR2			PR3		
		V_p	V	V_p/V	V_p	V	V_p/V	V_p	V	V_p/V
P-PR	C1-W3	437.01	464.89	0.940	437.06	581.00	0.752	436.87	660.94	0.661
	C2-W1	1861.10	1972.63	0.948	1867.60	1998.05	0.935	1870.60	2097.53	0.887
	C2-W2	865.94	906.94	0.962	872.81	1010.69	0.865	874.34	1024.73	0.845
	C2-W3	429.22	462.80	0.937	432.70	558.74	0.774	433.85	571.50	0.751
	C3-W3	422.21	454.46	0.932	423.08	489.67	0.864	423.50	490.07	0.862
	C4-W3	395.91	405.91	0.975	405.38	421.74	0.961	405.44	420.69	0.963
C-PR	C1-W3	463.32	499.25	0.928	463.36	615.81	0.752	463.40	665.05	0.696
	C2-W3	462.34	496.91	0.930	462.42	599.65	0.771	462.88	618.87	0.748
	C3-W3	461.54	495.04	0.932	461.52	547.59	0.843	461.90	550.70	0.839
	C4-W3	461.25	486.55	0.948	461.3	499.56	0.923	461.6	500.43	0.920

For specimens with the same columns and infill plates but with limited flexibility factor (e.g. series C1, C2 and C3), the load carrying capacity of the structural system increases as connection stiffness increases under various flexibility factors. It indicates that enhancement of the load carrying capacity of the structural system results from increasing connection characteristics. Thus, connection characteristics could significantly influence the shear force taken by the frame. This means that the improvement of the structural load carrying capacity results from the contribution of the frame, which forms the second defence line for earthquake-resistant building.

5. CONCLUSIONS

This paper introduces a new type of structural system consisting of SRSF-SPSW. The seismic behaviour of this new structural system was estimated through experimental study and finite element analysis. Based on experimental results and parametric study, the following conclusions can be drawn.

(1) Setting of crossed stiffeners in SPSW with a stiffener-panel stiffness ratio of 12 increases stiffness, ductility, and peak lateral load of SRSF-SPSW by 6%, 17%, and 18%, respectively. It is attributed to the stiffeners reducing the height-thickness ratio of the plates, which improves the loading condition of the infill plates as well as delaying the buckling of steel panels.
(2) Incorporating stiffeners in SPSW increases the buckling load of thin steel plates due to its restraining effect in out-of-plane deformation. The stiffeners also reduce the concavity of columns, which leads to uniform distribution of forces between two floors.
(3) The use of thick SPSWs can be avoided through proper stiffener setting. Increasing the stiffness of the stiffeners can enhance the initial stiffness and peak lateral load of SRSF-SPSW and improve the overall behaviour of the specimen. The stiffener-panel stiffness ratio is recommended to be around 40.
(4) The influence of connection stiffness on the load carrying capacity of the structural system is related to the stiffness of columns and thickness of infill plates. This influence is enlarged with increasing stiffness of columns and reducing thickness of infill plates. The load carrying capacity of a structural system with strong column-weak plate is significantly affected by connection stiffness and is increased by 42.2% when the connection is changed from pinned to rigid. For structural systems with weak columns (e.g. flexibility coefficient of columns is smaller than 2.5), the load carrying capacity is enhanced by less than 10% when changing pinned connections to rigid connections.

ACKNOWLEDGMENTS

The authors are grateful to the financial support from NSF (Project No: 51408461). The authors would like to thank the technical assistance provided by Structural Engineering Research Laboratory at Xi'an University of Architecture and Technology.

REFERENCES

[1] Thorburn, L.J., Kulak, G.L. and Montgomery, C.J., "Analysis of Steel Plate Shear Walls", Structural Engineering Report.No.107. Department of Civil Engineering, University of Alberta, Canada, 1983.
[2] Lubell, A.S. and Prion, H.G.L., "Unstiffened Steel Plate Shear Walls Performance Under Cyclic Load", Journal of Structural Engineering, 1983, Vol. 126, No. 4, pp. 453-460.
[3] Chen, G.D. and Guo, Y.L., "An Cyclic Test of Steel Plate Shear Walls", Journal of Building Structures, 2004, Vol. 25, No. 2, pp. 19-26 (in Chinese).
[4] Wang, Y.C., "Experiment and Theory Study of Bearing Capacity of Steel Plate Shear Walls on compound load action", PhD, Xi'an University of Architecture & Technology, 2011 (in Chinese).
[5] Lin, Y.C. and Tsai, K.C., "Seismic Responses of Steel Plate Shear Walls Constructed with Restrainer" Report NCREE-04-015, National Center for Research on Earthquake engineering, Taipei, Taiwan, R.O.C., (in Chinese).
[6] Park, H., Kwack, J., Jeon, S., Kim, W. and Choi, I., "Framed Steel Plate Wall Behavior under Cyclic Lateral Loading", Journal of Structural Engineering, ASCE, 2007, Vol. 133, No. 3, pp. 378-388.
[7] Tsai, K.C. and Li, C.H., "Cyclic Tests of Four Two-storey Narrow Steel Plate Shear Walls-Part 1 Analytical Studies and Specimen Design", Earthquake Engineering & Structural Dynamics, 2010, Vol. 39, pp. 775-799.

[8] Qu, B. and Bruneau, M., "Testing of Full-scale Two-storey Steel Plate Shear Wall with Reduced Beam Section Connections and Composite Floors", Journal of Structural Engineering, ASCE, 2008, Vol. 134, No. 3, pp. 364-373.
[9] Habashi, H.R. and Alinia, M.M., "Characteristics of the Wall-frame Interaction in Steel Plate Shear Walls." Journal of Constructional Steel Research, 2010, Vol. 66, No. 2, pp. 150-158.
[10] Kurata, M., Leon, R.T., Desroches, R. and Nakashima, M., "Steel Plate Shear Wall with Tension-bracing for Seismic Rehabilitation of Steel Frames", Journal of Constructional Steel Research, 2012, Vol. 71, pp. 92-103.
[11] Zhang, X.Q. and Guo, Y.L., "Behavior of Steel Plate Shear Walls with Pre-compression Adjacent Frame Columns", Thin-Walled Structures, 2014, Vol. 77, pp. 17-25.
[12] Bhowmick, A.K., Grondin, G.Y. and Driver, R.G., "Nonlinear Seismic Analysis of Perforated Steel Plate Shear Walls", Journal of Constructional Steel Research, 2014, Vol. 94, pp. 103-113.
[13] Alinia, M.M. and Dastfan, M., "Cyclic Behaviour, Deformability and Rigidity of Stiffened Steel Shear Panels", Journal of Constructional Steel Research, 2007, Vol. 63, No. 4, pp. 554–563.
[14] Alavi, E. and Nateghi, F., "Experimental Study on Diagonally Stiffened Steel Plate Shear Walls with Central Perforation", Journal of Constructional Steel Research, 2013, Vol. 89, pp. 9-20.
[15] Nie, J.G., Zhu, L., Fan, J.S. and Mo, Y.L., "Lateral Resistance Capacity of Stiffened Steel Plate Shear Walls", Thin-Walled Structures, 2013, Vol. 67, No. 3, pp. 155-167.
[16] Azizinamini, A. and Radziminski, J.B., "Static and Cyclic Performance of Semi-rigid Steel Beam-column Connections", Journal of Structural Engineering, ASCE, 1989, Vol. 115, No. 12, pp. 2979-2999.
[17] Elnashai, A.S. and Elghazouli, A.Y., "Seismic Behavior of Semirigid Steel Frames", Journal of Constructional Steel Research, 1994, Vol. 29, No. 1, pp. 149-174.
[18] Kishi, N., Chen, W.F. and Goto, Y., "Effective Length Factor of Columns in Semi-rigid and Unbraced Frames", Journal of Structural Engineering, ASCE, 1997, Vol. 123, No. 3, pp. 313-320.
[19] Bernuzzi, C., Zandonini, R. and Zanon, P., "Experimental Analysis and Modeling of Semi-rigid', 1996, Vol. 38, No. 2, pp. 95-123.
[20] Yu, J.G., Hao, J.P., Zhang, W.Q., Zhong, W.H. and Xie, Q., "Stability Analysis for Semi-rigid Jointed and Braced Steel Frames", World Earthquake Engineering, 2010, Vol. 26, No. 3, pp. 101-108 (in Chinese).
[21] Xie, Q., Hao, J.P. and Yu, J.G., "Study on Semi-rigid Frame with Steel Palte Shear Wall", Beijing, Proceeding of the Eleventh International Symposium on Structural Engineering, 2010, pp. 1917-1923.
[22] Caccese, V., Elgaaly, M. and Chen, R., "Experimental Study of Thin Steel-Plate Shear Walls Under Cyclic Load", Journal of Structural Engineering, 1993, Vol. 119, No. 2, pp. 573-587.
[23] Kulak, C.L., Laurte Kennedy, D.J. and Driver, R.G., "Discussion of Experimental Study on Thin Steel Plate Shear Watts under Cyclic Load by Caccese, V., Elgaaly, M., and Chen, R.", Journal of Structural Engineering, 1994, Vol. 120, No.10, pp. 3072-3073.
[24] Xie, M., "Behavior of Steel Shear Wall Panels and Frame-Wall Systems", Bethlehem, Pennsylvania, Lehigh University, 1995.
[25] Alinia, M.M. and Dastfan, M., "Behaviour of Thin Steel Plate Shear Walls Regarding frame Members ", Journal of Constructional Steel research, 2006, Vol. 62, No. 7, pp. 730–738.

[26] GB/T228-2002, “Metallic Materials-Tensile Testing at Ambient Temperature”, 2009, Beijing, China Standard Press (in Chinese).
[27] GB/T 2975-1998, “Steel and Steel Products-Location and Preparation of Test Pieces for Mechanical Testing”, 2009, Beijing, China Standard Press (in Chinese).
[28] JGJ 101-96, “Specification of Testing Methods for Earthquake Resistant Building”, 1997, Beijing, China Architecture and Building Press (in Chinese).

AXIAL FORCE AND DEFORMATION OF A RESTRAINED STEEL BEAM IN FIRE

Description and validation of a simplified analytical procedure

Naveed Iqbal [1,*], Tim Heistermann [1], Milan Veljkovic [1], Fernanda Lopes [2], Aldina Santiago [2] and Luis Simões da Silva [2]

[1] Luleå University of Technology, Division of Structural and Construction Engineering, Luleå, Sweden
[2] University of Coimbra, Department of Civil Engineering, Coimbra, Portugal
(Corresponding author: E-mail: naveed.iqbal@ltu.se)

Received: 17 February 2015; Revised: 7 May 2015; Accepted: 28 July 2015

ABSTRACT: Structural fire design is exceedingly adopting the performance based approach. There are evident advantages of this approach compared to the prescriptive methods from codes. An analytical procedure, based on the real performance, must accurately predict the beam behaviour in fire. The study presented here proposes one such simplified analytical procedure aim to predict the real behaviour of a restrained steel beam. The proposed analytical procedure is validated through FE Analysis using FE models validated through test results. The study also attempts to establish the importance of using semi-rigid connection strength with respect to accurately predicting the behaviour of the restrained beam at catenary stage.

Keywords: Structural fire design, performance based design, Abaqus, fire tests, simplified design procedure, catenary action

DOI: 10.18057/IJASC.2016.12.2.6

1. INTRODUCTION

The prescriptive design approach in fire from design codes requires each structural component to fulfil their design requirement in isolation. This approach overlooks the interaction between different structural components in fire situations that might be unfavourable in some and favourable in other cases. Advanced numerical modelling tools have enabled the application of the performance base approach for design of structures in fire. Based on sound engineering principles and calculations, complex structural systems such as composite structures can be analysed with such tools. Contrary to the prescriptive approach, performance based design is more complex and its application is relatively case specific.

The World Trade Centre (WTC) towers collapses have shown how damaging the interaction between different structural members can be in fire [1]. Other examples such as the full scale building tests conducted by the Building Research Establishment (BRE) at Cardington have led to useful data regarding redundant structural systems in fire [2].

The focus of this study is the analysis of the behaviour of a restrained steel beam in fire. The restrained behaviour of a steel beam in fire has also been previously studied by other researchers. Liu et al tested a sub-frame in fire using two different types of connections: flush end plate and web-cleat connections [3]. Yin and Wang investigated the effect of axial and rotational stiffness on a restrained steel beam in a sub-frame exposed to fire [4]. They further developed an analytical procedure to describe the behaviour of a restrained steel beam in fire. The procedure was validated using FE modelling [5], [6]. Li and Guo [7] also included the cooling phase in their study to assess the tensile forces produced as a result. Santiago et al [8] focused on the role of end restraints on a steel beam in a sub-frame exposed to natural fire conditions (heating and cooling phases). Gillie

used a benchmark study to demonstrate the complexity of the behaviour of a restrained steel beam at elevated temperatures compared to the assumption of an isolated member in standard fire tests [9].

2. ANALYTICAL PROCEDURE

2.1 Introduction

Figure 1 shows the axial force-vs-temperature curve of the beam. Under fire exposure the beam is initially compressed due restrained expansion. Later as the beam is heated further, the material strength and stiffness is considerable reduced causing the beam to deflect and release the initial compression and transition into the tensile phase. The beam at this stage behaves like a catenary resisting part of the applied load. An analytical procedure should enable the designer to predict the level of the axial force and deflection of the beam during fire exposure.

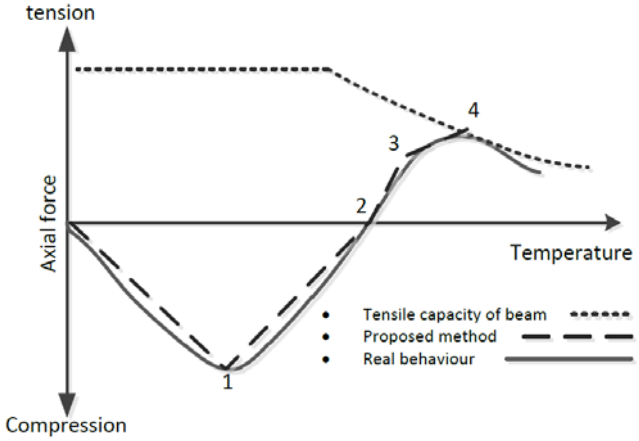

Figure 1. General Variation of the Axial Force in a Restrained Steel Beam in Fire

The procedure presented here is based on a concept presented by Wang et al. [10]. The original method proposes calculating three transition points on the axial force-vs-temperature curve. These points are the maximum compressive force (1), zero axial force (2) and maximum tensile force (4) (Figure 1). These points are joined together by straight lines to get the approximate axial force-vs-temperature curve.

2.2 Proposed Novel Approach

To obtain a better approximation of the curve, the proposed procedure has four transition points instead, which are calculated and then joined together forming the broken line in Figure 1. This approach provides a comparatively better approximation of the axial force vs temperature relationship of the beam due to its extra transition point 3 and consideration of the residual bending moment resistance from point 2 to point 3. The details of the procedure are described as follows.

2.2.1 Maximum compressive force

The first transition point (1) on the axial force vs. temperature curve of a restrained steel beam is the maximum compressive force developed due to the beams' restrained thermal expansion. The maximum compressive force is determined by considering its interaction to the bending moment produced by the imposed loading on the beam. The interaction equation from Eurocode 3 part 1-2 has been considered in the analytical procedure presented here [11]. Increasing temperature will reduce the modulus of elasticity and yield strength of steel, which implies that an iterative

procedure will be adopted to calculate the maximum compressive force and the temperature at which it will be achieved. Figure 2 shows a schematic diagram of the procedure used for this purpose.

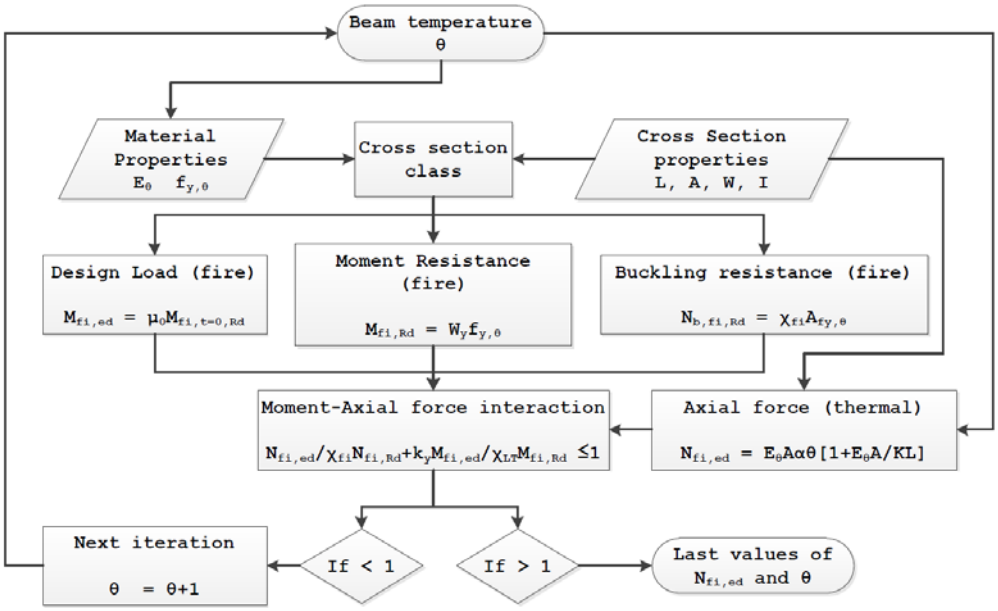

Figure 2. Schematic Diagram of the Calculation of Maximum Compressive Force

The assumptions considered in the calculation shown in Figure 2 are as follows:

- Axial force in the beam is calculated from the equation taken from Usmani et al. [12]:

$$N_{fi,Ed} = E_\theta A \alpha \Delta T \left[1 + \frac{E_\theta A}{KL}\right] \tag{2.1}$$

- The stiffness 'K' in Eq. 2.1 above is the stiffness of the supporting.
- The deflection of the beam is assumed to be elastic during this initial phase.
- The beam is assumed to be restrained from lateral torsional buckling.

2.2.2 Zero axial force

The first phase of the axial force-temperature curve concludes at point (1). As the temperature increases, further the compressive force in the beam reduces until it becomes zero, i.e. point (2) on the curve shown in Figure 1. From equilibrium, the imposed load is resisted only through flexural bending resistance up to point (2). At this point, the bending moment resistance of the beam is exactly equal to the bending moment from the imposed loading.

The temperature at point (2) is determined from the yield strength of the steel using condition of equality between the moment resistance and the imposed loads as shown in Figure 3.

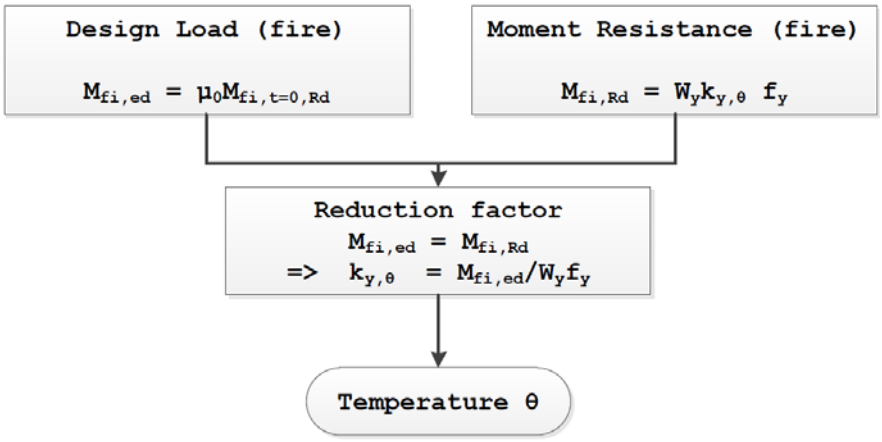

Figure 3. Limiting Temperature for the Bending Moment Resistance of the Beam

The calculation shown in Figure 3 is based on following assumptions:

- The bending moment resistance of the beam is directly proportional to the yield strength of the steel material, disregarding lateral torsional instability.
- The beam is assumed to be simply supported.

The temperature at point (2) corresponds to the conventional limiting temperature of a steel beam according to Eurocode 3 part 1-2.

If a semi-rigid connection is considered, then its strength and stiffness must be used. These will vary with increasing temperature, which must be taken into account. The Initial stiffness and strength of the connection are directly proportional to the modulus reduction factor $k_{E,\theta}$ and the yield strength reduction factor $k_{y,\theta}$, respectively, according to EN 1993-1-2 [11].

A modified procedure is thus used to calculate point (2), described in Figure 5. This procedure would also introduce the connection temperature into the calculation. Generally, the beam temperature at midspan is higher than the connection temperature due to the concentration of mass at the connection. An equation from Annex D of EN 1993-1-2 has been used here to determine the connection temperature shown below as Eq. 2.2 [11].

$$\theta_{conn} = 0.88 \cdot \theta_{beam} \left[1 - 0.3\left(h / D\right)\right] \tag{2.2}$$

The temperature of an unprotected steel beam subjected to a standard fire (ISO 834) is determined using Eq. 2.3 below, from EN 1993-1-2 [11].

$$\Delta\theta_{beam} = k_{sh} \frac{A_m / V}{c_a \rho_a} \dot{h}_{net} \Delta t \tag{2.3}$$

The steel beam with an IPE 300 profile and the connection temperature with increasing time, when uniformly exposed to a standard ISO 834 fire, is shown in Figure 4.

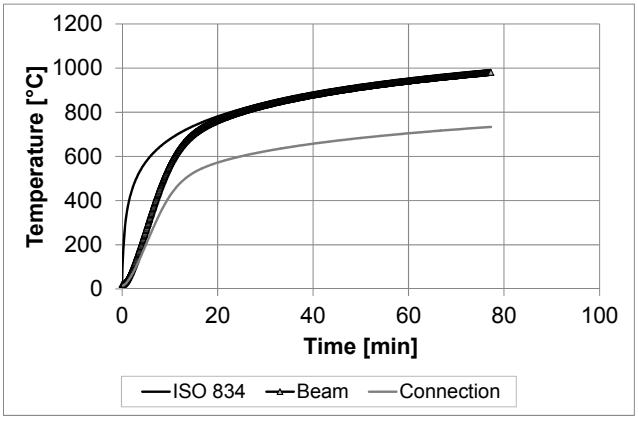

Figure 4. Temperature-vs-time Curves

As a first approximation, the reduction factor $k_{y,conn}$ is calculated using the beam temperature at point (2) according to Figure 3. This value of $k_{y,conn}$ is the starting value in the loop shown in Figure 5. Once the loop gives repeating values of $k_{y,conn}$, it is terminated and the last value of beam temperature in the loop is taken as point (2) on the curve.

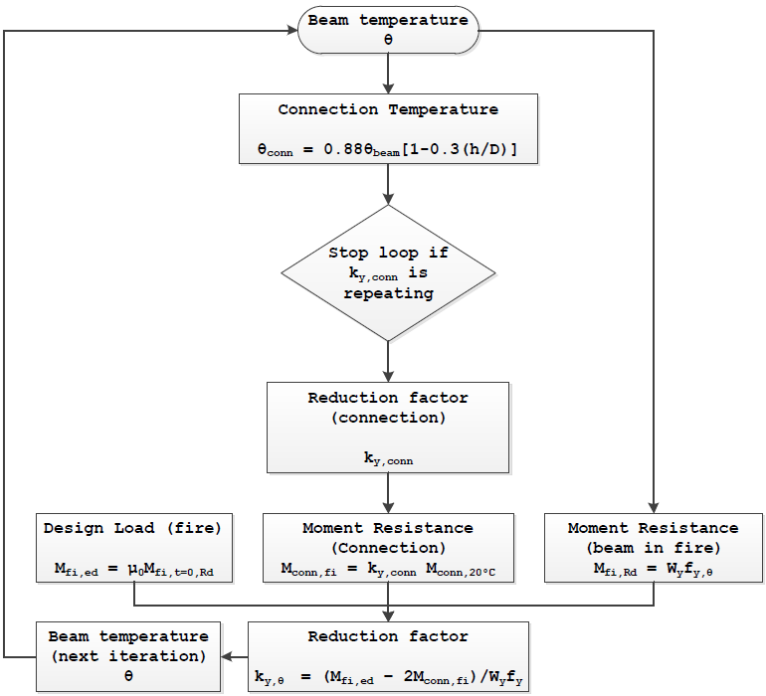

Figure 5. Calculation of the Reduction Factor for the Connection

The midspan deflection of the beam at this point is calculated using the deflection profile proposed by Dwaikat and Kodur, described in Figure 6 [13].

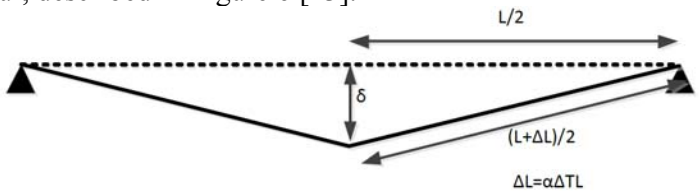

Figure 6. Deflection Profile of the Beam during Catenary Phase

2.2.3 Maximum tensile force

As the temperature increases beyond point (2) calculated above, it is evident that the bending moment resistance of the beam is insufficient to resist the imposed loading. A simply supported beam would undergo runaway deflection at this point. However, a restrained beam would develop an additional resistance through the tensile axial force in the beam resisted at the supports through a catenary action. The bending moment resistance of the beam will progressively decrease with corresponding increase in catenary action as the temperature increases. The limit to the catenary action in the beam is imposed by the beams tensile capacity.

The midspan deflection of the beam in the catenary phase is also calculated using Eq. 2.4 based on profile in Figure 6.

$$\delta = \sqrt{\left[\frac{L+\alpha\Delta TL}{2}\right]^2 - \left[\frac{L}{2}\right]^2} \tag{2.4}$$

The catenary phase can be divided into two distinct phases, i.e. without interaction between catenary force and residual bending moment and with interaction between them.

The boundary between these two phases is at point (3) in Figure 1, determined by calculating the axial force and bending moment resistance for each temperature increment beyond point (2) on the curve. The criteria for no interaction between the axial force and bending moment is checked at each increment and continued if satisfied. The last increment that satisfies this condition is the point from which onwards the catenary force will interact with the bending moment resistance. This calculation procedure can be easily understood through the schematic diagram of Figure 7.

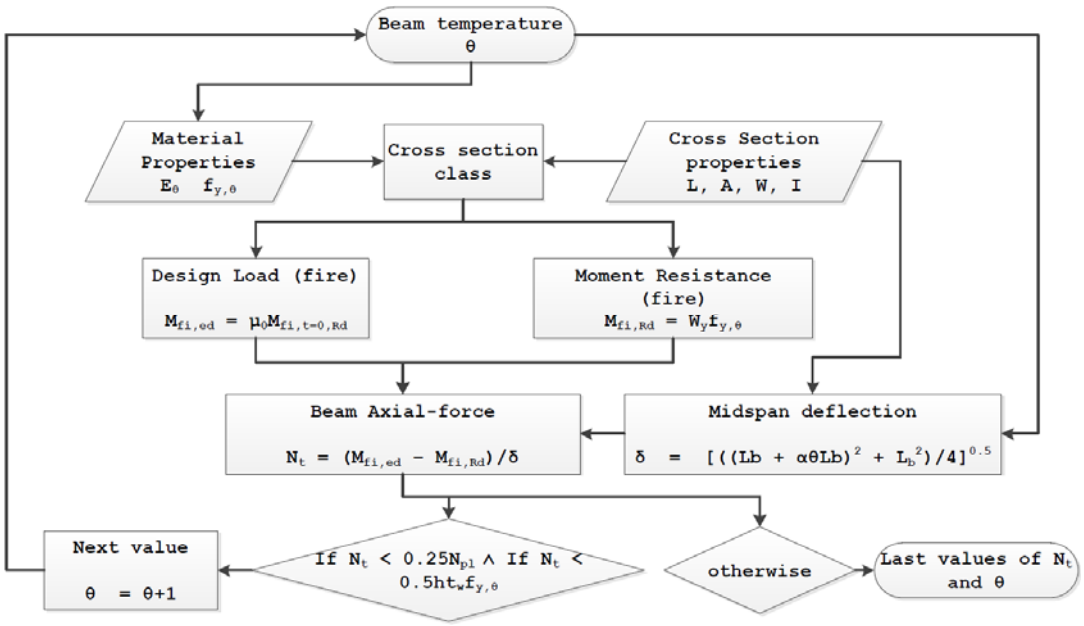

Figure 7: Schematic Diagram of the Calculation of Temperature during the Catenary Phase up to which there is no Interaction between the Axial Force and the Bending Moment Resistance

Last point (4) on the curve is determined by assuming that the bending moment resistance is zero and catenary action is solely responsible for resisting the imposed load. The catenary force is equal to the tensile capacity of the beam at this point; beyond this point the beam undergoes runaway deflection.

3. FINITE ELEMENT MODEL

The hand calculation procedure has been validated using FE Analysis, in Abaqus [14]. The FE models were validated against test results on sub-frames at elevated temperatures discussed below.

3.1 Sub-frame Tests

The sub-frame tests were performed at the University of Coimbra. This was done within a European project COMPFIRE [15]. Under the COMPFIRE project, a novel connection consisting of a reverse channel between steel beam and Concrete Filled Tubular (CFT) columns was studied at elevated temperatures. The aim of this project was to demonstrate the large rotational capacity of this connection type at elevated temperatures compared to other types of connections [15].

Full scale tests were carried out on sub-frames consisting of an IPE 300 profile beam supported at each end by a CFT column through reverse channel connections. The columns are 3525 mm tall and the beam has a 5000 mm long span shown in Figure 8 [16]. Other details of test specimens are given in Table 1 below.

Table 1. List of Sub-frame Models at Elevated Temperature

Test n°	*Temperature curve*	*Column section*	*Reverse channel*
1.	Heating1 + cooling	SHS 250x10	U 200x90x10
2.	Heating2 + cooling	SHS 250x10	U 200x90x10
3.	Heating1 + cooling	SHS 250x10	U 200x90x8
4.	Heating1 + cooling	SHS 250x10	U 200x90x12

In each case, the beam has a utilization factor of 0.2, i.e. 47 kN constant load. The connections, webs and the bottom flanges are heated using flexible ceramic heating pads. The top flange was not directly heated in order to simulate the heat sink effect of the concrete slab. The column was also not heated directly [16].

The measurements made during the tests include the midspan deflection, reaction forces at the column ends and temperatures along the beam span and connections.

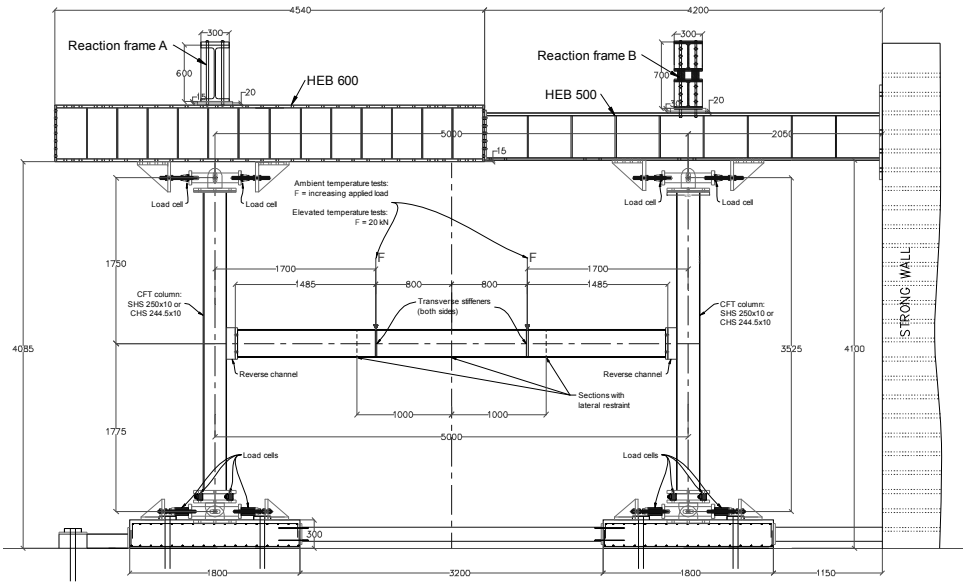

Figure 8. Experimental Setup of the Sub-frame Tests [16]

The lateral torsional instability is prevented by restraining lateral translation along the span of the beam.

All steel components are made of Steel S355 except the end-plates, which are of S275. The concrete in CFT column is grade C30\37. The bolts in connection are M24 grade 10.9 [16].

3.2 Connection Strength

The reverse channel connection is expected to behave as a semi-rigid connection. There are presently no rules in Eurocode 3 for calculation of the strength and initial stiffness of reverse channel connections, therefore numerical procedures have been used for their calculation using FE Models of the connections shown in Figure 9.

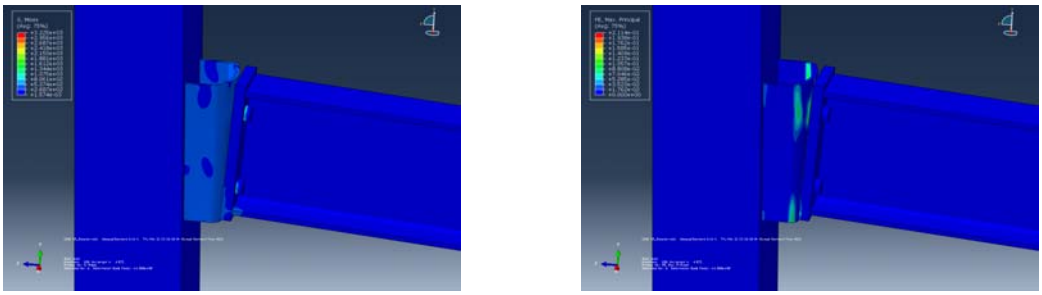

Mises Stress distribution Principal plastic strain distribution

Figure 9. Deformed Shape of a Reverse Channel Connection

The moment-vs-rotation diagram is plotted for the connection by measuring the rotation of the beam near the connection. These plots are shown below in Figure 10.

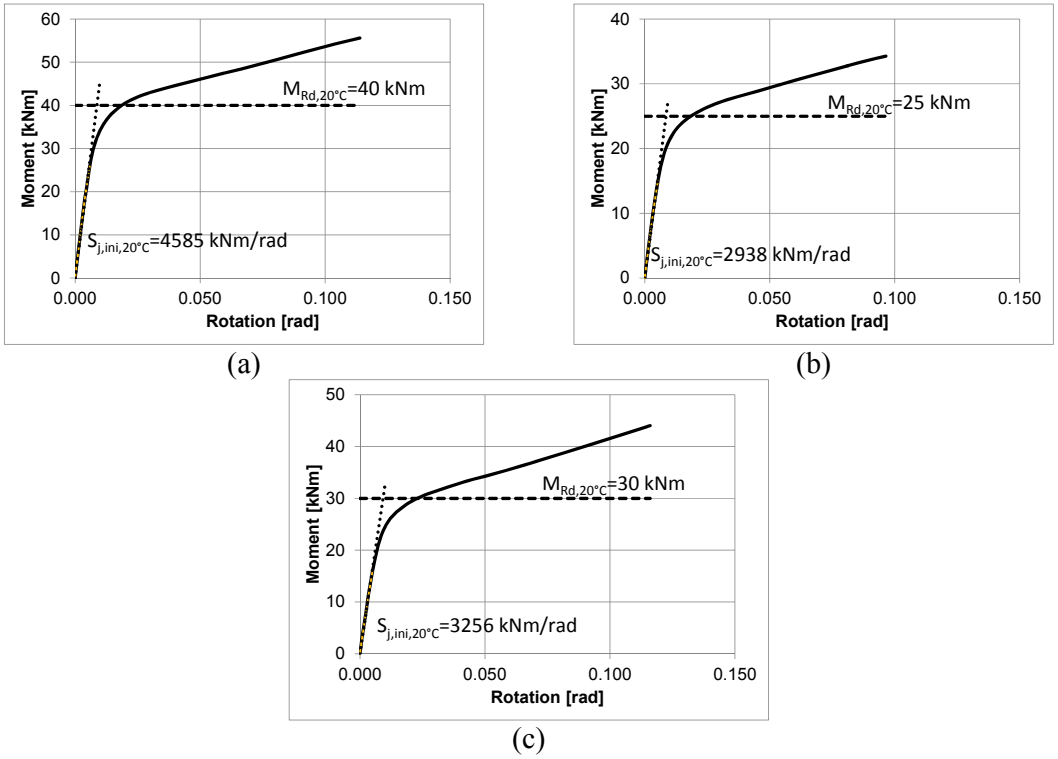

Figure 10. Moment-vs-rotation Diagram of Reverse Channel Connection

(a) 12 mm thickness, (b) 8mm thickness, (c) 10 mm thickness

The stiffness and strength of the three different reverse channel connections are summarised below in Table 2.

Table 2. Initial Stiffness and Strength of the Reverse Channel Connections

Reverse channel thickness (mm)	*Initial Stiffness ($S_{j,ini,20°C}$) kNm/rad*	*Connection strength ($M_{Rd,20°C}$) kNm*
12	4585	40
10	3256	30
8	2938	25

3.3 Material model

The material models used in the FE-models were based on the coupon tests conducted on specimens from the different structural components, also done at the University of Coimbra. Specimens from all components were tested at room temperature only, except the ones from channel component, which was also tested at elevated temperatures. The results from these coupon tests are summarized in Table 3 [15].

Table 3. Mechanical Properties of Steel from Coupon tests [15]

Structural component	*Temperature (°C)*	*Nominal yield strength (MPa)*	*Test result*	
			Yield strength (MPa)	Ultimate strength (MPa)
End-plate (S275)	20	275	236.7	424.7
I-Beam (S355)	20	355	446	562
SHS (S355)	20	355	554.7	621.3
Reverse channel, SHS (S355)	20	355	513.3	558.7
	200	355	489.3	515.7
	400	355	447.3	473
	600	166.9	249.7	252.3
	800	39.1	119.7	124
Mean (20°C)			437.7	541.7
Standard Deviation (20°C)			122.3	71.9

The tri-linear stress-strain curve for carbon steel at elevated temperatures from EN 1993-1-2, shown in Figure 11, was used in the FE Models [11]. This stress-strain model does not consider strain hardening; therefore only yield strength values are taken from the coupon tests.

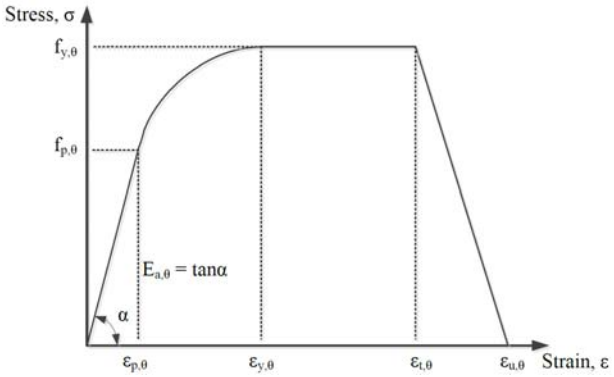

Figure 11. Stress-strain Relationship for Carbon Steel at Elevated Temperatures [12]

The stress-strain curves for the channel component at different temperatures, according to Table 3, are shown in Figure 12. For the other components the reduction factors from EN 1993-1-2 were used for the curves at elevated temperatures. Eq. 3.1 and Eq. 3.2 are used to calculate the true values of the stresses and strains from their nominal values [14].

$$\varepsilon_{\text{true}} = \ln\left(1+\varepsilon_{\text{nom}}\right) \tag{3.1}$$

$$\sigma_{\text{true}} = \sigma_{\text{nom}}\left(1+\varepsilon_{\text{nom}}\right) \tag{3.2}$$

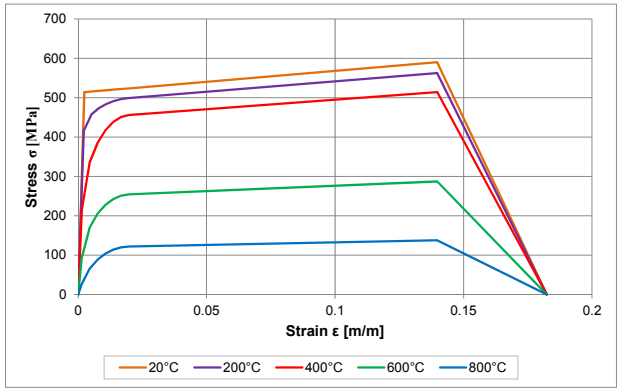

Figure 12. Stress-strain Curve at Elevated Temperatures from Coupon Tests

Nominal material properties of bolt grade 10.9 from EN 1993-1-1 were used [17]. The stress-strain model for the bolts was based on the analytical model proposed in the European project COSSFIRE [18]. Figure 13 shows this model at different temperatures for the bolt grade 10.9.

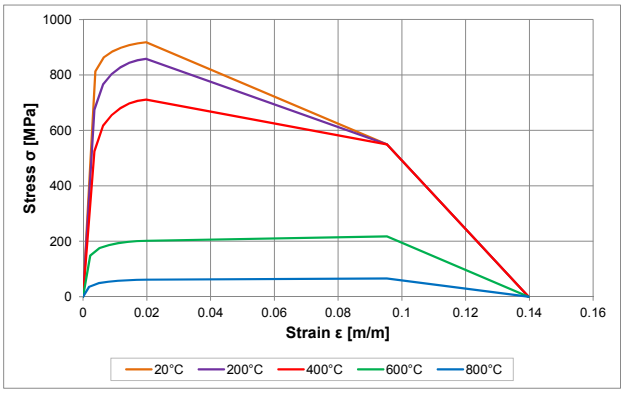

Figure 13. Stress-strain Curve at Elevated Temperatures for Bolt Material

3.4 Element Type

The sub-frame has been modelled using 3D solid reduced integration elements C3D8R. The use of first order reduced integration elements can reduce computation time but the drawback for such elements can be 'hourglassing'. However, in Abaqus, first order reduced integration elements possess hourglass controls, which in combination with a fine mesh can solve the problem of 'hourglassing'.

3.5 Analyses Procedure

The analysis of the sub-frame model is performed in a series of four 'Static general' steps described below:

Bolt pretensioning: As the first step in the simulation, the bolts are pretensioned in order to initialize the contact interactions and prevent any rigid body motions later in the analysis.

Fixing the bolt length: The second step, is to fix the bolts at their current lengths using Abaqus bolt load option 'fix-current-length'. Bolts are passive entities and not actively force driven; therefore this step ensures this by keeping the bolts at a particular compression distance.

Load application: A pressure load is applied on the top flange of the beam on an area and at positions corresponding to the tests.

Temperature incrementation: In the last step, thermal loading is applied as increasing temperature in the model as a predefined field according to the temperature-time measurements made in the tests.

4. VALIDATION OF FE MODEL

The axial force and midspan deflection obtained from the analysis of the FE models have been compared to the corresponding results from the tests. Figure 14 and Figure 15 show these results for the beam axial force and the midspan deflection respectively.

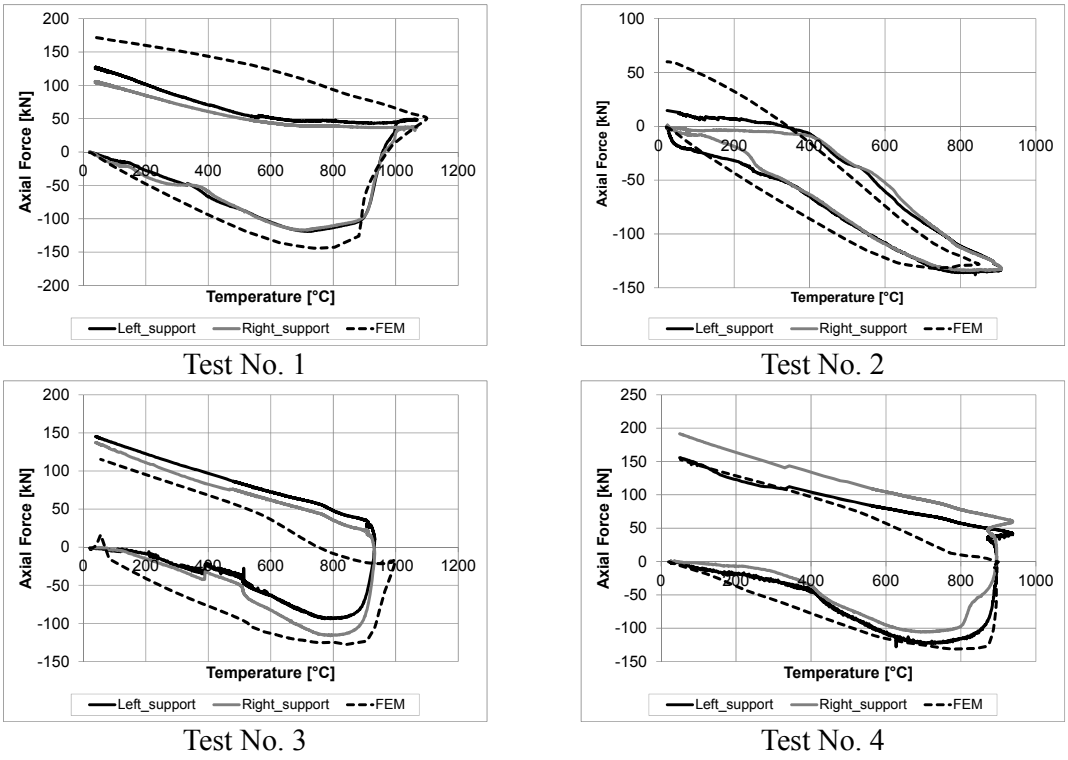

Figure 14. Axial force-vs-temperature from Tests and Finite Element Modelling

Figure 14 shows that the variation of axial force in the FE models is very close to the test results. However, Figure 15 shows relatively sharp difference between the FE models and test results. Two reasons could be attributed to this difference; firstly FE models are generally expected to give stiff response. Second could be the uncertainty of the material strength at elevated temperature compared to Eurocode. Nevertheless, the results are close enough to warrant the reliability of the FE models for this study.

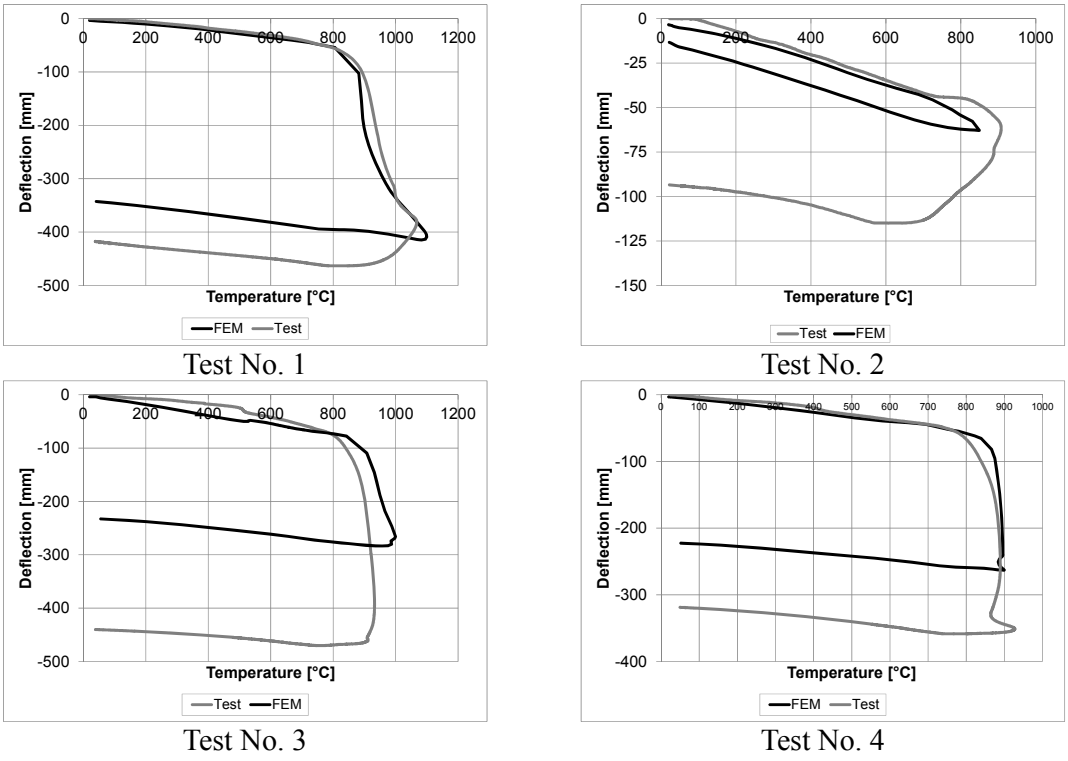

Figure 15. Midspan deflection-vs-temperature from Tests and Finite Element Modelling

5. VALIDATION AND DISCUSSION OF ANALYTICAL METHOD

The validated FE models have been further used here to verify the proposed analytical procedure. Two different load levels (fraction of the ambient temperature design resistance) for each of the three channel thicknesses of the connection are used for comparison between FE model and analytical procedure. Table 4 presents a list of the models used here.

Table 4. FE-models used for the Verification of the Analytical Procedure

No.	*Beam profile*	*Reverse channel thickness (mm)*	*Load level*
1.	IPE 300	8	0.4
2.	IPE 300	8	0.6
3.	IPE 300	10	0.4
4.	IPE 300	10	0.6
5.	IPE 300	12	0.4
6.	IPE 300	12	0.6

Figure 16 and Figure 17 show these comparisons for axial force and midspan deflection, respectively two support conditions, i.e. simply supported and semi-rigid (reverse channel).

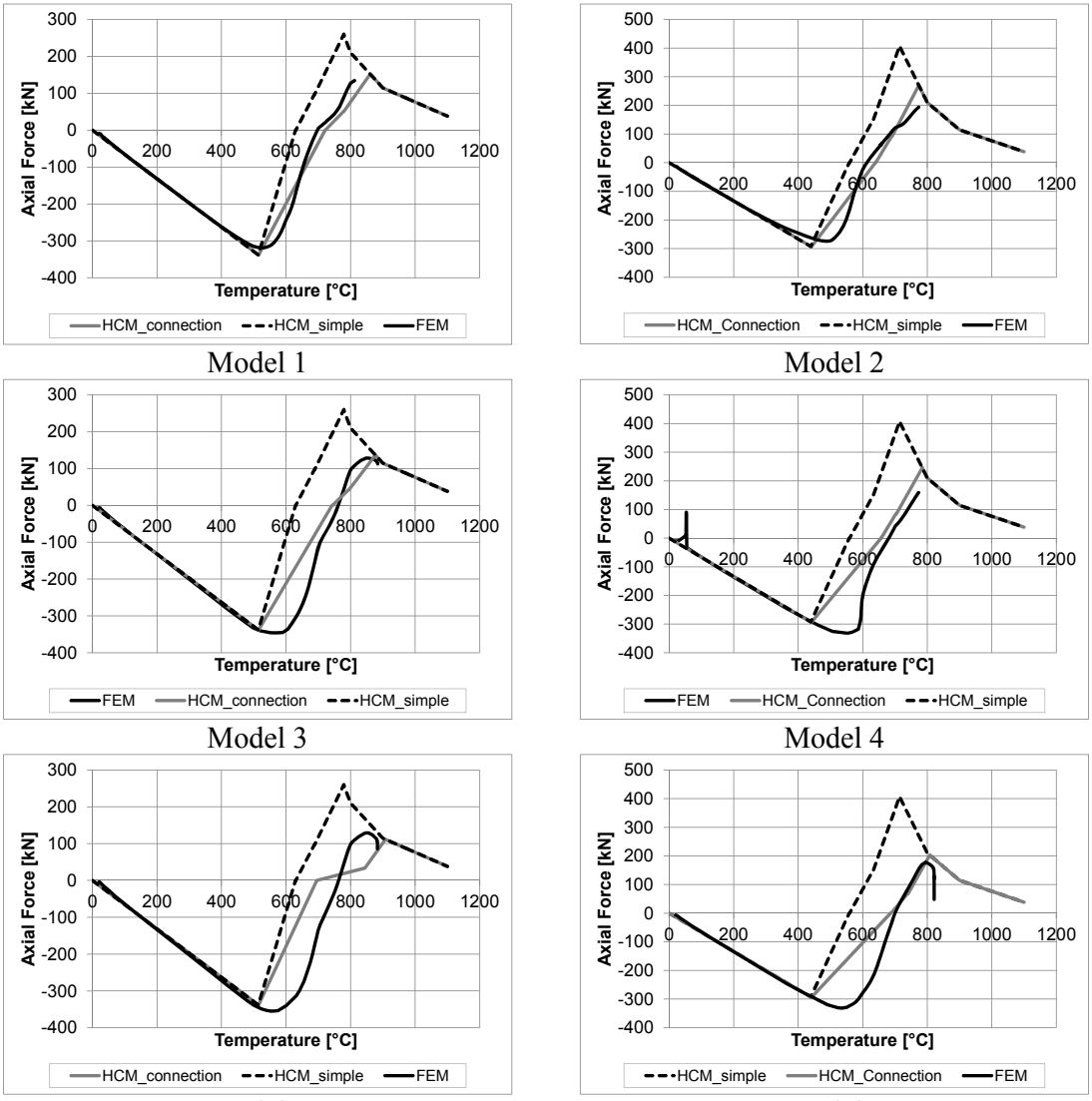

Figure 16. Variation of Axial Force in Steel Beam with Increasing Temperature

Comparison between the FE models and the tests and later the analytical procedure gives some important insights. Figure 14 shows similar response between FE models and tests of compression in the initial phase and tensile catenary action in the later phase of heating. Test 2 is an exception where the beam has not been heated until the catenary phase and was cooled off earlier. All tests show the beam to be in tension during the cooling phase. Test 1 shows the highest tensile force in the catenary phase due to being heated the most.

Test 1 and Test 2 shows the biggest difference from the FE model in terms of the tensile force after cooling. Difference in the column stiffness could be the reason for this as the column was not heated in the FE model. The difference in deflection between the FE models and tests could be due to the difference in real material properties at elevated temperatures and the ones proposed by Eurocode as used in FE models.

The comparison between the FE models and the analytical procedure, according to Figure 16, shows the significance of using the connection moment in the calculation procedure. Table 5 gives a summary of the results from the comparison.

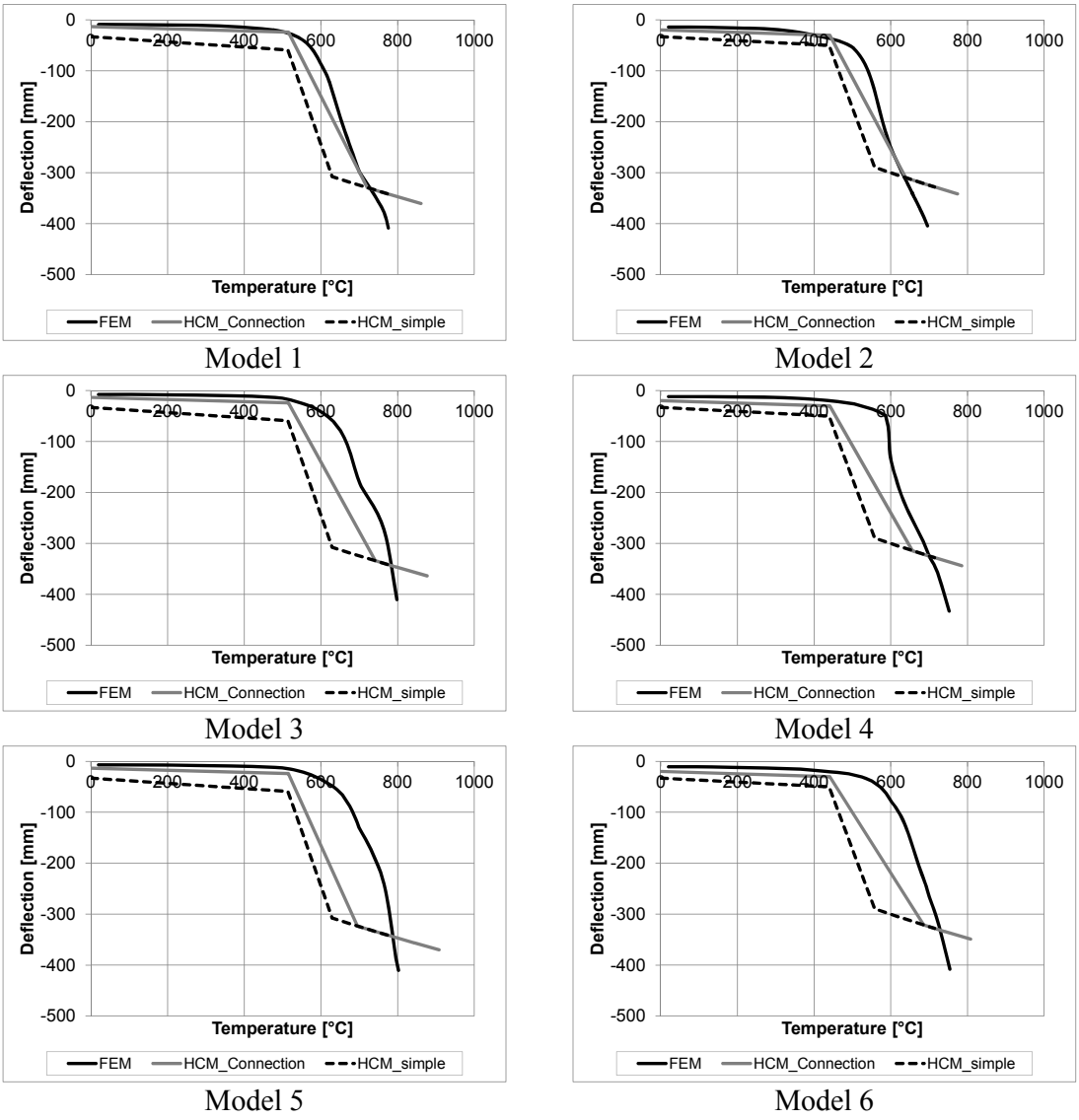

Figure 17. Variation of Midspan Deflection in Steel Beam with Increasing Temperature

Table 5. Results from FE-models and Hand Calculation Procedures

No.	*Maximum compressive force (kN)*			*Temperature (zero axial force) [°C]*					*Maximum tensile force(kN)*				
	FEM	HCM	Diff. %	FEM	HCM (simple supports)	Diff. %	HCM (Connection moment)	Diff. %	FEM	HCM (simple supports)	Diff. %	HCM (Connection moment)	Diff. %
Model-1	318	338	6.29	697	629	9.7	721	3.43	135	260	93.4	152	13.2
Model-2	274	294	7.23	616	558	9.35	639	3.83	194	408	110	267	39
Model-3	346	338	2.33	763	629	17.6	742	2.8	129	260	102	137	6.38
Model-4	332	294	11.46	684	558	18.5	657	4.0	159	408	156	247	55
Model-5	355	338	4.65	764	629	17.7	695	9.0	129	260	101	112	13.2
Model-6	331	294	11.33	700	558	20.3	686	2.0	178	408	129	203	14.4

From the results in Table 5, it can be seen that consideration of the connection reduces the difference between the results from FE models and the analytical. The simply supported beam assumption in the analytical procedure gives conservative results for point (2) and point (4).

Similarly the midspan deflection from the analytical procedure with connection moment included (Figure 17) shows convergence towards the numerical results, whereas the model based on simple support assumption is diverging with increasing temperature. A detailed design example is provided in the ANNEX for a given beam and column dimensions.

5. DISCUSSION AND CONCLUSIONS

The method presented in this study is based on the assumption that the temperature is uniform across the beam cross section depth. However, in reality the temperature of the top flange can be lower than the web and bottom flange due to its proximity to the concrete slab. This would cause the beam to have a higher resistance at elevated temperature than shown here and could be incorporated into future extension of this approach. The restrained thermal expansion of the beam will induce second order bending moment in the compressive phase of the beam, which has not been taken into account here based on small deflection assumption; however, this can also be introduced as a further extension to this proposed approach in future work.

Main conclusions derived from the study presented here are as follows:

- In the absence of a component method procedure for the connection type considered in this study, a numerical approach was adopted which gave a satisfactory estimation of the connection strength. This is born out of the fact that the analytical procedure has been significantly accurate with these estimated connection strength used as inputs.
- At elevated temperatures material properties such as it strength and stiffness degrade; this degradation has certain uncertainty associated with them, but despite this fact the FE models have been able to simulate the behaviour of the tests satisfactorily. .
- The connection moment resistance at elevated temperatures, though not very significantly high, can contribute towards significantly increasing the conventional limiting temperature (defined by the point of zero axial force in the beam). This increase in temperature can range from 60 °C to 120 °C, from its value without it.
- The semi-rigid connection contributes towards reducing the difference between the maximum catenary force from the analytical procedure and the FE model results. The difference is 24% for the procedure with semi-rigid connection whereas 115% for the procedure without semi-rigid connections.
- The deflection profile obtained from the analytical procedure is also much closer to the FE model results when considering the contribution of the semi-rigid connection. This indicates that the connection strength is significant despite the fact that the connection type considered here in this study is not a moment type connection.

ACKNOWLEDGMENT

The authors acknowledge the funding from the European Community's Research Fund for Coal and Steel (RFCS) under grant agreement n° RFSR-CT-2009-00021, which leads to the research work presented here.

REFERENCES

[1] McAllister, T.P., "Structural Fire Response and Probable Collapse Sequence of World Trade Center Building 7, Federal Building and Fire Safety Investigation of the World Trade Center Disaster (NIST-NCSTAR 1-9) VOUMES 1 and 2", National Institute of Standards and Technology, NIST, 2008, pp. 1129–1140.

[2] Kirby, B.R., "Large Scale Fire Tests: The British Steel European Collaborative Research Programme on the BRE-8", Fire Safety Science - Proceedings of the Fifth International Symposium , 1997, pp. 1129–1140.

[3] Liu, T.C., Fahad, M., Davies, J., "Experimental Investigation of Behaviour of Axially Restrained Steel Beams in Fire", Journal of Constructional Steel Research , 2002, Vol. 58, No. 9, pp. 1211–1230.

[4] Yin, Y.Z. and Wang, Y.C., "A Numerical Study of Large Deflection Behaviour of Restrained Steel Beams at Elevated Temperatures", Journal of Constructional Steel Research, 2004, Vol. 60, No. 7, pp. 1029–1047.

[5] Yin, Y.Z. and Wang, Y.C., "Analysis of Catenary Action in Steel Beams using a Simplified Hand Calculation Method, Part 1: Theory and Validation for Uniform Temperature Distribution", Journal of Constructional Steel Research, 2005, Vol. 61, No. 2, pp. 183–211.

[6] Yin, Y.Z. and Wang, Y.C., "Analysis of Catenary Action in Steel Beams using a Simplified Hand Calculation Method, Part 2: Validation for Non-uniform Temperature Distribution," Journal of Constructional Steel Research , 2005, Vol. 61, No. 2, pp. 213–234.

[7] Li, G.Q. and Guo, S.X., "Experiment on Restrained Steel Beams subjected to Heating and Cooling", Journal of Constructional Steel Research , 2008, Vol. 64, No. 3, pp. 268–274.

[8] Santiago, A., da Silva, L.S., Real, P.V. and Veljkovic, M., "Numerical Study of a Steel Sub-frame in Fire", Computers and Structures , 2008, Vol. 86, No. 15, pp. 1619–1632.

[9] Gillie, M., "Analysis of Heated Structures: Nature and Modelling Benchmarks", Fire Safety Journal , 2009, vol. 44, no. 5, pp. 673–680.

[10] Wang, Y.C., Burgess, I., Wald, F. and Gillie, M., "Performance Based Fire Engineerig of Structures", CRC Press , 2012, 1st Edition, pp. 394.

[11] EN 1993-1-2, Eurocode 3: Design of Steel Structures Part 1-2: General Rules-Structural Fire Design, Brussels: European Committee for Standardization, 2004.

[12] Usmani, A.S., Rotter, J.M., Lamont, S., Sanad, A.M. and Gillie, M., "Fundamental Principles of Structural Behaviour under Thermal Effects", Fire Safety Journal , 2001, Vol. 36, No. 8, pp. 721–744.

[13] Dwaikat, M.M.S. and Kodur, V.K.R., "A Performance based Methodolgy for Fire Design of Restrained Steel Beams", Journal of Constructional Steel Research , 2011, Vol. 67, No. 3, pp. 510–524.

[14] Abaqus, Abaqus Users' Manual v6.12, Simulia, RI, USA, 2012

[15] da Silva, L.S., Santiago, A., Lopes, F., Veljkovic, M., Heistermann, T., Iqbal, N., Wald, F., Jana, T., Davison, B., Burgess, I., Huang, S-S., Dong, G., Wang, Y., Mandal, P., Hu, Y., Jafarian, M., Koutlas, G. (2013). COMPFIRE: Design of Composite Joints for Improved Fire Robustness. Final Report No. 4, Research Fund for Coal and Steel, Grant agreement n.º RFSR-CT-2009-00021, European Commission, Brussels.

[16] Lopes, F., Santiago, A., da Silva, L.S., Iqbal, N., Veljkovic, M and da Silva, J.G.S., "Sub-frames with Reverse Channel Connections to CFT Composite Columns-experimental Evaluations", Advanced Steel Construction , 2015, Vol. 11, No. 1, pp. 110–125.

[17] EN 1993-1-1, Eurocode 3: Design of Steel Structures Part 1-1: General Rules and Rules for Buildings, Brussels: European Committee for Standardization, 2005.

[18] Zhao, B., Roosefid, M. (2009). COSSFIRE: Connections of Steel and Composite Structures under Natural Fire Conditions. Final Report No. 6, Research Fund for Coal and Steel, Grant Agreement n.º RFSR-CT-2006-00028, European Commission, Brussels.

ANNEX

Design Example:

Determine the maximum axial compressive force and the maximum axial tensile force generated in a 6 m unprotected steel beam exposed to a standard fire (ISO 834). The cross sectional profile of the beam is an IPE 330 made of steel grade S355 and it is connected at its ends to supporting HD 360x134 profile columns through semi-rigid reverse channel connections. The floor height is 3.5 meters. The utilization factor of the beam is 0.4.

Step 1: Cross section classification

For fire design situation: $\varepsilon_\theta = 0.85\sqrt{235/f_y} = 0.85\sqrt{235/355} = 0.692$

[EN 1993-1-2]
Top flange [outstand compression element]
Width to thickness ratio:

$9\varepsilon_\theta < c_f/t_f = 5.06 < 10\varepsilon_\theta \Rightarrow$ class = 1 [EN 1993-1-1: table 5.2]

Web [internal compression element]
Width to thickness ratio:

$42\varepsilon_\theta > c_w/t_w = 36.13 \Rightarrow$ class = 4 [EN 1993-1-1: table 5.2]

Step 2: Effective cross-section properties:

Stress distribution ratio (web): $\psi = 1$
Plate buckling factor (web): $k_\sigma = 4.0$
Plate slenderness (web): $\lambda_p = [c_w/t_w]/[28.4 \cdot \varepsilon \cdot \sqrt{k_\sigma}] = 0.782$
[EN 1993-1-5: section 4.4]
Reduction factor: $\rho = [\lambda_p - 0.055(3+\psi)]/\lambda_p^2 = 0.919$
[EN 1993-1-5: section 4.4]
Effective web width: $h_{w,eff} = \rho \times h_w = 249.07$ mm
Area of effective cross section: $A_{eff} = 6096$ mm^2
Moment of inertia (strong axis): $I_{eff} = 117693414$ mm^4

Step 3: Axial support stiffness (columns):

Length of column: $L_c = 2 \times$ floor height = 7 m
Axial support stiffness: $K_c = 192EI_c/L_c^3 = 48.8$ kN/mm

Step 4: Maximum compressive force (Point-1):
At temperature θ:

Axial force in the beam due to restrained thermal expansion:

$$N_{Ed} = EA\alpha\theta / [1 + EA/(0.5K_c L_b)]$$

Axial force capacity of the beam: $N_{b,fi,Rd} = \chi_{fi} k_{y,\theta} f_y A_{eff}$

Bending moment resistance at 20°C: $M_{c,Rd} = W_{el,eff} f_y / \gamma_{Mfi} = 253$ kNm

Applied bending moment in fire: $M_{fi,ed} = 0.4 M_{c,Rd} = 101$ kNm

Bending moment resistance in fire: $M_{fi,Rd} = W_{el,eff} k_{y,\theta} f_y / \gamma_{Mfi}$

Design resistance for combined bending and compression:

$$N_{Ed}/N_{b,fi,Rd} + k_y M_{fi,Ed}/M_{fi,Rd} \leq 1$$

Where, $k_y = 1 - \mu_y N_{Ed}/N_{b,fi,Rd} \leq 3$

And $\mu_y = (1.2\beta_{M,y} - 3)\lambda_\theta + 0.44\beta_{M,y} - 0.29 \leq 0.8$

[EN 1993-1-2]
Incrementally increasing the temperature until the design resistance for combined bending and compression is reached:
$\theta_1 = 391°C$, $N_1 = 605$ kN [maximum compressive force]

Step 5: Zero Axial force (Point-2)

Bending moment capacity of connection 20°C: $M_{conn} = 40$kNm

As a first iteration:

Assuming simple supports: $f_{y,\theta} = M_{fi,Ed}/W_{el,eff} = 142$MPa

Reduction factor: $f_{y,\theta} = 142$MPa $\Rightarrow k_{y,\theta} = f_{y,\theta}/f_y = 0.4$

Beam temperature: $k_{y,\theta} = 0.4 \Rightarrow \theta = 629°C$

Connection temperature:

$$\theta_{conn} = 0.88\theta(1 - 0.3\,h/D) = 470°C \text{ for } h/D = 0.5$$

[EN 1993-1-2]
Reduction factor (connection): $\theta_{conn} = 470°C \Rightarrow k_{y,conn} = 0.845$

Connection resistance: $M_{conn,fi} = k_{y,conn} M_{conn} = 33.8$kNm

Considering connection resistance to calculate $f_{y,\theta}$

$$f_{y,\theta} = [M_{fi,Ed} - 2M_{conn,fi}]/W_{el,eff}$$

Using $f_{y,\theta}$ to perform the next iteration and so on until the reduction factor $k_{y,conn}$ becomes repetitive:
$k_{y,conn} = 0.52 \Rightarrow M_{conn,fi} = 20.8$kNm $\Rightarrow f_{y,\theta} = (M_{fi,Ed} - 2M_{conn,fi})/W_{el,eff} = 83.7$MPa
$f_{y,\theta} = 83.7$MPa $\Rightarrow k_{y,\theta} = f_{y,\theta}/f_y = 0.236$
$k_{y,\theta} = 0.236 \Rightarrow \theta_2 = 698°C$

Step 6: Tensile force (bending-tension interaction) (Point-3)

In the catenary phase, initially the bending moment resistance is significant, thus interaction with the tensile force is taken into account.
For an incrementally increasing temperature $\theta > \theta_2$:
Residual Moment: $\Delta M = M_{fi,Ed} - M_{fi,Rd} - 2M_{conn,fi}$

Beam deflection: $\delta=\sqrt{[(L+\alpha\theta L)/2)^2-(L/2)^2}$

Axial force: $N_t = \Delta M/\delta$

Stop the incrementation when: $N_t \geq N_{t,Rd}$ OR $N_t \geq 0.5ht_w f_{y,\theta}$

The values obtained are: $\theta_3 = 778°C$, $N_3 = 70kN$

Step 7: Maximum tensile force (Point-4)

For an incrementally increasing temperature $\theta > \theta_3$:

Beam tensile resistance: $N_{t,fi,Rd} = Af_{y,\theta}/\gamma_{Mfi}$

Beam deflection: $\delta=\sqrt{[(L+\alpha\theta L)/2)^2-(L/2)^2}$

Residual Moment: $\Delta M = M_{fi,Ed} - 2M_{conn,fi}$

Stop the incrementation when: $N_{t,fi,Rd} \times \delta = \Delta M$

The values obtained are: $\theta_4 = 869°C$, $N_4 = 168.7kN$

LATERALLY RESTRAINED STEEL PLATE WITH STIFFENERS FOR SEISMIC RETROFITTING OF CONCRETE COUPLING BEAMS

B. Cheng[1], R.K.L. Su[2*], C. Shi[3] and C.T. Yang[3]

[1]*Associate Professor, Department of Civil & Transportation Engineering, Beijing University of Civil Engineering and Architecture, China*
[2] *Associate Professor, Department of Civil Engineering, The University of Hong Kong, Pokfulam Road, Hong Kong, China*
[3]*Master Candidate, Department of Civil &Transportation Engineering, Beijing University of Civil Engineering and Architecture, China*
**(Corresponding author: E-mail: klsu@hku.hk)*

Received: 15 April 2015; Revised: 18 September 2015; Accepted: 7 October 2015

ABSTRACT: Existing deep reinforced concrete (RC) coupling beams with low shear span ratios and conventionally reinforced shear stirrups tend to fail in a brittle manner with limited ductility and deformability under reversed cyclic loading. Previous studies have developed a new retrofitting method with an unstiffened laterally restrained steel plate (LRSP) for existing deep RC coupling beams. By utilizing the post-buckling loading capacity of steel plate, the deformability and energy dissipation of the retrofitted coupling beams were enhanced while maintaining flexural stiffness during an earthquake. However, the occurrence of early plate buckling usually results in reduced strength, stiffness and energy dissipation capacity accompanied by significant pinching. In this study, half-scale deep RC coupling beams rehabilitated by LRSP with stiffeners were tested. The results demonstrate that the type of bolt connection greatly influences the performance of retrofitted coupling beams. The additional stiffeners can prevent plate buckling and ensure that the steel plate has a wider yield area and hence higher energy dissipation.

Keywords: Deep coupling beams, seismic retrofitting, laterally restrained steel plate, stiffener, bolt connection

DOI: 10.18057/IJASC.2016.12.2.7

1. INTRODUCTION

The need to retrofit in earthquake prone regions may arise directly from the problems of aging infrastructure, recognition of the vulnerability of existing infrastructure, updates in seismic code requirements, or changes in building performance objectives. Coupled shear walls are very frequently incorporated into high rise buildings as a primary lateral resisting system. Coupled beams in coupled shear walls are very important structural components that provide the necessary lateral strength, stiffness and deformability for the whole building to resist extreme wind and earthquake loads. In past decades, the design of many concrete buildings such as in Hong Kong have not taken into account earthquake actions. Following the introduction of the new design codes, many existing coupling beams are found to be deficient in shear capacity. Paulay [1] has pointed out that deep reinforced concrete (RC) coupling beams are prone to brittle failure in the form of diagonal or sliding failure when insufficient shear reinforcement is used. Past earthquake records [2, 3] also reveal that many deep RC coupling beams have been seriously damaged in a typical shear failure mode during major earthquakes. Under strong earthquake loads, brittle failures of these coupling beams could significantly affect their energy dissipation ability and the structural safety of the entire building. To improve the seismic resistance of existing buildings, many coupling beams deficient in shear or lacking in deformability need to be retrofitted.

Only a few studies in the literature are related to the seismic retrofitting of existing RC coupling beams. Harries et al. [4] studied a shear strengthening method for existing coupling beams with a span-to-depth ratio of 3.0. In their study, the retrofitting involved a number of different attachment methods to fix the steel plate to one side of the coupling beams. They found that the hybrid method of bolting and epoxy bonding to attach the steel plates both in the span and at the ends performed the best. Su and Zhu [5] studied a shear strengthening method for RC coupling beams with a span-to-depth ratio of 2.5. To strengthen the coupling beams, they bolted the steel plate to both ends of the wall panels without adhesive bonding. Their experimental studies showed that this retrofitting method could greatly increase the shear capacity of medium length coupling beams, while fastening the retrofit plate to the span of a concrete beam could prevent local buckling of the steel plates, but this led to serious concrete damage at the failure stage. In all experiments of Su and Zhu, minor buckling of the steel plate was observed and the effects of local buckling on the behavior of strengthened coupling beams were not investigated. The widths of door and window openings usually range from 1.0 to 1.5 m, while height ranges from 1.5 to 2.5 m; thus, many coupling beams above the openings are rather short and deep. Su and Cheng [6, 7] experimentally studied the use of a laterally restrained steel plate (LRSP) without stiffeners to retrofit deep concrete coupling beams with a span-to-depth ratio of 1.1. In the test, thin mild steel plates were utilized. The steel plate started to develop a diagonal tension field after the onset of global buckling at the early stages of loading and exhibited nonlinear behavior at relatively small inter-story drift ratios. Due to the post-buckling loading capacity and tension field action in the steel plate, LRSP retrofitted coupling beams failed in a ductile manner. Cheng and Su [8] conducted a numerical parametric study to investigate the influence of plate buckling on the LRSP retrofitted coupling beams. However, shear buckling of steel plate in the early stages usually results in reduced strength, stiffness and energy dissipation capacity accompanied by significant pinching. Lu and Li [9] proposed slim buckling-restrained steel plate shear walls to seismically strengthen the lateral load resistance of buildings. The stable hysteresis curve, good deformability, and high energy dissipating ability of the proposed buckling-restrained steel plate shear wall were demonstrated experimentally. In this study, we attempt to add steel stiffeners to the steel plate to defer the shear buckling and to increase the energy dissipation capacity of the retrofitted beams. A series of LRSPs with stiffeners have been tested to investigate the effectiveness of the proposed method in the prevention of pinching of the hysteresis curves and increasing the energy dissipation capacity of the retrofitted coupling beams.

2 LRSP RETROFITTING METHOD

The main characteristic of the LRSP retrofitting method is the use of a plate buckling control device, which is composed of steel angles (Figure 1). Cheng and Su [7] applied the plate buckling control device to effectively suppress laterally out-of-plane plate buckling. To avoid adding extra flexural strength and stiffness to the retrofitted coupling beam, the lateral stiffeners are connected to a steel plate by bolt connections with slotted holes, which allow the two lateral stiffeners to freely rotate and move in the longitudinal direction. The advantage of using a plate buckling restraining device instead of adding stiffeners to the steel plates to control plate buckling is that the stiffness of the coupling beams would not be increased. This is important because the increase in the beam's stiffness would stiffen the lateral load resisting system and cause the structure to attract more seismic loads, which might lead to early failure of the coupled shear walls under strong seismic loads. Experimental studies have demonstrated that, for the specimens with the buckling control device, plate buckling at the beam-wall joints is suppressed. A continuous shear transfer medium across the joints, provided by the steel plate, can continue to take a larger share of the load in the post peak region and alleviate concrete crushing in the compression region. As a result, LRSP retrofitted coupling beams failed in a more ductile fashion.

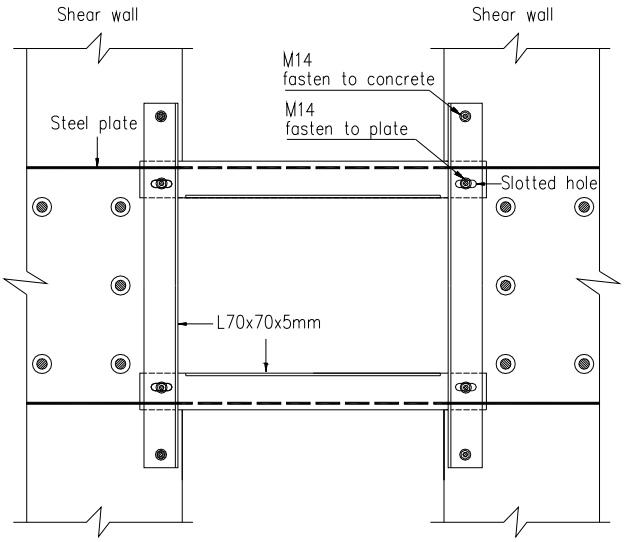

Figure 1. LRSP Retrofitting Method

3. EXPERIMENTAL PROCEDURE

3.1 Description of Test Specimens

Five specimens with the same dimensions and reinforcement specifications (see Figure 2a), but different retrofitting schemes, were fabricated and tested. Each beam was connected to two RC panels, simulating a section of the coupled shear walls, to properly model the beam-wall interactions. Two base beams were attached to the top and bottom ends of each specimen and rotated 90^o to fix the specimen onto the loading frame via anchor-bolt connections.

The sizes of the coupling beams were 450 mm deep by 120 mm wide, with a clear span of 500 mm and a span-to-depth ratio of 1.11. The top and bottom longitudinal reinforcements of the coupling beams consisted of four 12 mm diameter high-yield reinforcement bars with a steel ratio of 0.8%, and the side bars included four 8 mm diameter mild steel round bars. The shear reinforcements in the coupling beams consisted of four 8 mm diameter hoops with a 125 mm pitch. This shear reinforcement arrangement was selected to represent the shear-deficient coupling beams in old existing buildings.

Given the limited load capacity of a 500 kN hydraulic jack, the original coupling beam DCB8 was designed to achieve a loading of less than 50% of the jack capacity, according to the provisions given in the old British Standard CP114 [10], meaning that the jack was able to cause the retrofitted coupling beams to fail. For the specimens with a bolted steel plate, the capacity of the steel plates should not be higher than 250 kN. The shear capacity of steel plates was designed according to the British Standard BS5950 [11] with a full plastic assumption, which ignored the effects of steel plate buckling and bolt group slippage. The material properties of concrete, steel and rebar are shown in Table 1. Through the design calculation, thin steel plates of 4.5 mm were selected.

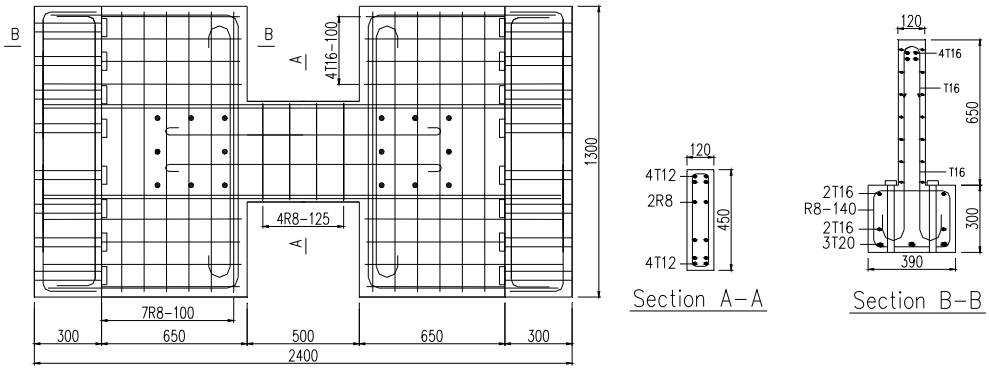

(a)

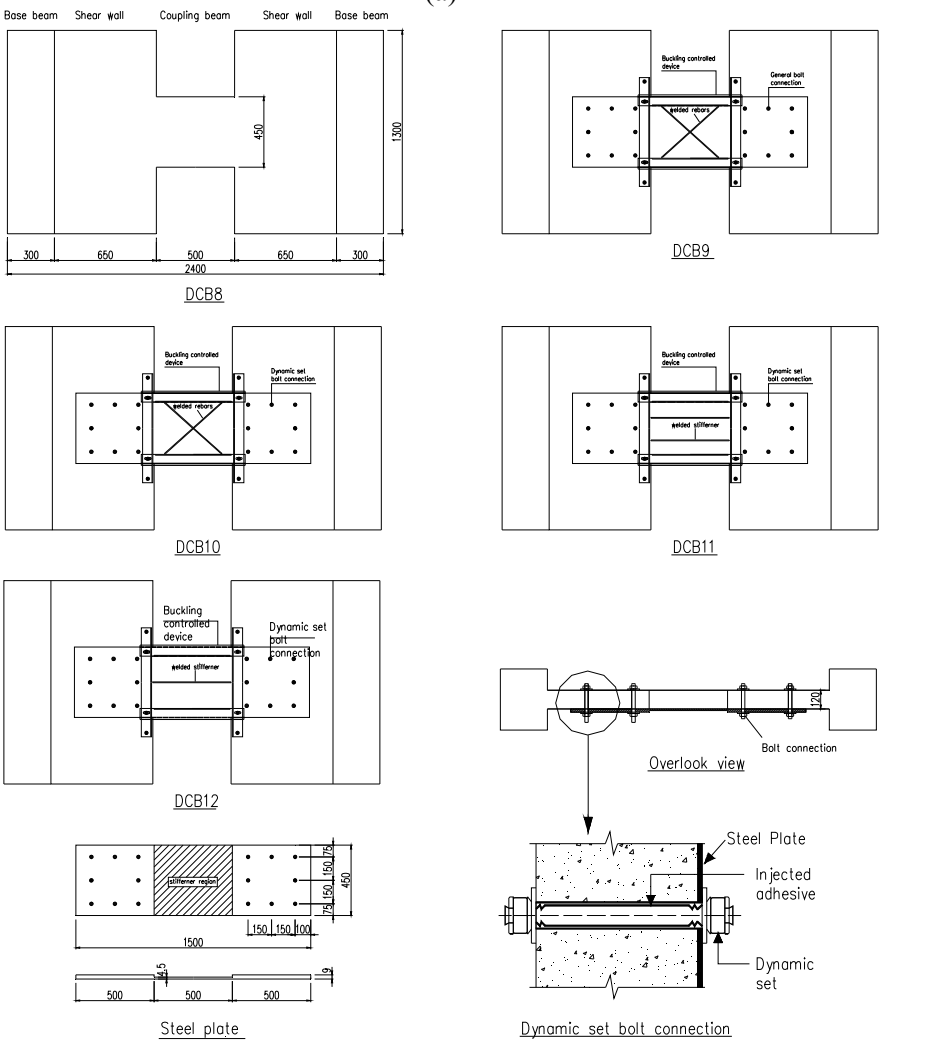

(b)

Figure 2. Details of test specimens: (a) RC details and (b) bolt-plate configurations

Table 1. Material Properties

	Concrete	Steel plate	
Specimen	f_{cu} (MPa)	f_{yp} (MPa)	E (MPa)
DCB8	59.6		
DCB9	61.4	362	203,420
DCB10	60.3	367	203,536
DCB11	60.1	345	200,386
DCB12	62.6	353	200,652

Reinforcement bars		
Type	f_y(MPa)	E (MPa)
T12	545	199,300
T16	556	187,865
T20	484	195,643
R8	473	189,500

The retrofitting schemes of all the specimens are shown in Table 2 and Figure 2b. The first specimen DCB8 with a plain RC arrangement was used for control purposes. The LRSP method and stiffeners were all applied to Specimens DCB9 to DCB12, as shown in Figure 2b. Stiffeners are structural elements connected to the steel sheet by continuous fillet welds. Rigid stiffeners are used to ensure that the plate can reach its full plastic strength and avoid overall buckling. Through numerical studies of the local buckling effects of steel plate, Cheng and Su [8] numerically found that, for steel plate with span-to-depth ratio 1.1, the height to thickness (h/t) ratio of steel plate should be lower than 62.5. Therefore, one horizontal or two horizontal and diagonal stiffeners are adopted. Rectangular steel plates with width of 20mm and thickness of 9mm are selected as horizontal stiffeners and steel rebars with diameter of 10mm are selected as diagonal stiffeners The stiffeners are placed symmetrically along the span of the steel plate, as shown in Figure 3.

Table 2. Coupling Beam Details

Specimen	Stiffeners	Plate thickness at span	Plate thickness at ends	LRSP method	Bolt property	Type of bolt connection
DCB8	N/A	N/A	N/A	N/A	N/A	N/A
DCB9	Two diagonal	4.5mm	9mm	Added	High-tensile steel	General
DCB10	Two diagonal	4.5mm	9mm	Added	High-tensile steel	Dynamic set
DCB11	Two horizontal	4.5mm	9mm	Added	High-tensile steel	Dynamic set
DCB12	One horizontal	4.5mm	9mm	Added	High-tensile steel	Dynamic set

The anchors at the ends of the steel plates were designed to be strong enough to transfer all loading from the steel plates to the wall regions using the linear bolt group theory. To avoid plate buckling in the anchor regions, thicker steel plates of 9 mm (which is twice the thickness of the plate in the span) were used in the anchor regions. To allow for construction tolerances, clearance through-holes were provided in the steel plates and concrete walls.

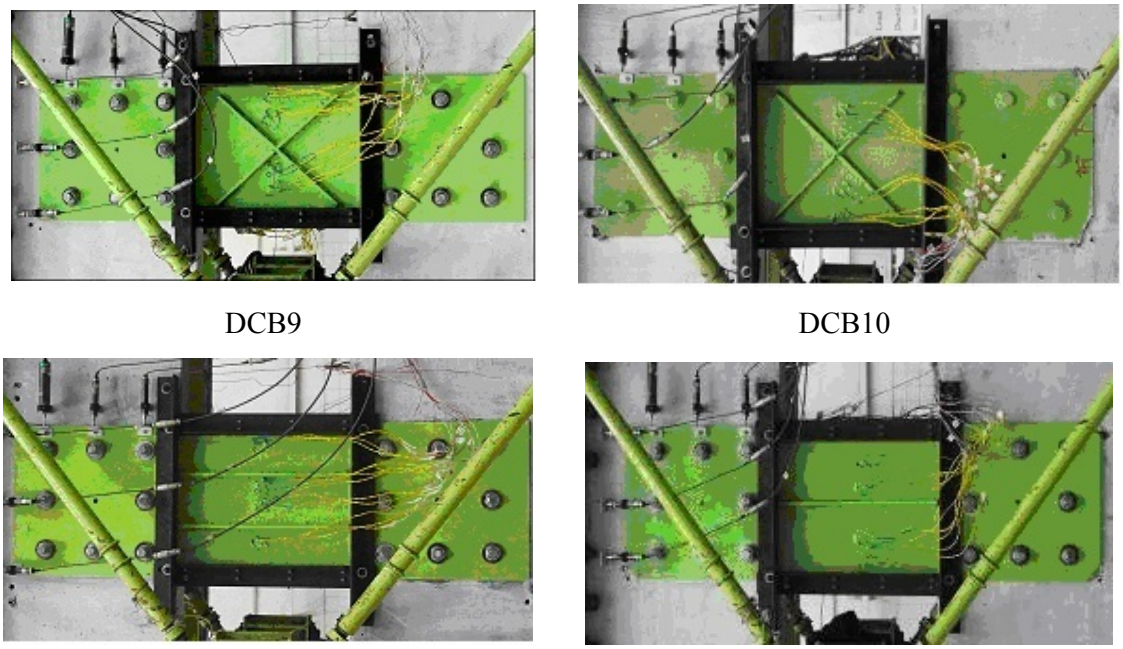

DCB9 DCB10

DCB11 DCB12

Figure 3. Stiffeners on Steel Plate

Since the steel plates were attached to coupling beams solely by bolt connections, the strength, stiffness and fixing details of the bolts would significantly influence the behavior of the entire retrofitting system. In this study, 20 mm diameter high strength bolts were used to fix the external steel plate, while slightly larger clearance through 22 mm diameter holes was provided in the steel plates and concrete walls to allow for fabrication tolerances. Two types of bolt connection are adopted in the specimens. One is the general bolt connection which screws the bolts by tightening torque to about 0.3 kNm (according to China Standard Q/STB 12.521.5-2000). The other is the dynamic set bolt connection which minimizes any possible slippage between various components at the connections by injecting adhesive to fill the gaps between the bolt shank and surrounding concrete (see Figure 2b).

3.2 Test Setup, Loading Procedure and Instrumentation

The load frame shown in Figure 4, designed by Kwan and Zhao [12], was used in the tests. To facilitate loading, the specimens were rotated 90º from their actual positions. The bottom end of each specimen was attached to a horizontal steel beam that was fixed to the floor, while the top end was attached to a structural steel beam that could move horizontally during the loading process. Reversed cyclic loading was applied by a 500 kN servo-controlled hydraulic actuator through a rigid arm at the top end of the specimen where the line of action of the applied shear force passed through the center of the beam. In this way, the coupling beam was loaded with a constant shear force along the span and a linearly varying bending moment with the point of inflection located at the mid-span, which simulated the real situation.

The specimens were tested under reversed cyclic loading to simulate an earthquake or wind forces. The loading process was divided into two phases: the first phase was load-controlled and the second phase was displacement-controlled. Reversed cyclical loading was applied to each specimen up to 75% of the estimated ultimate shear capacity (V_u^*). The subsequent cycles were displacement-controlled, in which the specimen was displaced to a nominal ductility factor (μ_n = 1)

for one cycle and then to each successive nominal ductility factor for two cycles, as illustrated in Figure 5. The beam rotations (θ), defined as the differential displacement between the two beam ends (Δ) in the loading direction divided by the clear span (l), were calculated using the displacements measured by the linear variable displacement transducers (LVDTs) L3 and L4, as illustrated in Figure 5. The nominal yield rotation (θ_{yn}) at μ_n = 1 originated from Park [13] and is obtained by extrapolating the average of the θ values corresponding to the positive and negative loads at $0.75V_u^*$ in the first cycle by a factor 4/3. The actual yield rotation (θ_y) was obtained in the same manner from the maximum measured shear (V_u). The test was terminated when the peak load reached in the first cycle of a nominal ductility level fell below the lesser of $0.8V_u^*$ and 0.8 V_u and the test specimen failed.

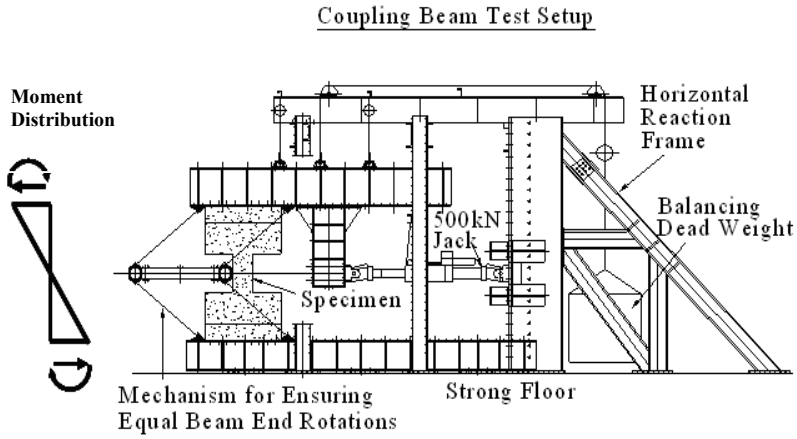

Figure 4. Test Setup

A number of instruments, including Linear Variable Displacement Transducers (LVDTs) and strain gauges, were installed to capture the deflection, curvature profiles and slippage of the bolt group in the anchor region. Strain gauges were attached along the plates, longitudinal bars and stirrups to investigate the deformations and internal load distributions of the steel plates and steel bars. The arrangements of the LVDTs and strain gauges are shown in Figures 6(a) and 6(b), respectively.

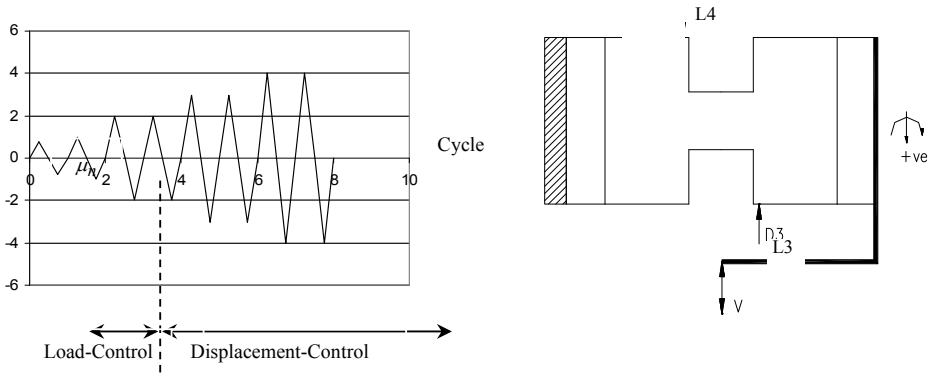

Figure 5. Loading History

4. RESULTS AND DISCUSSION

4.1 Strength, Deformation and Ductility

The performance of the specimens was evaluated through the measured strains and LVDT data. Several parameters were defined to interpret the results of the tests. The ultimate rotation θ_u is defined as the chord rotation angle at 0.8 V_u of an envelope curve on the softening branch and the yield chord rotation θ_y is defined as the chord rotation angle at 0.75 V_u of an envelope curve on the increasing branch. The maximum ductility μ is equal to the ultimate rotation θ_u divided by the yield chord rotation θ_y. As the test values for the positive cycles were not the same as those for the negative cycles, the values from the positive and negative cycles were averaged. It should be noted that Table 3 gives a summary of the experimental results before the rotation of 0.04 rad. This is because Qian and Xu [14] studied the deformation decomposition rule of RC shear wall structures and established the relationship between the deformation of coupling beams and inter-story drift. They pointed out that the rotation of coupling beam is about twice of the inter-story drift. Furthermore, Chinese Code (GB50011-2010) gives the inter-story drift ratio limit of 0.01 rad for high rise shear wall buildings under major earthquake conditions. Therefore if the rotation demand of coupling beams is more than 0.04 rad, the inter-story drift ratio demand of high rise shear wall buildings would probably exceed the codified drift limit.

Table 4 summarizes the experimental results of the ultimate strength V_u, the ultimate rotations θ_u and the ductility μ of all the tested beams. By comparing the test results of the retrofitted beams with those of the control specimen (DCB8), the increases in strength, rotation and ductility were calculated. By comparing the test results of DCB9 with general bolt connections and those of DCB10 with dynamic set bolt connections, the effects of bolt connections is revealed. It can be seen that the shear strengths V_u and ultimate rotation θ_u of DCB9 were all decreased when compared with those of the controlled specimen while the shear strengths V_u and ultimate rotation θ_u of DCB10 were increased by 67% and 116%, respectively. The results indicate that the type of bolt connection has significant effects on the behavior of retrofitted coupling beams. General bolt connections with clearance holes on steel plates result in large bolt slippage at the early loading stage. As a result, the concrete and steel plate did not work together effectively. Meanwhile, the dynamic bolt connections, with injected adhesive to fill the gap between the clearance hole and bolt shank, alleviated the slippage and ensured that the plate and concrete moved together effectively.

Table 3. Summary of Experimental Results

Specimen	Failure Mode	V^*_u kN	V_u kN	V_u increased %	v_{max} MPa	θ_y rad	θ_u rad	θ_u increased %	μ	μ increased %	K_o 10^6kN/m
DCB8	brittle	242	246	N/A	4.6	0.0055	0.0186	N/A	3.4	N/A	27
DCB9	brittle	460	244	**N/A**	**5.4**	**0.0039**	**0.0152**	**-18**	**3.9**	**15**	**38**
DCB10	ductile	460	411	**67**	**7.6**	**0.0092**	**0.0403**	**116**	**4.4**	**29**	**27**
DCB11	brittle	460	400	**63**	**7.4**	**0.0083**	**0.0287**	**54**	**3.5**	**3**	**29**
DCB12	ductile	460	366	**49**	**6.8**	**0.0076**	**0.0374**	**101**	**4.9**	**44**	**29**

By comparing the results of DCB11 with DCB12, the effects of the number of stiffeners can be studied. The only difference between these two specimens is the number of stiffeners used, DCB11

using two horizontal stiffeners and DCB12 using only one horizontal stiffener. The shear strengths V_u and ultimate rotation θ_u of DCB11 were increased by 63% and 54%, respectively, while the shear strengths V_u and ultimate rotations θ_u of DCB12 were increased by 49% and 101%, respectively. The results reveal that the number of stiffeners has significant effects on the behavior of retrofitted coupling beams. By adding fewer stiffeners, the increase in rotation deformability is much higher than the increase in shear strength. This is because using more stiffeners makes the plate more rigid and less ductile.

By comparing the results of DCB10 and DCB11, the effects of the stiffener arrangement can be investigated. The only difference between these two specimens is the arrangement of stiffeners, two diagonal stiffeners for DCB10 and two horizontal stiffeners for DCB11. The shear strength V_u and ultimate rotation θ_u of DCB10 were increased by 67% and 116%, respectively, while the shear strength V_u and ultimate rotation θ_u of DCB11 were increased by 63% and 54%, respectively. These results show that the stiffener arrangement can affect the deformability but not the shear capacity of the retrofitted beams. Diagonally arranged stiffeners can increase the deformability much more than horizontally arranged stiffeners for the retrofitted coupling beams.

The theoretical shear capacity (V_{code}^*) of DCB8, determined according to British Standards, is 242 kN which is very close to the average shear capacity (246 kN) obtained from the experiment. However, the theoretical shear capacities (V_{code}^*), using the full plastic assumption for steel plate of the retrofitted specimens, is 460 kN. Significant errors can occur in the prediction of shear capacity as a result of ignoring bolt slippage. For DCB9, with the general bolt connections, large bolt slippage can cause significant error (46%) in shear strength prediction. Meanwhile, for DCB10 and DCB12 with dynamic bolt connections, this error can be reduced to 10% to 25%.

The initial stiffness K_0 was obtained by dividing the load at 75% of the ultimate load by the corresponding displacement. As shown in Table 4, the initial stiffnesses K_0 of the retrofitted coupling beams are almost the same as those of the original specimen DCB8, but not those of specimen DCB9. The reason is that, for DCB9, with general bolt connections, at the early loading stage, concrete beam solely resists the shear loading, resulting in a lesser yield rotation than that of the other specimens. It can be concluded from the test results that this new seismic retrofitting method can increase the deformation and ductility of deep RC coupling beams while avoiding any substantial increase in their flexural stiffness. Since the total amount of base shear induced in a building during an earthquake is primarily dependent on the lateral stiffness of the structure, the proposed method would not impose extra forces on the building after seismic retrofitting.

4.2 Crack Patterns and Failure Behaviors

The concrete crack patterns of the test specimens were all very similar. The first cracks in the test specimens all occurred at the beam-wall joints and were inclined at about 45°. As the applied load increased, major diagonal cracks were formed across the beam span. These extensive diagonal cracks indicate that the shear capacity of the beams was insufficient. This result agrees with the anticipated brittle shear failure mode as a sufficient amount of longitudinal steel has been provided to avoid flexural failure prior to shear failure. The wall piers, including the joint regions, only experienced slight cracks when the beams failed.

Figure 7 shows the crack patterns of the control specimen DCB8 and the retrofitted specimens DCB9 and DCB10 at the same load level of 200 kN. It can be seen that serious diagonal cracks appeared in DCB8 and DCB9 at the early loading stage. Meanwhile, for DCB10, with dynamic bolt connections, at the same load level, much smaller diagonal cracks were observed. This means that the LRSP works well with the concrete beam from the early loading stage. This can help to delay

the increase in width of the diagonal cracks in concrete.

From the strain gauge data in the shear stirrups, the applied load corresponding to yielding of the stirrups can be identified. For the control specimen DCB8, the shear stirrups started to yield when the load increased to 264 kN. Soon after yielding, the shear force could no longer be resisted and the specimen reached its peak capacity (also at 264 kN). The results indicate that insufficient shear reinforcement is the primary cause of failure for the control specimen. When the shear links yielded, the strength could not be increased much further and shear link yielding caused the crack width to increase at a faster rate. The presence of high transverse tensile strains in the diagonal compressive struts eventually led to concrete cracking and crushing. For DCB9, the shear stirrups also yielded at a load of about 260 kN which is very similar to the case of DCB8. This means that, with the adoption of the general bolt connections, the additional steel plate did not mobilize initially and the shear transfer across the beam-wall joints through the steel plate was not activated. Hence, both DCB8 and DCB9 experienced a brittle failure mode. For DCB10 to DCB12, the shear stirrups also yielded at their ultimate load (at around 400 kN). The results show that, with the adoption of dynamic set bolt connections, the concrete beam can effectively work with the additional steel plate, and the steel plate contributes to the shear resistance in the early loading stage. Therefore, the shear links yielded at a higher load level and the crack width increased at a slower rate. This can also explain why Specimens DCB10 to DCB12 have better deformability.

4.3 Load-rotation Curves

Figure 8 shows the load-chord rotation hysteresis loops for all the specimens. The load-rotation curve of the control specimen DCB8 exhibited substantial pinching after reaching the peak load. This pinching is associated with a rapid stiffness degradation and reduced energy dissipation in the post-peak regime. For DCB9, due to the significant bolt slips, the steel plate did not deform in the early rotation level (< 0.04 rad). The load-rotation curve of DCB9 is very similar to that of DCB8, while in the later rotation level (> 0.04 rad), the load-rotation curve is similar to that seen with steel plate only. For DCB10 to DCB12, it can be seen that the pinching was less serious. Comparing the envelopes of the load-rotation curves, the retrofitted specimens (DCB10 to DCB12) with restrained plates exhibited more ductile behavior after the peak loads.

Compared with the previous beam test results [7] using LRSP without stiffeners, we have found that stiffeners can reduce the pinching effect, resulting in a more stable hysteresis behavior and higher energy dissipation. However, using stiffeners cannot completely mitigate the pinching effect.

4.4 Energy Dissipation and Stiffness Degradation

In order to compare the energy dissipation of the specimens, the energy dissipation coefficient (w) in each half-cycle was evaluated. The value of w is a ratio of the energy dissipation in each half-cycle to the elastic potential energy at the largest amplitude. Figure 9 shows the variations in w with a nominal ductility level in the first cycles. During the early ductility levels, the energy dissipation coefficients of all the specimens were small. At this stage, only hair cracks were observed and specimens remained elastic, which resulted in the small energy dissipation. For DCB8 and DCB9, the energy dissipation coefficients increased rapidly at the ductility level (μ_n=±1). This is because, at this stage, major diagonal cracks occurred in the specimens and large energy dissipation suddenly occurred. With the increase in ductility demands, the energy dissipation coefficients of DCB8 and DCB9 decreased rapidly. This is because brittle shear failure occurred. For DCB10 to DCB12, the energy dissipation coefficients increased after the ductility level (μ_n=±1); this means that the specimens entered into the inelastic deformation region later than the control specimen DCB8 and DCB9 with general bolt connections. With the increase in ductility

demand, the energy dissipation coefficients of the specimens remain stable and have an increasing trend. This is due to good composite action between the concrete beam and the steel plate, which has a stable shear deformation.

Figure 10 shows the variations r_k , which is a ratio of the secant stiffness (K) in the first cycle to that in the former first cycle at each nominal ductility level. Differences among the specimens were generally insignificant. It can be seen that, in the early ductility level (μ_n=±0.5), the secant stiffness of DCB8 was lower than that of the retrofitted coupling beams (DCB10 to DCB12). All specimens exhibited a severe loss of stiffness with the increase in deformation due to the occurrence of diagonal shear cracking in the concrete. It can be seen that, in DCB8 and DCB9, the stiffness decreased more rapidly than in the other specimens. For DCB10 to DCB12, although the additional steel plates have different stiffener arrangements, the variations of secant stiffness are very similar throughout the whole loading process.

DCB8 DCB9 DCB10

Figure 7. Concrete Crack Patterns

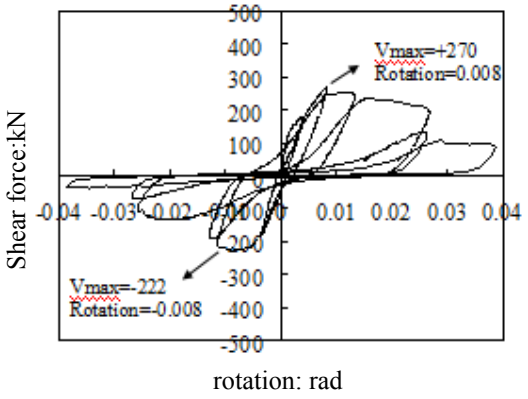

DCB8

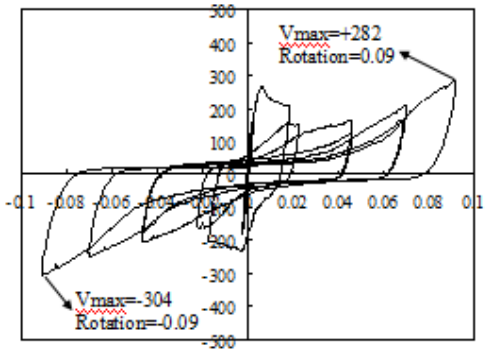

DCB9

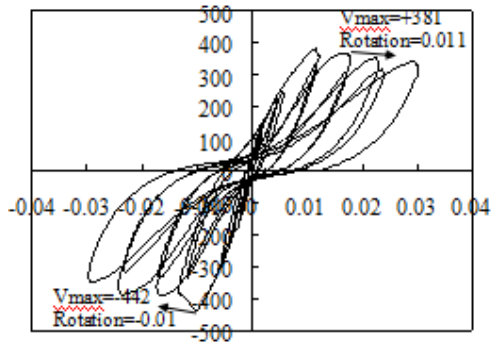

DCB10

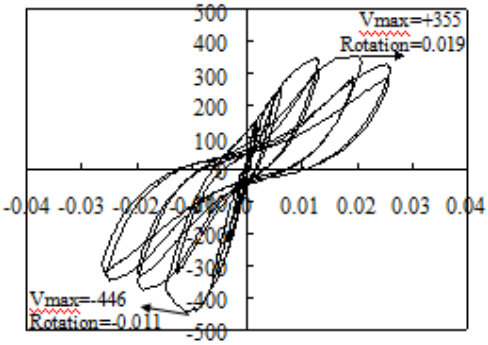

DCB11

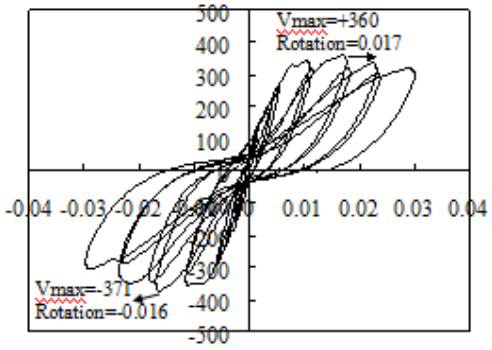

DCB12

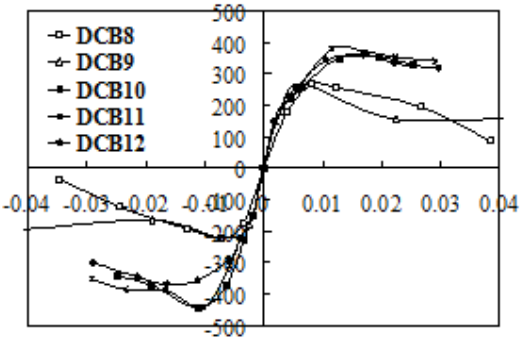

envelope

Figure 8. Load-rotation Curves

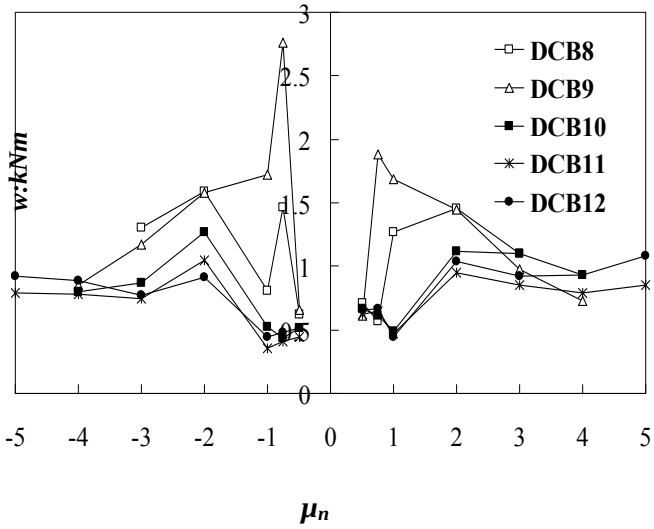

Figure 9. Variations of Energy Dissipated, with Ductility Level

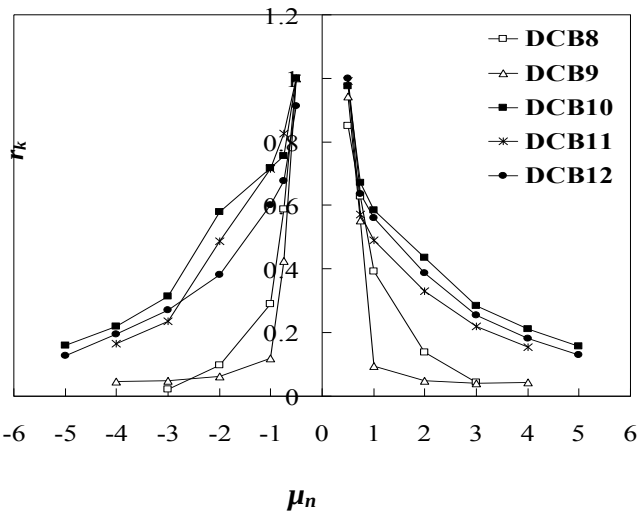

Figure 10. Variations of Stiffness Degradation, with Ductility Level

4.5 Behaviors of Steel Plates

The shear and axial strains of the steel plates can be obtained from the rosette strain gauges attached to the plate surfaces. Figure 11 shows the variations of the shear stress rosette 2 at the mid-span of the steel plate. These results reveal that the shear stress in the steel plate has an increasing trend as the chord rotation increases, which means that the steel plate can accommodate more shear forces. For DCB9 with diagonal stiffeners, it can be found from Figure 11 that when the rotation of coupling beam reached to 0.04rad, the shear stress is about 50Mpa. Therefore the steel plate remained in an elastic state. The reason is that, with the adoption of general bolt connections between the steel plate and concrete, the steel plate did not work together with the concrete beam successfully due to the large bolt slippage. Most shear force was resisted by the concrete beam during this loading stage. This resulted in more serious concrete crushing at the beam-wall joints and enhanced the rate of concrete deterioration. It also explains why DCB9 had poor deformability and brittle failure. For DCB10 with diagonal stiffeners and dynamic set connections, the steel plate remained in an elastic state. However, the deformability and ductility were much better than for DCB9. This is due to the fact that, with dynamic set connections, the steel plate and concrete beam worked together effectively. Diagonal stiffeners helped to delay the diagonal crack opening and resisted much of the compressive force at the beam-wall joints region, which resulted in the alleviation of concrete crushing at the beam-wall joints and the expectation that the concrete beam could resist more shear capacity. For DCB11 and DCB12 with horizontal stiffeners, steel yielding occurred suddenly at a rotation of about 0.01 rad. At the early loading stage, the concrete beam resisted most of the shear force. Major diagonal cracking occurred at about 0.01 rad and the shear capacity of the concrete beam reduced suddenly. After that, a significant portion of the shear force transferred from the concrete beam to the steel plate, which meant that it yielded and entered into a plastic state. With the rotation increased, for DCB11 with two horizontal stiffeners, due to the larger stiffness of steel plate, more shear force could be resisted. On the other hand, due to elongation of the steel plate with large axial stiffness, more compressive force was applied to the concrete beam which resulted in earlier concrete crushing. This can explain why DCB11 has higher strength but poorer deformability and ductility. Although DCB12 with one horizontal stiffener has lower strength than DCB11, due to the lesser axial stiffness of steel plate, it demonstrates better deformability and ductility.

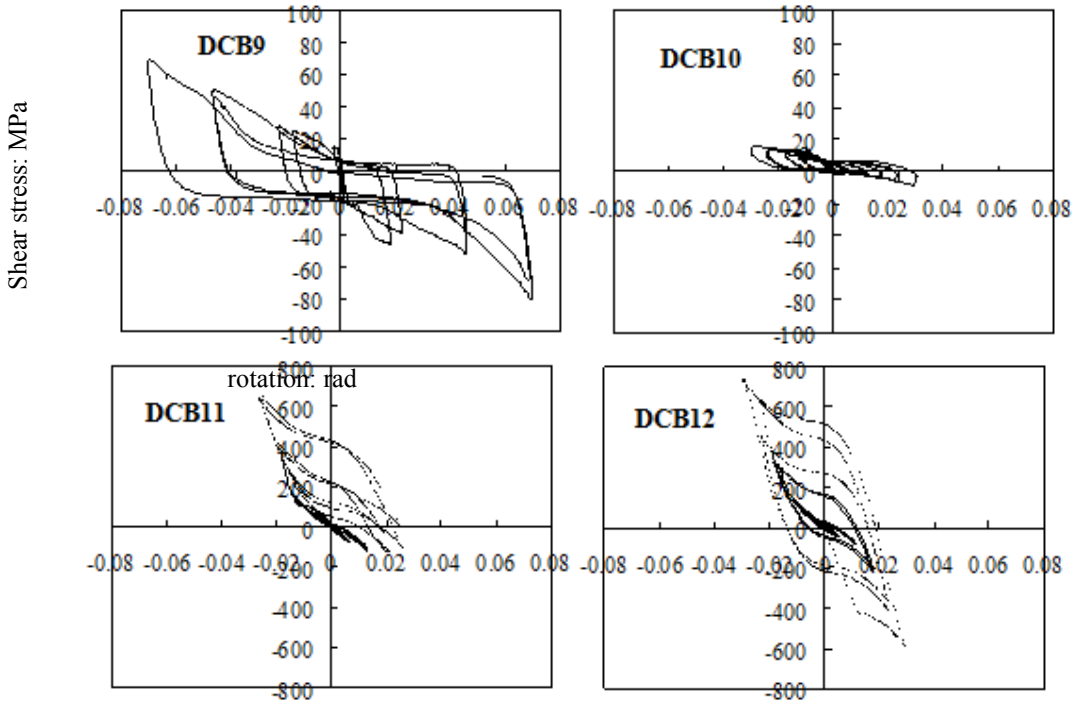

Figure 11. Shear Stress at the Point (Rosette 2) of the Steel Plates

4.6 Slips of Bolt Groups

The composite action of coupling beams and a bolted steel plate was accomplished by anchor bolts which must slip under the interfaces of the shear forces. Using the LVDT arrangement (L6-L8), as shown in Figure 6, the average rotational movements at the center of the anchor bolt groups were found.

The rotations determined from the LVDT readings in the longitudinal directions were defined as the 'longitudinal rotation'. The value of longitudinal rotation is divided the deference between L6 and L8 by the distance between them. As shown in Figure 12, the longitudinal rotation of DCB9, which had general bolt connections, is much higher than that of other specimens due to the significant slippage between the concrete and bolt connection. While for DCB10 to DCB12, which had dynamic set bolt connections, the rotation of the bolt group increased almost linearly with the increase in chord rotation, the maximum longitudinal rotation was lower than 0.01 rad. This demonstrates that the bolt groups were strong enough and able to behave elastically, while the concrete beams underwent inelastic deformation.

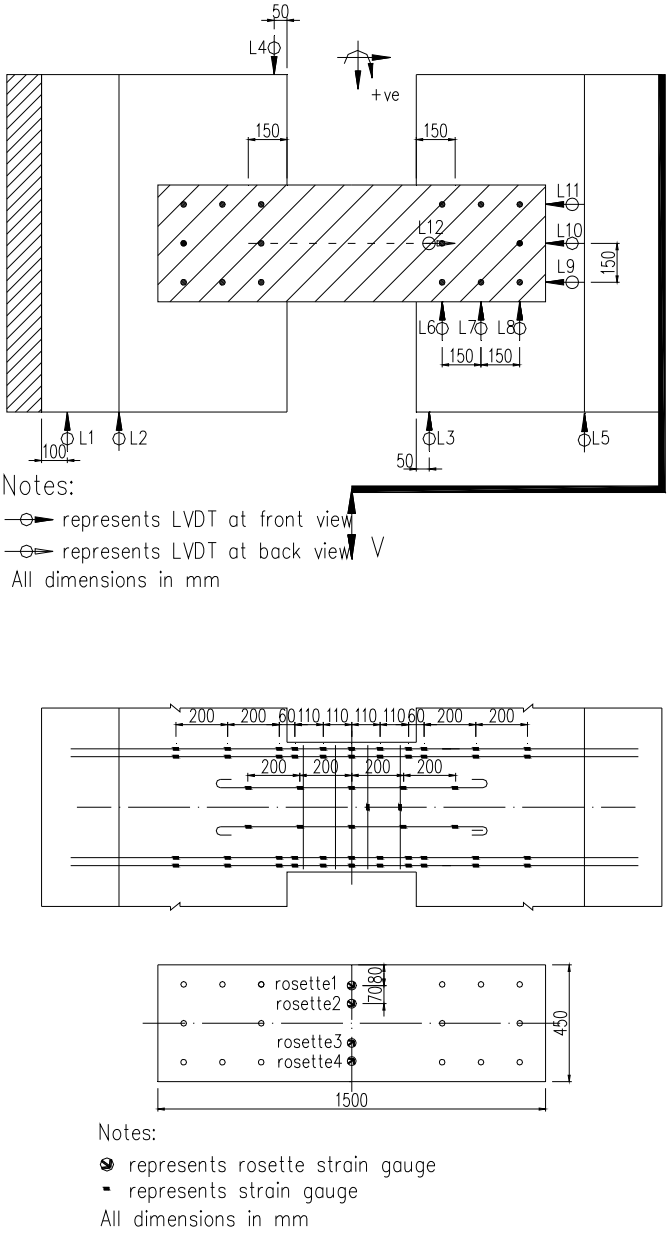

Figure 6. Instrumentation: (a) LVDT Arrangement; (b) Strain Gauge Arrangement

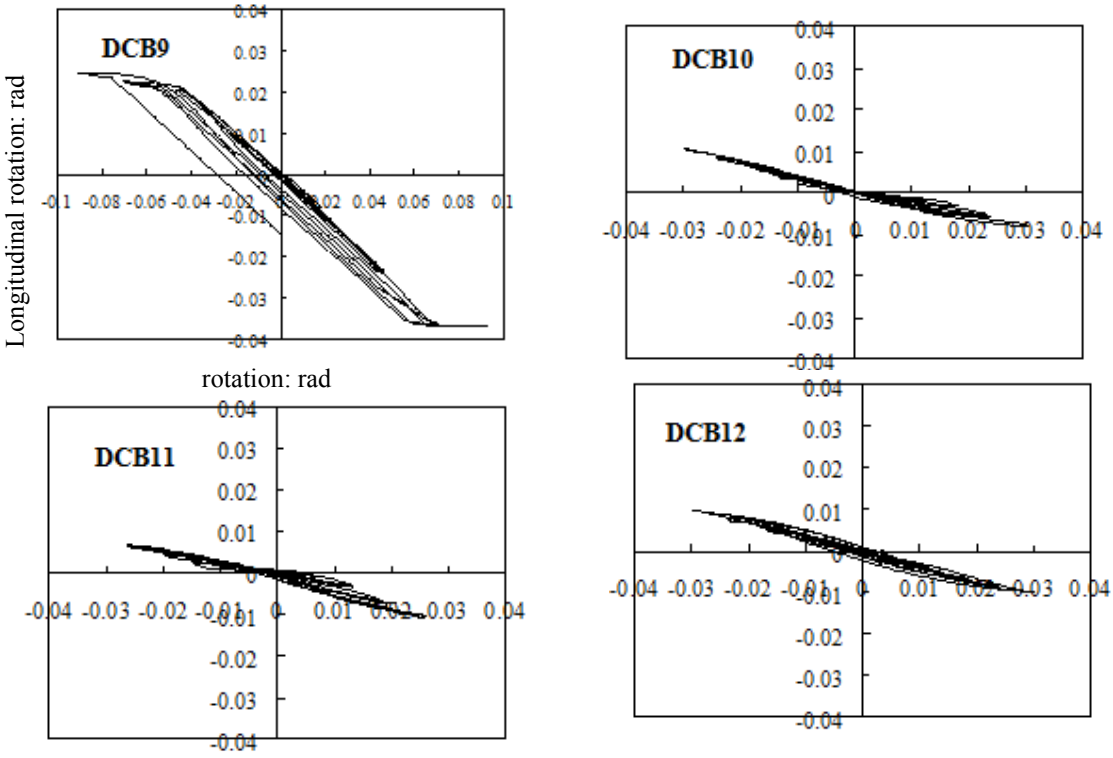

Figure 12. Longitudinal Rotation of Bolt Group

5. CONCLUSIONS

Experimental study was conducted on laterally restrained steel plate with stiffeners for the seismic retrofitting of concrete coupling beams. The main findings of this study are summarized as follows:

1. The use of laterally restrained steel plate with stiffeners for the seismic retrofitting of concrete deep coupling beams has demonstrated effectiveness in increasing deformability and energy dissipation while reducing strength and stiffness degradation. Also, the retrofitted beams failed in a less brittle manner.
2. The type of bolt connections used is found to have significant effects on the performances of the retrofitted coupling beams. Dynamic set bolt connections with adhesive to fill in the gap between the concrete and bolt can alleviate bolt slippage and make the retrofitted coupling beams achieve a desirable seismic response. By comparison with the general bolt connections, the shear capacity of the LRSP coupling beam can be increased by 67% and the ultimate deformation can be increased by 116% by using dynamic set bolt connections.
3. The stiffener arrangements also have significant effects on the performances of the retrofitted coupling beams. Providing stiffeners can prevent pinching of the hysteresis curves, increase the shear strength and enhance the energy dissipation capacity. On the other hand, too much stiffening would lead to a loss of structural deformability. It is concluded that an optimum amount of diagonal stiffeners should be used to simultaneously achieve desirable strength and deformability. The steel rebars with diameter of twice of the thickness of steel plate are suggested as the diagonal stiffers.
4. The prediction of the shear capacity of retrofitted coupling beams based on the full plastic section assumption without considering the effects of plate buckling and bolt slips would overestimate the true capacity by 10 to 25%.

ACKNOWLEDGEMENTS

The work described in this paper has been fully supported by the National Natural Science Foundation (Project No.51208023), Beijing Natural Science Foundation (Project No.8162014) and National Natural Science Foundation (Project No.51408436).

REFERENCES

[1] Paulay, T., "Coupling Beams of Reinforced Concrete Shear Walls", Journal of the Structural Division, 1971, Vol. 97 (ST3), pp. 843-862.

[2] Mitchell, D., Devall, R.H., Saatcioglu, M., Simpson, R., Tinawi, R. and Tremblay, R., "Damage to Concrete Structures due to the 1994 Northridge Earthquake", Canadian Journal of Civil Engineering, 1995, Vol. 22(2), pp. 361-377.

[3] Wang, Y.Y., "Lessons Learned from the "5.12" Wenchuan Earthquake: Evaluation of Earthquake Performance Objectives and the Importance of Seismic Conceptual Design Principles", Earthquake Engineering and Engineering Vibration, 2008, Vol. 3, pp. 255-262.

[4] Harries, K.A., Cook, W.D. and Mitchell, D., "Seismic Retrofit of Reinforced Concrete Coupling Beams using Steel Plates", ACI SP-160, 1996, Vol. 6, No. 1, pp. 93-114.

[5] Su, R.K.L. and Zhu, Y., "Experimental and Numerical Studies of External Steel Plates Strengthened Reinforcement Concrete Coupling Beams", Engineering Structures, 2005, Vol. 27, No. 10, pp. 1537-1550.

[6] Su, R.K.L. and Cheng, B., "Plate Strengthened Deep Reinforced Concrete Coupling Beams", ICE-Structures and Buildings, 2011, Vol. 164, No. 1, pp. 27-42.

[7] Cheng, B. and Su, R.K.L., "Retrofit of Deep Concrete Coupling Beams by Laterally Restrained Side Plates", Journal of Structural Engineering, 2011, Vol. 137, No. 4, pp.503-512.

[8] Cheng, B. and Su, R.K.L., "Numerical Studies of Deep Concrete Coupling Beams Retrofitted with a Laterally Restrained Steel Plate", Journal of Advances in Structural Engineering, 2011, Vol. 14, No. 5, pp. 903-915.

[9] Lu, Y. and Li, G.Q., "Slim Buckling-restrained Steel Plate Shear Wall and Simplified Model", Advanced Steel Construction, 2012, Vol. 8, No. 3, pp. 282-294.

[10] BSI, CP114, "British Standard Code of Practice, Part 2: The Structural Use of Reinforced Concrete in Buildings", London: The Council for Codes of Practice, British Standards Institution, 1969.

[11] BSI, BS5950, "Structural Use of Steelwork in Building, Part 3: Design in Composite Construction, Section 3.1: Code of Practice for Design of Simple and Continuous Composite Beams", London: British Standards Institution, 1990.

[12] Kwan, A.K.H. and Zhao, Z.Z., "Testing of Coupling Beams with Equal End Rotation Maintained and Local Joint Deformation Allowed", Proceedings of the Institution of Civil Engineers – structures and buildings, 2002, Vol. 152, No. 1, pp. 67-78.

[13] Park, R. "Ductility Evaluation from Laboratory and Analytical Testing", Proceedings of the Ninth World Conference on Earthquake Engineering, Tokyo-Kyoto, Japan, 1988, pp.605-616.

[14] Qian, J.R. and Xu, F.J., "Deformation Decomposition Rule of RC Frame Core Tube Structures", Building Structure, 2006, Vol.36, No. 12, pp. 33-36. (in Chinese)

ICSAS 2016

The organizing committee is pleased to announce The Eighth International Conference on Steel and Aluminium Structures (ICSAS) 2016 to be held in Hong Kong, a dynamic metropolitan with thriving construction industry.

Introduction

Seven ICSAS Conferences have been successfully held in Cardiff, UK (1987), Singapore (1991), Istanbul, Turkey (1995), Helsinki, Finland (1999), Sydney, Australia (2003), Oxford, UK (2007) and Kuching, Malaysia (2011). The conference aims at bringing international experts and leaders together to disseminate recent research findings in the fields of steel and aluminium structures. It will also provide a forum for the discussion of the developments in the design and construction of steel and aluminium structures.

Who Should Attend

Steel and aluminium structure designers and manufacturers, trade associations, design engineers, steel fabricators, architects, owners or developers of steel and aluminium structures, researchers, academics and post-graduate students.

Key Dates

Abstract Submission	November 30, 2015
Acceptance of Abstract	January 15, 2016
Full Paper Submission	April 15, 2016
Acceptance of Full Paper	August 15, 2016
Conference	December 7 – 9, 2016

8TH INTERNATIONAL CONFERENCE ON STEEL AND ALUMINIUM STRUCTURES

DECEMBER 7 – 9, 2016 HONG KONG

Call for Papers

Prospective authors are invited to submit abstracts before **November 30, 2015**, on the topics as follows (but not limited to):

- Analysis and Design of:
  - Structural Steel
  - Stainless Steel
  - Aluminium Alloy
- Architectural Uses
- Cold-formed Steel Structures
- Composite Structures
- Computational Modelling and Analysis
- Connection Behaviour
- Earthquake and Seismic Analysis
- Fire Engineering
- Material Properties and Structural Reliability
- Plates and Shell Structures
- Scaffoldings and Racks
- Specification and Standard Developments
- Sustainable Development
- Tubular Structures

Abstracts should be submitted electronically via the conference website: www.civil.hku.hk/ ICSAS2016

Exhibition

Booths will be organised for exhibitors during the Conference, allowing companies and associations an excellent opportunity for marketing and promotion.

For exhibition information contact:
Prof. Ben Young
Department of Civil Engineering
The University of Hong Kong
Email: young@hku.hk

Prizes

Three papers will be selected for the following awards:

- *Best Steel Structures Paper Award*
- *Best Aluminium Structures Paper Award*
- *Best Composite Structures Paper Award*

Organised by

Department of Civil Engineering
The University of Hong Kong

The University of Hong Kong

www.civil.hku.hk/ICSAS2016

ORDER FORM

ISSN 1816-112X

Advanced Steel Construction, an international journal

Indexed by the Science Citation Index Expanded, Materials Science Citation Index and ISI Alerting Services

From: _____

To: ***Secretariat, Advanced Steel Construction, an international journal***
Fax: (852) 2334-6389

I/ We would like to enter a subscription to the ***International Journal of Advanced Steel Construction (IJASC)*** *published by The Hong Kong Institute of Steel Construction.*

Please complete the form and send to:

International Journal of Advanced Steel Construction
c/o Department of Civil and Environmental Engineering
The Hong Kong Polytechnic University
Hunghom, Kowloon, Hong Kong

Fax: (852) 2334-6389 Email: ceslchan@polyu.edu.hk

Published by : The Hong Kong Institute of Steel Construction
Website: http://www.hkisc.org/

Please tick the appropriate box

- ❑ Please enter my hard-copy subscription **(4 issues per year)**.
- ❑ Please send me a complimentary copy of the *Advanced Steel Construction, an International Journal (IJASC).*

Please tick the appropriate box(es)

	Print	**On-line is free**
Personal	❑ US$ 125	
Institutional	❑ US$ 280	

Total Amount **US$** _____

Methods of payment *(please tick the appropriate box(es))*

- ❑ Please invoice me
- ❑ Cheque enclosed for US$ _____ payable to Hong Kong Institute of Steel Construction Limited (No personal cheque accepted)

Ship to

Name (Prof./ Dr./ Mr./ Ms.) _____
Address _____
_____
_____
City/ State/ Postal Code _____
Country _____
Email _____ Fax _____